UNIVERSITY OF LIVERPOOL

A Non-Invasive Beam Current Monitor for a Medical Accelerator

Thesis submitted in accordance with the requirements of the

University of Liverpool

for the degree of Doctor in Philosophy by

Tomasz Cybulski

October 2017

ABSTRACT

Proton or heavy ion beams are a very attractive and promising tool in cancer therapy. They offer much localised and better controlled dose distributions in comparison to X-rays, thus, decreasing damage sustained by healthy tissue. Diagnostics of these beams is particularly interesting as interference with the beam, especially in the case of the ocular treatment, leads to a significant degradation of essential parameters of beam, therefore, non-interceptive methods of monitoring are preferred.

In this work, a novel method of a proton beam current monitor was devised, relaying on non-invasive measurements, investigating the proton beam halo region. The method required adaptation of the LHCb VELO detector to allow its operation as a stand-alone device. The performance of the detector was tested in conjunction with a dedicated Faraday Cup, optimised to suit the clinical proton beam characteristics at the Clatterbridge Cancer Centre (CCC). To perform theoretical predictions of the proposed monitor, auxiliary measurements were completed that involved other instrumentation such as scintillating screens. They were used in the beam profile measurements that sourced information used afterwards to create a model of the existing beamline, which was used to find the extent of and nature of the beam halo extent.

The thesis presents results of theoretical studies and modelling of different parts of the experimental set-up leading to the final design of the mentioned monitor, followed by a first successful run with a proton beam at CCC. A discussion on the outcomes of data analysis is presented with indication for possible future development of the method.

Although the monitor was prepared and tested with a 60 MeV proton beam, the instrumentation can used with higher energy hadron therapy beams, including other particle species than protons once additional adaptation to their properties has been performed.

TABLE OF CONTENTS

1. INTRODUCTION

1.1 Foreword

Modern medicine takes advantage of many different treatment techniques in the battle against malicious cancer cells. Aside from conventional methods, e.g. tumour resection and chemotherapy, radiotherapy techniques offer a very precise treatment tool either on their own or complementary to conventional methods. The discovery of X-rays by Wilhelm Conrad Roentgen in 1894 [1] started an era where ionising radiation has found its applications in both industry and medicine. Linear accelerators (LINACS) became wide-spread sources of both electron and X-ray beams of energies higher than 1 MeV.

Electron and X-rays beams in the energy range between 5 MeV and 16 MeV are commonly used in cancer treatment. [2] The development of linear accelerators technology made them user friendly and compact facilities. The standardisation of technology has also brought down their price by reducing manufacturing costs and turned them into affordable devices for radiotherapy centres all over the world. Alongside the standardisation of technology, medical procedures followed the same path of setting various model treatments. Other disciplines, like dosimetry and radiobiology, were concurrently developed to investigate the pros and cons of radiotherapy methods. The interaction mechanisms of electrons and photons with matter were also thoroughly studied to support the aims of radiation therapy. Ionisation of cell structures invoked by radiation, regardless of whether they belong to cancer-affected or healthy tissue, supports control of the lifecycle of cells by directing them towards death induced by the extent of suffered damage. Any adverse effects of radiation therapy must be avoided in healthy tissues surrounding tumours by precise control of the beam parameters during radiation delivery, which among many, involve energy, geometry and amount of deposited dose. Continuous technological advances in accelerator science has led to much more localised radiation delivery methods, offered nowadays, reducing the extent of radiation treatment complications.

In recent decades protons and heavy ions have been widely used in cancer treatment as they demonstrate very advantageous dose distribution profiles in comparison to conventional photon therapy. The dose depth curves determined by the energy transfer rates demonstrate inversion of the dose depth profiles for charged particles with a prominent peak at the end of

their range and preserving low energy transfer at the beginning of the path in matter. This type of behaviour comes from their kinetic energy being dissipated in many Coulomb interactions with atomic electrons with an increased number of interactions rate towards the end of their finite path.

The cost of facilities delivering hadron therapy beams is significantly higher than for the conventional solutions, which restricts their availability. Nevertheless, hadron beam delivery techniques offer many clinical benefits and satisfy demand for more conformal dose distributions that gives justification to their, yet scarce, creation. At the same time, a demand in advances and development of more sophisticated methods in quality assurance measurements is generated. As a result a new technique of monitoring proton beams used in ocular treatment was proposed and is presented in greater detail in this thesis. The concept was brought forward after a preliminary experiment performed by the High Energy Physics Group (HEP) at the University of Liverpool described in the next section.

1.2 Motivation

Monitoring of the dose delivery during treatment plays a vital role in radiotherapy. The control systems terminate the radiation once the prescribed dose has been achieved. This is based on information collected from monitors implemented on machines as safety interlocks to detect any inadmissible abnormalities in dose rate, symmetry of the beam profile, energy and many other parameters. The wide-spread standard used in radiation monitoring are ionisation chambers. Throughout the years they proved to be the most reliable and versatile monitors, easy to maintain and also cost-effective. Their principle of measurement relies, however, on an invasive method, where the beam must pass through the active volume of the detector to induce ionisation of gas contained between its electrodes. Photon radiation in conventional radiotherapy does not suffer significant energy degradation when passing through the chamber due to the interaction mechanisms with matter. [3] In this fashion the clinical properties of the beam remain practically unchanged. The same measurement principle applied to charged particle beams affects their properties to a much larger extent. In general high-Z materials have more scattering effects on proton beams and a smaller effect on the energy degradation. The opposite is observed for low-Z materials, e.g. aluminium, which the ionisation chambers are made of. For them, the energy degradation is larger than the lateral scatter. [4]

The 60 MeV proton beam at the Clatterbridge Cancer Centre (CCC) has a measured range in water of $\mathrm{d} = 29.9\ \mathrm{mm}$, which is the lowest maximum clinical range of protons when compared to other similar treatment centres. Range of protons is defined as a mean depth of penetration measured along a straight line parallel to incidence of protons from a point where protons enter an absorbing medium to the point at which additional displacement is no longer detectable. [11] Even though, the beam has sufficient range to be used in treatments of a majority of ocular posterior tumours, which on average are situated at the depth of $27.0\ \mathrm{mm}$. The deepest tumour locations are reported to be about $31.0\ \mathrm{mm}$. [5] The design of the beam line at CCC, where beam travel happens in air and passes through a couple of quality assurance devices (two parallel-plate ionisation chambers), results in degradation of the maximum nominal energy $\mathrm{E_{nominal}} = 62.0\ \mathrm{MeV}$ by $\Delta\mathrm{E} = 2.0\ \mathrm{MeV}$. As a consequence, the nominal penetration depth of protons of $\mathrm{d_{nominal}} = 31.0\ \mathrm{mm}$ for the stated nominal energy is reduced to the reported 29.9 m, and the availability of treatments for deeper located tumours is restricted. Therefore, the concept of a non-invasive beam current monitor prototype was brought forward to investigate the feasibility and accuracy of measurements as an alternative to the energy-degrading ionisation chambers. The development of a model of a non-invasive monitor was preceded by tests of a multi-strip silicon particle tracking LHCb VELO (VELO) detector operating at CERN, carried out by the High-Energy Physics Group at the University of Liverpool. The detector was installed at CCC to examine whether the high sensitivity of the detector response to minimum ionising particles (MIPs) [3] can be effectively applied to monitor a low energy proton therapy beam.

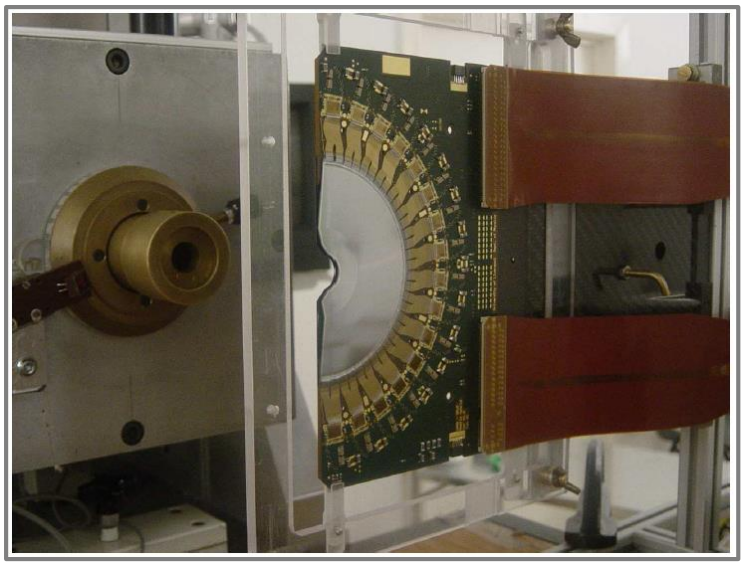

Figure 1: Set-up of the initial measurements with the LHCb VELO detector with a proton therapy beam at CCC performed by the High-Energy Physics Group at University of Liverpool. (Courtesy of Gianluigi Casse) [8]

During tests, the VELO detector was positioned at several locations starting from the treatment nozzle and progressing in the beam propagation direction z. A brass terminating aperture was fitted on the nozzle to decrease the beam diameter to $\Phi = 15\ \mathrm{mm}$ (figure 1). Hit maps were obtained across the surface of the detector as a function of the radial distance from the beam axis at five z positions: $25\ \mathrm{mm}$, $70\ \mathrm{mm}$, $110\ \mathrm{mm}$, $153\ \mathrm{mm}$ and $230\ \mathrm{mm}$. The measured extent of the beam halo in the vicinity of the treatment iso-centre can be examined in figure 2.

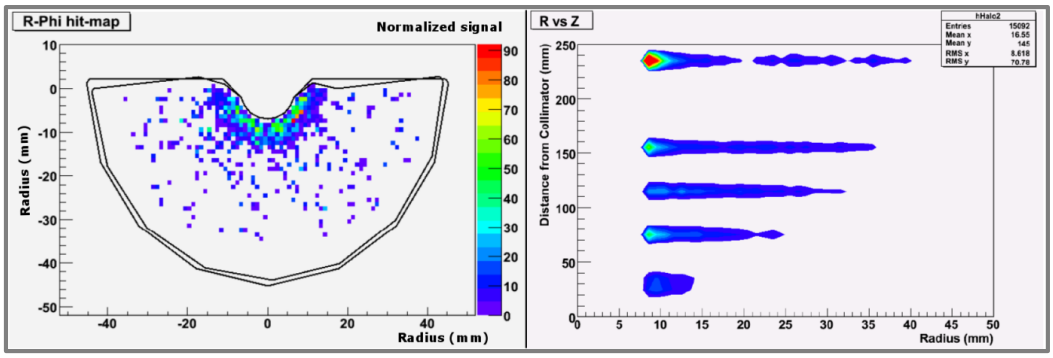

Figure 2: A measured proton beam halo hit map reconstructed by the LHCb VELO detector for the position $z = 25\ mm$ (on the left) and the extent of the proton beam halo as a function of the distance from the treatment nozzle (on the right). (Courtesy of Gianluigi Casse).[8]

The results have proven that the design of the VELO detector, possibly along with other similar detectors, can be potentially applied as a part of a beam monitoring instrumentation having an advantage of introducing no interactions, which could affect the core of the beam, owing to the design of the sensors.

In consequence, the outcome of the presented research became a motivation to investigate the properties of the VELO detector as a source of information about the absolute beam current intensity relying on the beam halo measurements.

1.3 Objectives of the proposed concept

Accelerator science utilises many different types of detectors to monitor the parameters of both relativistic and non-relativistic beams. Beam current monitoring is crucial to reflect on the overall performance of the machine, validation of the design and application of any essential adjustments to the parameters determining the optimal performance of an accelerator. This is especially critical for medical applications of accelerators, where parameters of the beam determine the clinical efficiency of cancer treatment. In the case of proton therapy of ocular lesions at CCC, the energy of the proton beam falls into the lower region of relativistic velocities (γ =1.064 and $\beta = 0.34\ c$) and can easily be degraded. Therefore, the quality assurance and beam monitoring during treatment must be kept at the lowest possible levels of interception and therefore the absolute beam values are determined only prior to the treatment using a destructive Faraday Cup.

The concept of the non-invasive beam current monitor incorporating the stand – alone operation of the VELO detector appeared to give rise to a new measurement method that could

reduce degradation of the beam energy and potentially extend the application of the detector to medicine.

In normal operation, the VELO detector collects information about the tracks of vertices originating from the collision region at the LHCb experiment at CERN at a frequency $f_{LHC} = 40MHz$ [9], synchronised with the bunch crossing frequency in the LHC accelerator. In principle, the detector parameters could be adjusted to perform measurements at the time of bunch crossing at CCC, however, this requires significant contribution to re-design the optical triggering system. A more detailed explanation of the technical aspects of the VELO detector are covered in chapter 4. As a result, the design of the monitor prototype was directed to assess the feasibility and sensitivity of the method that in principle investigated correlation between the average values of the absolute beam current and the magnitude of amplitudes obtained from the VELO detector.

The determination of the proton beam halo distribution calls for position of the VELO detector to be known in the three cardinal directions: horizontal, vertical and longitudinal. Additionally, the achieved alignment of the detectors on either side of the beam had to be concentric. This required the development of an advanced detector positioning system that provided sufficient support and protected the detector from any damages. The available space for integration with the existing beam line involved adjustments necessary to adapt the detector to operate outside the environment which it was designed for. At CCC, VELO was run without vacuum whilst the sensors were still kept at a low temperature to minimize their radiation-induced deterioration. The above prerequisites were carefully tackled in the framework of this thesis.

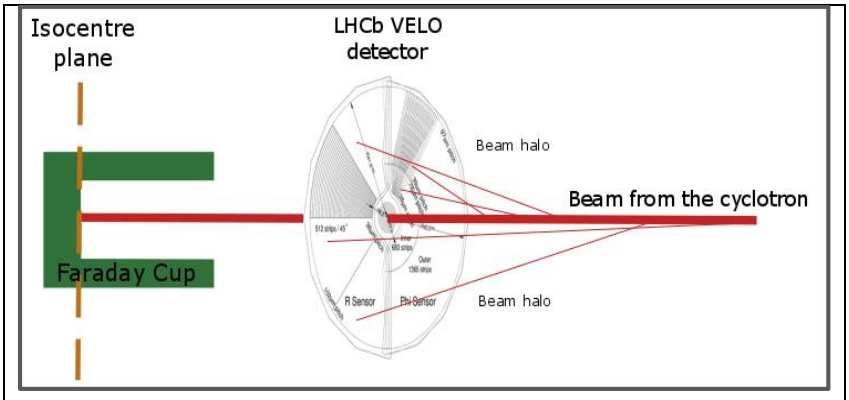

Figure 3: A concept of test measurements for the proposed non-invasive method for beam current measurement.

Literature studies were carried out to investigate measurement capabilities of different beam intensity detectors used for accelerators. The ideal detector for the beam current measurement at CCC ought to resolve shape of single bunches from the cyclotron and be suitable for the energy and intensity characteristics of the beam. An impedance-matched Faraday Cup (FC) proved to meet the set conditions and offered a spectrum of advantages such as simplicity of design, good mechanical properties, performance robustness and a wide bandwidth for electric signal transfers, which are addressed and explained in chapter 3. In general, a FC comprises of a bulk of a conducting material, which terminates protons and builds up charge that can be read out by an external electronic circuit. The shape of the beam collector of the FC was optimised in this project to minimize errors in the charge collection originating from losses due to particle emission from the surface of the conductor when measuring the beam.

The development process of the experimental set-up for a non-invasive beam current monitor and results produced during tests with the proton beam at CCC are the aim and subject to discussion in the following chapters of this dissertation.

2. RADIATION THERAPY

The World Health Organisation and World Cancer Research Fund International have reported that the number of deaths from non-communicable diseases, e.g. cancer, cardiovascular diseases or diabetes, constitute about 80% of death causes in the world. [6] In 2012 14.1 million cancer cases were registered, with men suffering from cancer more often (7.4 million cases) than women (6.7 million cases). It is expected that these numbers will increase to 24 million a year in 2035. [6] Diet, maintaining a healthy weight and regular physical activity are linked with prevention of expected rates of common cancers in the wake of the predicted raise. The three most common types, which were assessed statistically, are lung, breast and colorectal cancer. They constitute respectively 13%, 11% and 9.7% of all cases reported in 2012. Cancer treatment employs many different methods of therapy, including surgery, chemotherapy and radiotherapy. Tumour resection may, however, not always be possible due to the location of the lesions, especially when the shape is hard to define or it is adjacent to critical organs determining the quality of the patient's life. In such cases, chemotherapy or radiotherapy may be a better choice. The principles of either classical X-ray radiotherapy or advances of hadron therapy, exploiting protons or heavy ions, aim to deliver the required dose to the tumour volume with the prescribed accuracy of the dose distribution. At the same time, care is taken to minimize any dose delivered to the healthy tissue, which could adversely disable the functions of organs at risk and have fatal consequences. Therefore, radiation delivery techniques demand constant improvement and refinement in the dose volume conformance. A precise radiotherapy treatment means that a number of the physical parameters of radiation beams must comply with certain quality levels defined for the intended clinical application. These include, among many others, the lateral beam profile extent, desired energy or energy spread to guarantee the treatment effectiveness. Proton treatment, especially of ocular tumours, is particularly susceptible to small changes in the quality of the beam due to the mechanisms of proton interactions with matter and low kinetic energy.

This chapter will outline basics of physics in the radiotherapy techniques and introduce how they link with the clinical applications. A short overview of the accelerator types in hadron therapy will be presented and the characteristics of the treatment proton beam at CCC will be given.

2.1 Interactions of ionising radiation in matter

Radiotherapy takes advantage of many physical phenomena leading to ionisation of atoms. There are two types of radiation used in modern radiotherapy:

- Indirectly ionising radiation of X-ray photons in conventional radiotherapy, which historically was the first to be used in radiation therapy;
- Directly ionising radiation composed of heavy charged particles such as protons and heavy ions.

Their interaction mechanisms are distinctively different and whilst the passage of photons though matter may occur without any interaction, the probability of no-interactions for charged particles is zero because of their Coulomb field.

2.1.1 Interaction of photons with matter

The interactions of photons with atoms are energy dependent and for the therapeutic range of energies (typically between 4 and 25 MeV) they are mainly based on interactions with electrons orbiting the atomic nuclei. There are three major processes involved in their energy deposition in a medium:

- Photoelectric effect, when an incident photon interacts with an electron bound with an atom. The photon disappears and the electron is removed from the atom and is free to migrate;
- Compton Scattering, when the photon experiences inelastic scattering off a bound atomic electron resulting in part of its incident energy being converted into the kinetic energy of the ejected election;
- $e^- - e^+$ pair production, when transformation of the photon energy into creation of the electron – positron pair takes place in the vicinity of an atomic nuclei.

The above processes lead mainly to the removal of photons from the incident beam. The whole process can be described as number of photons leaving the target I related the number of initial number of photons I_0 impinging on a target in a function of the target thickness x and the absorption coefficient μ, equation (1). The remaining fraction of photons that leaves the target either preserves the initial energy or experiences a decrease in that value often accompanied by a change to their direction with respect to their incidence. Therefore photon

beams are strongly penetrating and the estimation of an explicit range of a single photon is impossible.

$$I = I_0 \cdot e^{-\mu \cdot x} \quad (1)$$

Electrons which were liberated from the atoms often have enough kinetic energy to cause further ionisation of the surrounding atoms; these are called δ-electrons.

2.1.2 Interaction of charged particles with matter

The electric field of charged particles interacts with both electrons and atomic nuclei from the very moment the particles enter the target volume. Owing to their interaction mechanisms, they offer superior dose conformity as opposed to X-ray photons. The range of charged particles is finite when the thickness of the target is large enough and is a function of the initial kinetic energy. What is more, the maximum of energy deposition is located at the end of the particle range. In contrast, the maximum energy transfer for photon radiation happens in the build-up region, on entering the medium, which results in a deposition of significant dose in the skin of a patient. This significantly reduces application of conventional radiotherapy for deeply seated tumours, head treatments or when the size of the patient is large. A comparison of the discussed energy deposition mechanism for photons and charged particles, represented by carbon ions, where the dose was normalized to the value at the skin, can be examined in figure 4.

The concept of using protons in cancer treatment was brought forward by Robert Wilson back in 1946 at Harvard University. This has led to significant research and advance in charged particle beam delivery techniques, especially in the last two decades, in parallel with the ongoing refinement of conventional radiotherapy. The probability of complications in the healthy tissue can be significantly minimized for charged particle beams as the probability of recovery of the living cells is related to the transfer of energy per unit path length, called stopping power dE/dx. As a result proton therapy has become a desired treatment method especially in cancer treatments of lesions located in nervous tissue or in paediatric patients, where the healthy tissues are still in the development stages. [7] [10]

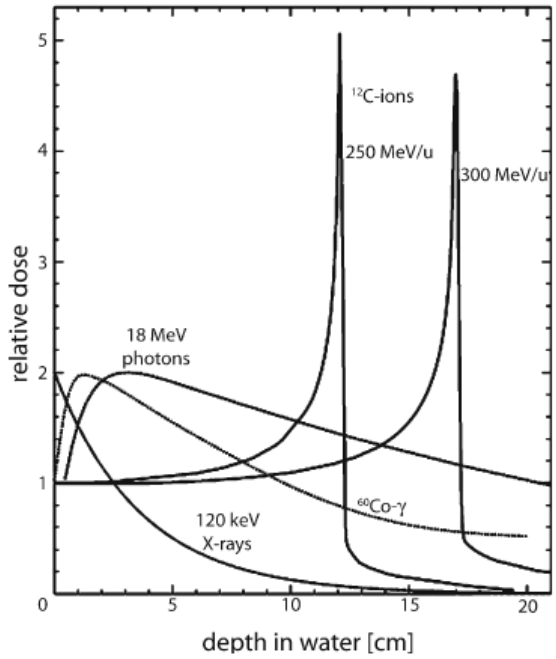

Figure 4: A comparison of depth dose curves for photon radiation and charged particles, where penetration characteristics can be observed with a pronounced Bragg peak terminating the range of the charged particles. [4]

The kinetic energy losses by charged particles follow the rules expressed by certain quantum mechanical probability of different interactions, however, they can be written down in the macroscopic formalism because of their path lengths covering ranges from a fraction of to a few tens of millimetres in the medical application. The small portions of energy transferred per unit length $\mathrm{dE/dx}$ are expressed in $\mathrm{MeV/cm}$ or are normalized to the density of medium ρ, noted as $\mathrm{MeV \cdot cm^2/g}$, when they become independent of the actual density of the material. There are a few major processes associated with energy loss and for the charged particles used in cancer treatment and three are of the largest significance:

- Inelastic collisions with atomic electrons constituting electronic stopping power $(\mathrm{dE/dx})_{\mathrm{el}}$, referred to as continuous slowing down approximation (CSDA);
- Elastic scattering from nuclei called nuclear stopping power that involves multiple Coulomb scattering (MCS), when the particle undergoes small deflections from the incident direction of travel, and nuclear reactions, $(\mathrm{dE/dx})_{\mathrm{nucl}}$
- Bremsstrahlung $(\mathrm{dE/dx})_{\mathrm{rad}}$, insignificant for protons and heavier ions but comprising a substantial contribution for electrons;

The value of total stopping power $(\mathrm{dE/dx})_{\mathrm{tot}}$ is a sum of the above three terms. On average, a $1\ \mathrm{MeV}$ proton experiences about 10^5 interaction before it is brought to a halt. Contribution from the nuclear interactions is much smaller than from CSDA and, in practice, the latter has the largest significance in the description of the energy transfer phenomena. The electronic stopping power was defined by Bethe in 1932 [11] and is described by a non-linear energy transfer rate in the target material per unit length, equation (2).

$$-\frac{1}{\rho}\left(\frac{dE}{dx}\right)_{el} = 2\pi \cdot N_A . r_e^2 \cdot m_e \cdot c^2 \cdot \frac{Z}{A} \cdot \frac{z^2}{\beta^2}\left(ln\frac{2m_e \cdot \gamma^2 \cdot V^2 \cdot W_{max}}{I^2} - 2\beta^2 - \delta - 2\frac{C}{Z}\right) \tag{2}$$

Where:

- r_e - Classical electron radius, $2.817 \cdot 10^{-13}$ cm;
- m_e - Mass of an electron, $9.109 \cdot 10^{-31}$ kg;
- N_A - Avogadro's number, $6.022 \cdot 10^{23}$ atoms/mol;
- I - Mean excitation potential of the target material determined empirically;
- Z - Atomic number of the target material;
- z - Charge of incident particle expressed in the units of e;
- β - Relativistic beta of a proton, $\mathrm{v/c}$, where v – particle speed;
- γ - Relativistic gamma;
- δ - Density correction;
- C - Shell correction;
- W_{max} - Largest possible proton energy loss in a single collision expressed by:

$$W_{max} = \frac{2m_e c^2 \beta^2 \gamma^2}{1 + 2 \cdot \frac{m_e}{M} \cdot \sqrt{1 + \beta^2\gamma^2 + \frac{m_e}{M}}} \tag{3}$$

- c - Speed of light;
- M - Mass of the incident particle.

The shell C and density δ corrections depend on the energy of the considered particle. The former accounts for the effects when the velocity of the particle becomes comparable with the velocity of the bound orbiting electron, including covalent bindings and must be included in

the above equation for $\beta \leq 0.05$. The latter, the density correction δ, is vital for higher energies of particles and must be included because of the polarisation effects that the Coulomb force of the incident particle has on the atoms of the target. Differences in the calculated energy loses are reported to reach about 10% of the actual value when no correction for density is applied. The effect is less important with an increasing atomic number value of the target. The Bethe – Bloch formula has got limitations when non-relativistic energies are considered and, as yet, there is no consistent model for particles characterised by $0.01 < \beta < 0.05$.

The value of the stopping power increases with the decreasing kinetic energy of protons, which is related to the term $1/\beta^2 \sim 1/\mathrm{E}^2$. The lower the speed V of a particle, the more time there is for interactions with the electrons. Furthermore, the stopping power is not only a function of the initial energy but also depends on the type of the target material. This explains the desired attribute of hadron therapy, as opposed to the conventional photon treatment, namely where the maximum of the energy deposition takes place in the tumour volume and permits to cover it with a homogenous dose distribution with a sharp fall off at the edges.

The small energy losses described by the CSDA mechanism and accumulation of minute deflections of protons from a straight like path result in broadening of their initial distribution in the lateral profile and determine the longitudinal distributions expressed as the depth of penetration. The processes linked with the above effects are consecutively called *multiple coulomb scattering* (MCS) and *longitudinal or range straggling*.

The range and path straggling have similar definitions, where the path length means an average distance travelled by a particle between the entrance to the target and to the end point where its kinetic energy is nearly zero and no more deflections are observed. Path lengths of a number of particles with the incident energy E_0 are always different, which results in different ranges defined as the mean depth of penetration measured along a straight line parallel to the incident direction. The range is always smaller than the path length because of multiple Coulomb scattering that particles experience and can be calculated from equation (4).

$$R(E_0) = R(E_r) \cdot \langle cos\theta \rangle + \int_{E_f}^{E_0} \langle cos\theta \rangle \left(\frac{1}{\rho}\frac{dE}{dx}\right)^{-1} dE \qquad (4)$$

The $\langle \cos\theta \rangle$ is the average cosine of the angle defined between the initial direction and the direction of their travel at the end of the path length at the energy $\mathrm{E_r}$. The value of $\mathrm{E_r}$ is set to

zero when a particle has energy of 10eV. [11] MCS is used mostly with regard to protons whilst alpha particles or ions with larger Z do not undergo so many deflections. This is linked with their mass and as a result, the range is convergent with the path length. The statistical approach of deflections leads to a distribution of protons at the end of their path to take Gaussian shape. [3] The probability of a reverse scattering event is very low and most of the scattering happens in the forward direction, with deflections not higher than a few degrees from the initial path. [10] Likewise, the low energy of the treatment beam at CCC means that protons are more prone to deflections in the plane transverse to the direction of their movement, resulting in a larger lateral spread. Ultimately, a standard deviation of the Gaussian distribution can be found using empirical equation (5). [12]

$$\sigma = \frac{13.6\ MeV}{\beta cp}\sqrt{\frac{l}{X}}\left(1 + 0.038 \cdot \ln\frac{l}{X}\right) \tag{5}$$

Where p is the proton momentum, l is the path length in a medium and X is the radiation length. [13]

Nuclear reactions are divided into two groups, explicitly *elastic* and *inelastic*. When a proton scatters elastically off a nucleus, it can leave it in either a ground or exited state. Inelastic collisions take place when the impinging proton is involved in collisions with protons or neutrons in a nucleus. This leads to the emission of secondary fragments, which carrying charge, are capable of further ionisation of the target material around that region. In principle, these fission elements contribute to the ionisation only locally.

The nominal beam energy from the Scanditronix MC60-PF cyclotron at CCC $\mathrm{E_{nominal}} = 62.0\ \mathrm{MeV}$ was checked with a set of the aluminium foils during the commissioning of the accelerator. The thickness of aluminium, required to fully stop the beam, was found to be approximately $\mathrm{d_{Al}} = 4.35\ \mathrm{mm}$. [15] The value was used as a first approximation of the minimum required thickness of the FC beam stopper for the non-invasive beam current monitor set-up discussed in this thesis.

This energy transfer along a path of a particle can be associated with the energy deposited at the consecutive locations. The fundamental relation of the two values is expressed by equation (6).

$$D = \Phi \cdot \frac{S}{\rho} \tag{6}$$

Where:

D - Dose deposited, $Gy = J/kg$;

Φ - Fluence of protons, $1/m^2$;

S - Stopping power, MeV/m, where $1MeV = 1.602 \cdot 10^{-13}J$;

ρ - Density of the target material, kg/m^3.

In unison, the dose rate can be expressed as a function of the proton beam current, equation (7). The relation demonstrates a purely linear behaviour and is based on an assumption that the proton fluence takes place through an area A:

$$\dot{D} = \frac{i_p}{A} \cdot \frac{S}{\rho} \tag{7}$$

Where:

i_p/A - Proton current through a surface A, $\mathrm{A/m^2}$;

$\dot{D}$ - Dose rate, $\mathrm{Gy/s}$.

Following this equation, the expected dependence of the signal induced in the VELO detector, measured in the beam halo region, should be a linear function of the beam current.

2.2 Accelerators as proton sources in proton therapy

Hadron therapy requires reliable beam delivery. This is achieved when both the choice and performance of an accelerator and the beam transport line are optimised to give a required beam spot size at the treatment iso-centre. The treatment field sizes range from as small as 1cm to 25 cm in diameter. Therefore, there have been various methods developed to provide uniform dose distribution coming from protons or heavier ions in the tumour volume. In general, there are two types of the beam delivery systems:

- Scattering, where a system of scattering foils broadens the beam laterally to a quasi-Gaussian shape and only the central part of it is selected to pass though the treatment nozzle located before the iso-centre.
- Scanning, where a pencil beam is scanned across the beam volume using magnetic steering and variable energy values.

The scattering method is widely used in ocular lesion treatments, which is preferential for low energy protons produced by cyclotrons. There are a number of additional associated devices that support conformance of the dose with the treatment volume because the delivered beam is quasi mono-energetic and has a strictly defined range. Acquiring smaller ranges requires manipulation of the beam energy and is supported with range shifters, range modulators, compensators and ultimately moulded by custom made apertures. Scattering leads to the contamination of the proton beams with neutrons released from the nuclear reactions in the above elements outside the patient and builds an undesired additional dose deposition in the treatment.

The scanning method can be divided into three further sub-groups that were devised and adopted at various treatment centres:

- Discrete Spot Scanning which is a step and shoot approach delivering the beam one spot next to another with the beam off intervals when the steering magnet adjustments take place;
- Raster scanning, which is scanning the target volume with the beam across a transverse plane to the beam direction at the same depth with a continuous beam delivery;
- Dynamic spot scanning, which is the most advanced method and additionally the beam energy is also varied during same delivery.

The disadvantages of these methods originate from the technical constrains in production of pencil beams with sharp edges (penumbra) and are more susceptible to organ motion. Moreover, the scanning method necessitates varying energy and the choice of an accelerator is very crucial to meet that requirement.

Historically, proton beams for medical uses were delivered at research centres using existing cyclotrons or synchrocyclotrons. At present, hadron therapy centres use mainly dedicated accelerators that are based on two types of machines:

- Cyclotrons;
- Synchrotrons.

There are significant differences between them in terms of the design and operation principles, space required and achievable beam energies. Therapeutic proton beams must cover range of energies between $60\ \mathrm{MeV}$ for ocular treatments to $230\ \mathrm{MeV}$ for tumours situated in other, deeper located organs of human body. Nowadays both types of machines are able to provide beam energies in the upper limit.

Cyclotrons produce proton beams with only one fixed energy. They are uncomplicated in terms of their design or injection mechanism of protons for acceleration, where injectors are incorporated in the centre of the machine. The lower treatment energies can also be achieved through interactions with energy degraders installed in the beam lines. This comes though at the cost of a decrease of the beam production efficiency, induced radioactivity of the beam line elements and an increase of the emittance [57] and energy spread.

Synchrotrons are circular machines that rely on multiple pass of protons or heavier elements through the accelerating sections. The magnetic field determining the orbits of the circulating particles is ramped up with their increasing energy. Therefore synchrotrons are a source of a wide energy range and intensity of particles that are used in the in scanning delivery methods. They require much more space than cyclotrons and additionally an injector linear accelerator must be accommodated alongside with them for pre-acceleration.

The Clatterbridge Cancer Centre operates a Scanditronix MC60-PF cyclotron for the ocular treatments. Cyclotrons are dipole magnet based accelerators, developed by E. Lawrence in 1932, that use a constant synchrotron frequency ω_0 of protons revolution where their path is circular and determined by a fixed value of magnetic field B_0 perpendicular to the direction of the motion. For non-relativistic particles this is described by equation (8), for $\gamma \approx 1$. Protons gain kinetic energy in a gap between two accelerating electrodes with the polarisation oscillating at an RF frequency chosen to match the revolution frequency, that is $\omega_{\mathrm{RF}} = \mathrm{h} \cdot \omega_0$, where h is a harmonic constant $\mathrm{h} = 1, 2,$ etc (figure 5). As a result at every crossing of the gap protons experience only accelerating potential from the electric field. The cyclotron frequency is obtained by equating the centripetal force and the Lorentz force, and for a given magnetic field strength the revolution frequency can be found:

$$\omega_0 = \frac{qB_0}{\gamma m} \tag{8}$$

Where:

m - Mass of a proton, kg;

ω_0 - Frequency of the RF field, $1/\mathrm{s}$;

γ - Relativistic gamma.

The acceleration at CCC is for the first harmonic, when the frequency of the RF field is equal to the cyclotron frequency. The relativistic increase of the mass with energy, when $\gamma > 1$, requires adjustments of the magnetic field to maintain the revolution synchronism and assure that protons on all the accelerating orbits arrive at the accelerating gap at the same. This had been solved by R. Thomas by introducing shaping of the magnets into sectors creating called hills and valleys, where the strength of the magnetic field varies along both the radius and the circumference of orbits. This concept has been used in the cyclotron designs since then and is known as an isochronous cyclotron.

Extraction of protons from the last orbit is very challenging as with the increasing kinetic energy the radii of the consecutive orbits are very close one to another and obey the equation (9). Therefore the extraction, depending of the chosen method, can partially strip inner orbits along with protons on the last orbit introducing a larger energy spread.

$$r = \frac{1}{B} \cdot \left(\frac{2mV_0}{e}\right)^{1/2} N^{1/2} \tag{9}$$

Where : N - revolution number.

The synchronisation of with the RF field frequency is also applied to the injector inside a cyclotron. The most commonly used and simplest type of injector is a cold-cathode Penning Ionisation Gauge (PIG). [18] The principle of operation is based on creating plasma between the two cathodes, which are placed at two opposite sides of a metal cylinder constituting an anode.

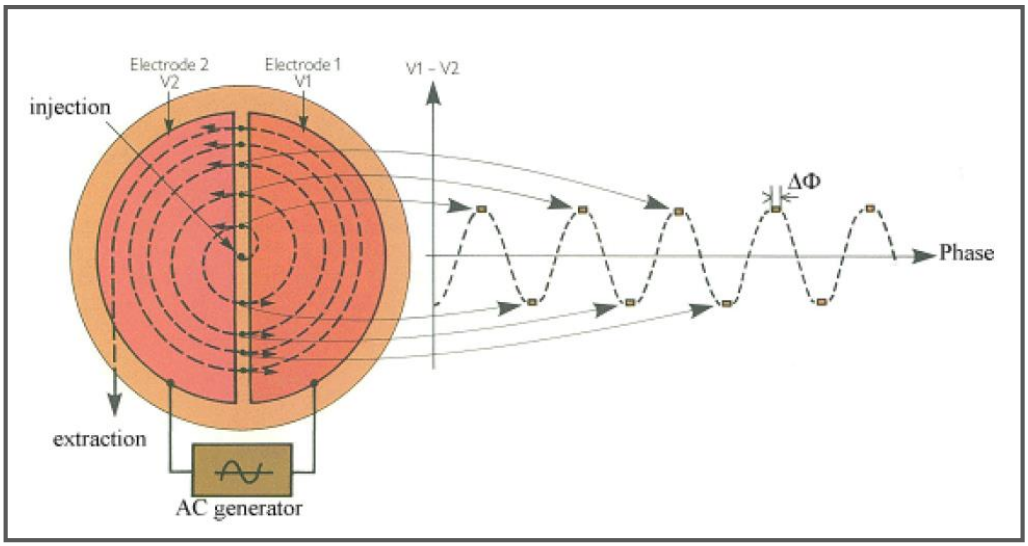

Figure 5: Principle of operation a cyclotron. [17]

The magnetic field of the cyclotron penetrates inside the cylinder and at any point is perpendicular to the cathodes situated at the two opposite sides on the central axis. Electrons emitted from the cathodes spiral around the magnetic field lines keeping their concentration at the very high levels, what enhances creation of plasma in the gas injected to the cylinder. Once a plasma is created, the voltage on both cathodes is increased to a few kV to trigger an arc current to promote the ionisation. Extraction of the created ions from the PIG source happens though a small slit in the side wall of the cylinder by a puller integrated with the accelerating electrode. This attracts the ions out, where they exhibit the principle acceleration in the cyclotron.

The main beam parameters and characteristics important for the project work associated with the cyclotron at CCC are presented in the following section.

2.3 Clatterbridge Cancer Centre treatment line

The Douglas Cyclotron Department at CCC remains the only proton therapy centre in the UK, and has been an important facility for many research projects in both medical physics and accelerator science. In 1998 the emittance measurements were performed on a part of the beam line used for the production of ^{18}F isotope (by J.A. Clarke et al.) to assess the suitability of the cyclotron for an energy upgrade by adding a booster LINAC at the extraction point. [19] Also, the treatment beam characteristics were modelled in 2006 by Colin Baker et al. using three different Monte-Carlo codes with the aim to simulate the transport of a $\mathrm{E_{nominal}} = 62.0\ \mathrm{MeV}$ proton

beam through the scattering foils, range shifter and modulator. In this way the depth and the radial dose profiles of the beam in water at the iso-centre were determined. [20] These studies, however, did not take into account the actual beam Twiss parameters at the position of the scattering foils as an input.

The Scanditronix MC-60 PF cyclotron was installed at CCC in 1984 for neutron therapy but the offered proton energy allowed as well for using them in therapy of ocular tumours. With the support from the Imperial Cancer Research Fund, a new ocular treatment room and beam line were added and the first treatment was delivered in 1989. [21]

By the design, the beam has to travel an overall distance $\Delta z = 16.0\ \mathrm{m}$ between the extraction point from the cyclotron to the scattering foils system in the treatment room. The beam line consist of two straight sections joined by a dipole switching magnet situated in the vault, where protons are diverted by an angle $\alpha = 5°$ with respect to the initial direction. A set of three quadrupole magnet triplets provide strong focusing [57] of the beam in both the vertical and horizontal planes (figure 6). A number of XY steering magnets are additionally used to correct for any deflections of the beam from the theoretical beam axis.

The beam line is terminated with a system of tungsten double scattering foils, each $25\ \mu m$ thick, which spreads the beam in the transverse direction to obtain a Gaussian-like distribution. Beyond this point, the beam leaves the vacuum pipe through a $50\ \mu m$ thick Kapton window. The rest of the beam path until the treatment iso-centre is in air. There are a number the beam shaping and monitoring elements on the way, which are distributed at different distances from the last scattering foil (figure 7):

- Modulator box hosting the energy shifter and beam modulator;
- Drift space;
- Main box, containing:
    a) Parallel –plate ionisation chambers for the dosimetric control;
    b) Retractable X-ray positioning panels;
    c) Alignment cross;
    d) Brass nozzle which terminates the box and is used for fixing the patient specific brass-milled apertures. The distance from the last scattering foil to the end of the nozzle is $\Delta z = 146.6\ cm$.

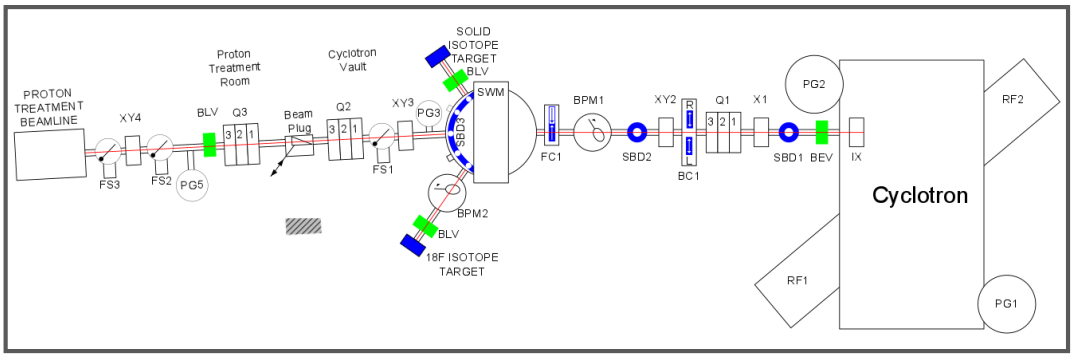

Figure 6: A schematic layout of the Scanditronix MC-60PF cyclotron at CCC. RF1 and RF2 are the Radio-frequency power supplies; Q1, Q2 and Q3 denote the focusing quadrupole magnet triplets and SWM stands for switching magnet, which can direct the beam to one of the three branches of the beam line.

The nozzle is also used to mark the treatment iso-centre with a termination pin slotted at the end, which gets aligned with a dedicated metal pointer affixed to the treatment chair to calibrate the chair position. The chair pointer was employed to achieve the alignment of the non-invasive beam current monitor introduced in this dissertation with the beam cardinal axes, namely horizontal and vertical.

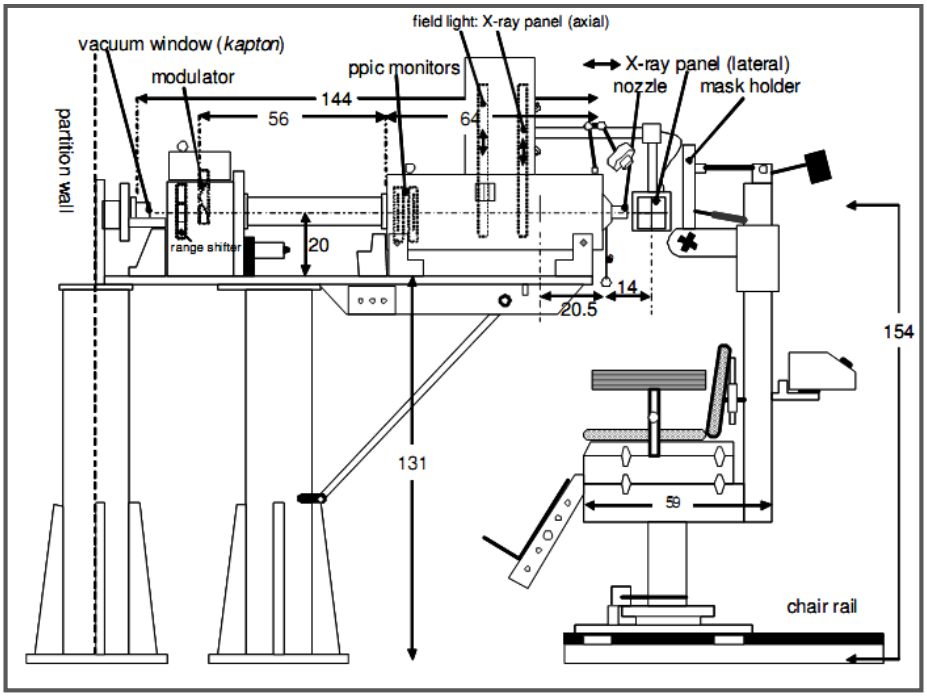

Figure 7: The layout of the treatment line in the treatment room at CCC. [5]

A dedicated model of the beam line was created, based on the above dimensions, to simulate the transport of the beam and estimate the evolution of the beam halo. Results of the modelling are presented in chapter 5.

Detailed knowledge on the beam characteristics was essential for the project to determine the time structure of the beam, which determined the design of the impedance-matched FC. The detector was intended to provide wide bandwidth with an intention of resolving the bunch separation and bunch shape for the provisioned future developments of the proposed non-invasive monitor method. The time and current structure of the beam for the Scanditronix MC-60PF cyclotron at CCC are summarized in tables 1 and 2.

Table 1: Time structure of the beam from the Scanditronix MC60-PF cyclotron. [15]

Max. kinetic energy $[\mathrm{MeV}]$	62.0
Ion type	p^+
RF frequency $[\mathrm{MHz}]$	26.70
Harmonic mode	1.0
RF beam acceptance $[\mathrm{deg}]$	13.0
Bunch length $[\mathrm{ns}]$	1.37
RF period $[\mathrm{ns}]$	37.45
Bunch repetition time $[\mathrm{ns}]$	37.45

Table 2: The proton beam parameters for the Scanditronix MC60-PF cyclotron based of the nominal values used in the treatment.

Average beam current $[\mathrm{nA}]$	5.0
Bunch peak current $[\mathrm{nA}]$	138.5
Number of ions $[\mathrm{ions}\ /\ \mathrm{s}]$	$3.12 \cdot 10^{+10}$
Number of ions per bunch	$1.17 \cdot 10^{+3}$
PIG source current $[\mu\mathrm{A}]$	$1.38 \cdot 10^{-1}$

Chapter Summary

This chapter comprised of an introduction to the interaction mechanisms of charged particles with matter with a particular focus on their application in cancer therapy and compared them to the conventional radiotherapy methods using X-rays. The elements of hadron therapy delivery systems were outlined showing their importance in the beam delivery by relating the physical beam characteristics with their clinical use. Ultimately the layout of the proton facility at the Clatterbridge Cancer Centre was introduced presenting the expected time structure and beam currents according to the technical specification of the cyclotron.

3. FARADAY CUP

Beam current measurements constitute an essential part of diagnostics for many accelerators as they are used for the constant monitoring of a given machine performance. The choice of a beam intensity measuring detector depends on the set requirements and utilises various particle detection techniques. The most versatile beam monitor and also the simplest possible solution for measuring currents for a variety of particle species is a Faraday Cup (FC). The design of the detector can be easily optimised to minimize effects arising from interactions with the measured beam. There is, however, a limit of the FC application when either the beam energy or current become very high. In these cases thermal aspects of operation start influencing the size of the FC and become critical factors in the design. [24] On many sites FCs cannot be used and non-destructive methods prove to be a better solution, e.g. on circular machines such as storage rings or synchrotrons.

For the application of the non-invasive beam current monitor discussed in this dissertation, the FC was identified as the most straightforward in implementation, simplest in handling and also as a cost effective solution for delivering readings of the absolute beam current. The different physical properties of the detector had to be carefully modelled to minimise possible signal losses when interacting with the proton beam at CCC. Therefore, phenomena associated with the irradiation of metal surfaces with proton beams were studied. Impedance matching was incorporated in the conceptual design to enhance the signal transfer quality by equalising electromagnetic wave propagation characteristics with those of the readout transfer lines. Although it was not foreseen at this stage of experiment to have bunch-to-bunch correlation of signals from both detectors, this option was exercised and enabled for future development of the monitor and the method. The bunch-to-bunch correlation required extensive modifications applied to the VELO detector electronics, as outlined in chapters 1 and 4, and was not envisaged at the stage of the experiment planning.

This chapter summarises the design steps taken to introduce the beam current measurements with the FC and justifies its application against ionisation chambers. It describes the results of the Monte-Carlo modelling of the signal losses due to ion-induced electron emission and finally presents the results of signal properties and the ability of the device to resolve beam time structure.

3.1 Gas detectors constrains

Ionisation detectors have been the longest used type of radiation detectors in physics experiments and are also widely used in radiotherapy for the quality assurance of the therapy beams. They rely on direct ionisation of gas contained inside them and further collection of the released charges on electrodes. They offer a very simple design and easy maintenance.

There are three basic types of gas detectors: ionisation chambers, proportional counters and Geiger-Mueller counters, which correspond the regions depicted in figure 8. All three can have the same architecture, however, differences arise in terms of applied potential, gas mixtures, to tailor their properties by either enhancing or quenching electron – ion pair production.

When radiation penetrates the volume of the detector, a certain number of electron hole pairs are created. In the absence of an external electric field, they would come to the thermodynamic equilibrium and recombine. An applied field leads to separation of the charges and electrons are accelerated toward the anode and ions towards the cathode.

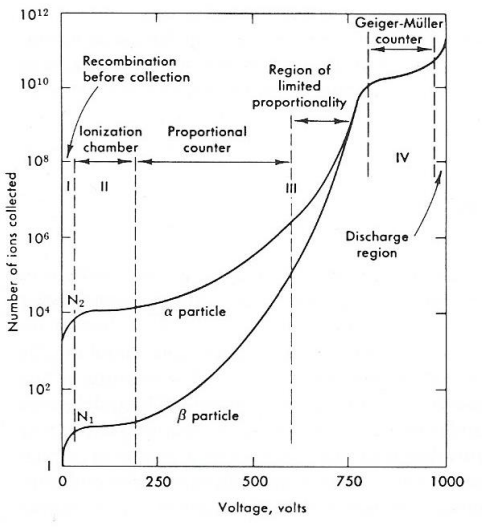

Figure 8: Dependence of the number of ions collected on electrodes versus applied voltage for a single wire gas chamber. [3]

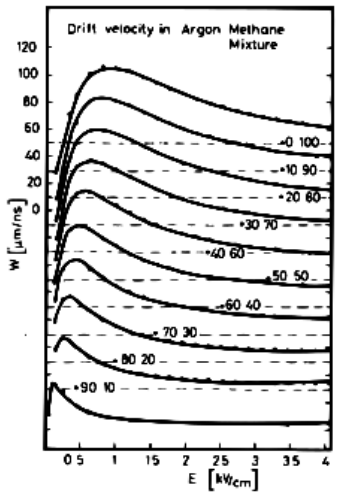

Figure 9: Velocity curves of electrons dependence on the electric field value for Argon Methane mixture. [3]

The ion collection curves in figure 8 illustrate the total charge collected on an electrode as a function of electric field V applied between the anode and cathode. The increasing voltage

gradually gives rise to an electric current in the readout circuit as more and more electron – ion pairs are separated in the volume of the detector. This continues until the first plateau region is reached (II), which is specific to the ionisation chamber operation, as a result of separation and collection of all the electron-ion pairs induced by passing radiation. The recorded currents are very small, normally in the order of 10^{-12} A or less, and must be measured by electrometers. The ionisation chambers are therefore suitable for measuring either gamma rays or radiation fields with very large particle fluence.

The motion of electrons and ions is an essential factor influencing the operating characteristics of gas detectors. There are two phenomena describing their movements; these are diffusion and drift in electric field. The former takes place in the absence of the electric field and is directly linked with the thermal velocities of the charges ruled by the Maxwell distribution [25] of mean speed that is proportional to the square root of temperature. This determines the spread of charges in a given time interval from the point of origin. The latter, when the electric field is present, forces additional acceleration of the charges. Raising the electric field introduces larger acceleration, however the final speed is limited by collisions with gas molecules. This can be described in terms of their mobility μ defined as:

$$\mu = \frac{u}{E} \tag{10}$$

where: u - Drift velocity, m/s;

E - Electric field, V/m.

The mobility of electrons is much higher than of ions and, therefore, their μ becomes a strong function of electric field E. The pulse formation in the readout circuit depends on both the geometry of the chamber, which influences the inherent capacitance, and the capacitance of the readout circuit. The shape of the pulse can be derived from the conservation of energy, where the energy stored in the electric field can be split into three components:

- Energy absorbed by ions;
- Energy absorbed by electrons ;
- Remaining stored energy.

The pulse rise measured across a resistance in the readout circuit cab be described by equation (11).

$$V_R = \frac{n_0 \cdot e}{d \cdot C} \cdot (\mu_{ions} + \mu_{electrons}) \cdot t \quad (11)$$

Where: n_0 - Number of electron-ion pairs produced;

e - Elementary charge, $1.602 \cdot 10^{-19}\mathrm{C}$;

d - Distance between the anode and the cathode, m;

C - Capacitance of the readout system and the detector, F;

t - Time of drift, s.

After time t larger than the drift time of ions, the registered maximum amplitude of the signal follows the relation in equation (12) and is not dependent on the point of charge creation. This holds for the readout circuit time constant being larger than mentioned time drift of ions, $\mathrm{RC} >> \mathrm{t_{ions}}$.

$$V_{max} = \frac{n_0 \cdot e}{C} \quad (12)$$

The charge collection from ions can be neglected when the time constant of the readout circuit is small compared to their collection time. Then, only the fast rising portion of the signal is registered from electrons and the chamber is said to be operated in an electron sensitive mode. Nonetheless, the charge collection time and the capacitance of the whole system influence significantly the time characteristics of ionisation chamber measurements. The separation between the electrodes is normally around a couple of millimetres, which combined with a limited operating range of applied potential and drift time constraints, ionisation chambers have limited application in fast timing experiments. An example of the mobility of electrons versus the applied voltage can be examined in figure 9, where μ is lower than $40\ \mu\mathrm{m/ns}$ for $\mathrm{E} \approx 100\ \mathrm{V/cm}$. For a classical parallel-plate ionisation chamber used in radiotherapy the charge collection is at the order of $\mathrm{t} = 100\ \mathrm{ns}$. As a consequence ionisation chambers are unsuitable to examine the pulse shape and a faster detector had to be considered for the proposed non-invasive beam monitor. For this reason a Faraday Cup with a large bandwidth was chosen, which offered the possibility to investigate the shape of single bunches.

The design steps and testing of the device are therefore subject to discussion in the following sections.

3.2 Beam intensity measurement principles and Faraday Cups

FCs are very simple and reliable devices for absolute beam current determination. In principle, an FC is a *beam stopper*, often called a *charge collector*, integrating charge carried by the particles in the beam by terminating them in the bulk of a conductive material. The beam stopper is isolated from the housing chamber and at the same time grounded through a charge meter. Despite the simplicity of the design and operation, FCs are destructive monitors unsuitable or even undesirable in many applications, e.g. on synchrotrons that rely on an undisturbed multiple pass of particles through the machine. Therefore the charge measuring detectors comprise of two fundamental types, depending on the implemented detection method, that are *invasive* and *non-invasive*. Their specific application normally implies their choice and depends on the parameters of the monitored accelerator, e.g. type of accelerated particles and their energy, intensity of the beam and time structure (DC or pulsed) or simply space available for integration. Machines with high energy and intensity of beams are more likely to be monitored by indirect methods such as beam transformers or capacitive pick-ups [23] [24]. Their principle of operation is based on picking up either electric or magnetic field of particles. The measured currents are estimates of real values due to their indirect interaction with the beam. They are extensively used across many electron or proton machines where the intensities are high enough to overcome noise limitations originating from associated readout electronics, e.g. accelerator RF system or simply quantisation of charge. The low intensity beams are more likely to be monitored with direct measurement methods, such as particle counting or FCs, offering better detection accuracy. Their operation relies on direct interactions with the structure of the detector that can result in either collection of the particles or lead to kinetic energy losses when traversing the medium, which leads to ionisation or emission of optical photons. The strength of the induced signal is directly proportional to the amount of deposited energy at the cost of perturbation or destruction of the beam. Therefore, these detectors are preferable either during commissioning of a given machine or for daily checks on LINACs or cyclotrons instead of implementation as in-treatment online monitors. FCs can also be used as

simple beam stoppers on medical accelerators, e.g. at Clatterbridge Cancer Centre or Paul Scherer Institute.

It was highlighted in the previous chapter that cyclotrons are RF-powered accelerators. Their bunch structure can be characterised by two parameters: the cyclotron frequency as an equivalent of the bunch repetition frequency and the phase acceptance of the cyclotron that corresponds to the bunch length. Therefore, the measured beam current can be described by two equations (13) and (14).

$$I(t) = \frac{n \cdot \varsigma \cdot e}{t} = \frac{Q}{t} \tag{13}$$

$$Q = \int_{t}^{t+T} I(t)dt \tag{14}$$

where:

n - Number of particles;

ς - Charge state of the particle, for protons, $\varsigma = 1$;

e - Charge of an electron, e $= 1.602 \cdot 10^{-19}$C;

t - Time representing either repetition period T or angular acceptance of the RF in the cyclotron (expressed in time), s;

Q - Total charge, C.

Eventually, the above values of current can be stated as either average or peak representation for a bunch.

The beam stopper accepting the impact of particles must be larger than the stopping range of protons. The latter can be obtained using the Bethe-Bloch formula in equation (2) [28], where the stopping range increases with the kinetic energy of the impinging particles. This requires larger longitudinal dimension of a collector, what becomes disadvantageous because of an increase in weight.

Termination of particles in the bulk of metal results in the device acquiring charge, where the amount of charge can be measured by grounding it through a current meter (figure 10). The appropriate type of readout electronics depends on the beam time structure, where DC-

beams are measured with electrometers whilst oscilloscopes or integrating picoammeters provide output measurements for pulsed beams. FCs are suitable for low current measurements at the level of pA and nA [23], although there are reported examples of FC designs for high power beams. [27] As a consequence of the measurement method based on particle termination, the power carried by the beam is deposited in the material and must be very often efficiently dissipated. There are different methods for conductive cooling of FCs available that come at a cost of signal quality degradation by introducing additional noise sources to the system, including leakage currents.

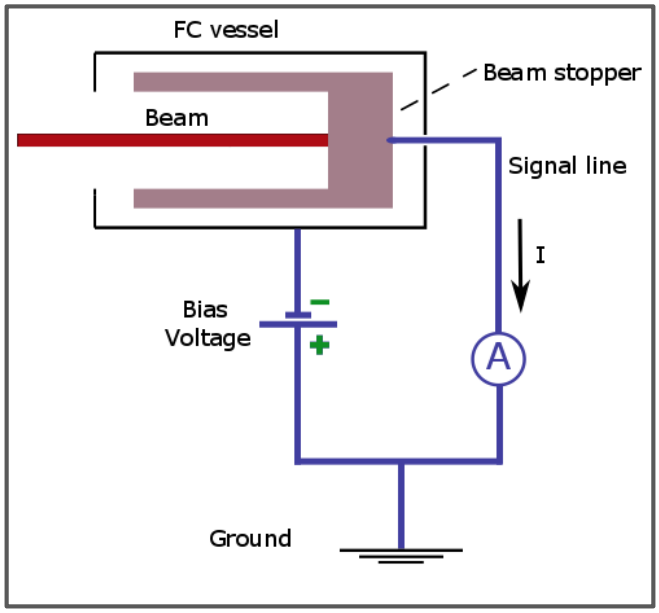

Figure 10: Schematic view of the Faraday Cup operation principle.

In the discussed application of the FC, the impinging protons hit the metal target surface at a normal angle, where they can either completely stop in the beam stopper undergoing many interactions, Their kinetic energy loss takes place through many Coulomb interactions with atom electrons, outlined in chapter 2, resulting in phenomena that may lead to their emission from the surface of the charge collector and further escape to the surrounding vacuum. These losses affect the recorded electric current readings by a meter and should they remain unsuppressed, a higher value of the reading will be observed. Suppression of proton-induced electron fluence incorporate a variety of methods, where a very basic solution includes adjusting the geometry of the collector in a way that the emission rate is decreased by recollecting the electrons emitted at the large angles to the normal to the target surface. Additionally, for electron energies below

$1\ \mathrm{keV}$ electrostatic suppression can be incorporated with a guarding ring biased with negative voltage that is fitted at the entrance to the charge collector. Alternatively, either the beam stopper of the whole housing vessel can also be biased, illustrated in figure 10. The external potential will have an effect on electron paths by reversing them to the beam stopper and as a consequence improving the accuracy of the measured current. More detailed elucidations on ion-induced electron emission will be covered in the following section.

Electron emission can be further enhanced by heat deposited by the beam in the collector, where the increase in temperature of metal promotes their thermal emission. For that reason addressing the thermal aspects of a FC operation is essential in designs for beams with higher intensities or energies. No special considerations are required unless heat delivered to the beam stopper exceeds several Watts. [23] For the proton beam at CCC the estimated energy deposition was obtained using the formula (15). There, the number of protons N arriving at the target in a given time interval dt is equivalent to the ratio of beam current I and elementary charge e .

$$P = \frac{I}{e} \cdot W \tag{15}$$

where:

I - Beam current, A;

P - Power of the beam, W;

e - Elementary charge, $1.602 \cdot 10^{-19}\ \mathrm{C}$;

W - Kinetic energy, where $1\ \mathrm{eV} = 1.602 \cdot 10^{-19}\ \mathrm{J}$.

The estimated power of the treatment beam at CCC is $\mathrm{P} = 0.3\ \mathrm{W}$ for the nominal parameters specified in the technical documentation, $\mathrm{E_{max}} = 60\ \mathrm{MeV}$ and $\mathrm{I} = 5 \cdot 10^{-9}\ \mathrm{A}$, and it falls below the previously mentioned threshold meaning that the radiative cooling in this case is sufficient.

FCs are characterised by low bandwidth with a maximum around 10 MHz and they are unsuitable for measuring high frequency beams. [23] There are, however, methods to improve their frequency response that originates from microwave theory. [26][29] The conceptual design

of the non-invasive beam current monitor described in this dissertation assumes only correlation of the average signal measured by the VELO in the proton beam halo region with an average value of the current measured by the FC. Otherwise, the complex readout electronics of the VELO would require extensive modifications, including a new design of the optical triggering system, in to order to look at consecutive bunches from the accelerator. Nevertheless, bunch-to-bunch measurements have not been excluded form the future use of the discussed method and accordingly the conceptual design of the FC provisioned resolving the bunch repetition frequency and shape, despite the fact that the RF field frequency of $\mathrm{f_{RF}} = 26.7\ \mathrm{MHz}$ is higher than the stated capabilities of FCs. A wide bandwidth FC can be produced when the impedance of the system, determined by a coaxial geometrical arrangement between the beam stopper and the hosting vessel, is matched with the impedance of the readout transfer line. The readout systems usually use coaxial cables with the impedance $\mathrm{Z} = 50\ \Omega$ that in an ideal situation do not have any cut off frequencies for the transport of the transverse electro-magnetic modes (TEM). [26] Additionally, the FC is connected to the coaxial cable through a $50\ \Omega$ coaxial feed-though constituting a barrier between the vacuum in the vessel and atmosphere.

There have been several designs of impedance matched monitors reported in literature. Their detailed design specifications can be found in references [29], [31] and [30]. For the discussed application, to resolve single bunches from the CCC cyclotron, the system is required to have a bandwidth better than the pulse repetition frequency $\mathrm{f_{RF}} = 26.7\ \mathrm{MHz}$, meaning that bunches arrive every $\mathrm{t} = 37.45 \cdot 10^{-9}$ s. The angular acceptance of ions from the ion source $\alpha \approx 13°$ corresponds to an approximate value of the bunch length of $\mathrm{t} \approx 1.35 \cdot 10^{-9}$ s (table 1). Therefore the minimum bandwidth $\mathrm{BW_{min}}$ for $-3\ \mathrm{dB}$ cut off frequency required to resolve the shape of a single bunch can be estimated by the following formula:

$$BW_{min} = \frac{0.35}{t}\ [Hz] \tag{16}$$

where:

t – Pulse width, s.

The system shall eventually have the bandwidth above $\mathrm{BW_{min}} = 259\ \mathrm{MHz}$.

The dimensions of the impedance matched collector and housing have to be adjusted according to the formula describing characteristic impedance of a coaxial line for transverse electromagnetic wave (17). [26][29]

$$Z_0 = \frac{1}{2\pi} \cdot \sqrt{\frac{\mu}{\varepsilon}} \cdot \ln\left(\frac{D}{d}\right) \tag{17}$$

where:

Z_0 – Impedance of the transfer line, $\mathrm{Z}_0 = 50\ \Omega$;

μ - Permeability of vacuum, $1.256 \cdot 10^{-6}\ \mathrm{H/m}$;

ε - Permittivity of vacuum, $8.854 \cdot 10^{-12}\ \mathrm{F/m}$;

D - Diameter of outer conductor, m;

d - Diameter of the collector, m.

To preserve the impedance $\mathrm{Z} = 50\ \Omega$ the ratio between the diameters should be kept at 2.3. This geometrical prerequisite appeared to be impractical in terms of both the dimensions of the whole device and the cost associated with the production, where the diameter of the collector $\mathrm{d} = 10\ \mathrm{cm}$ would have required the diameter of the housing vessel to be of $\mathrm{D} = 23\ \mathrm{cm}$. This would have had an adverse impact on both the manual handling and transport between the Cockcroft Institute and CCC due to the significant weight.

As a result, the transverse dimensions of the collector were decreased by decreasing the thickness of the side walls around the cavity of the beam stopper (figure 21). The thickness of the side walls were not significantly constrained by the proton range at their maximum energy, as they did not experience the direct impact of the beam unlike the target surface. Under the given circumstances, the beam stopper was accommodated in a DN100CF reducer cross. The diameter of the cavity $\Phi_{\mathrm{cavity}} = 4.0\ \mathrm{cm}$ at the entrance remained unchanged because of the maximum transverse dimensions of the beam at the iso-centre, $\Phi_{\mathrm{beam}} = 3.6\ \mathrm{cm}$. Consequently the impedance was reduced to approximately half of the anticipated value at the cost of introducing reflections of the signal. Re-arranging equation (17), a new diameter of the beam stopper was found, $\mathrm{d} = 63\ \mathrm{mm}$, for that given vessel and the impedance value calculated for the above dimensions should be $\mathrm{Z} \approx 27.7\ \Omega$. Electrical insulation of the beam stopper from back

flange was achieved with a PTFE disk introduced between them. The thickness of the latter was found to match the assumed impedance of the $25\ \Omega$ between the back of the collector and the metal support following the formula for the TEM mode of a parallel – plate waveguide, where the characteristic impedance is expressed by formula (18). [26][30]:

$$Z = \sqrt{\frac{\mu}{\varepsilon}} \cdot \frac{x}{d} \tag{18}$$

where:

μ - Permeability of PTFE;

ε - Permittivity of PTFE;

d - Diameter of the collector, m;

x - Thickness of the PTFE, m.

The estimated thickness of PTFE shall be about $\mathrm{x} = 12\ \mathrm{mm}$.

The bandwidth limit of the FC was also found with equations (19) and (20). [31]

$$\lambda_C = \pi \cdot (R + r)\sqrt{\varepsilon} \tag{19}$$

$$f_C = \frac{c}{\lambda_C} \tag{20}$$

where:

λ_C - Cut-off wavelength, m;

R - Inner radius of the vessel, m;

r - Radius of the collector, m.

The estimated cut-off wavelength was found to be $\lambda_c \approx 0.290\ \mathrm{m}$, which corresponds to the maximum bandwidth cut-off frequency $\mathrm{f_c} = 1.0\ \mathrm{GHz}$.

As mentioned, the decision to halve the initial impedance of the system resulted in introducing reflections of the signal at the transition points where the impedance mismatch takes place. The reflections influence the signal readout in two locations:

- At the connection of the beam stopper and the transfer line where part of the signal is repelled with opposite amplitude.
- At the face of the beam stopper where the second reflection takes place. Here the reflected signal has the same sign and amplitude following the phenomena of reflection in an open-end transmission line, equivalent to the termination with impedance $\mathrm{Z} = \infty$.

Whenever a transmission line of the characteristic impedance Z_0 is fed to another transmission line of a different characteristic impedance Z_1 and the load impedance has no reflections from the other end (e.g. terminated with its own characteristic impedance), a reflection coefficient Γ can be derived and is described by equation (21). At the same time, the transmission coefficient can be found and is expressed by equation (22). [26]

$$\Gamma = \frac{Z_1 - Z_0}{Z_1 + Z_0} \tag{21}$$

$$T = 1 + \Gamma = \frac{2 \cdot Z_1}{Z_1 + Z_0} \tag{22}$$

The commissioning of the FC included determination of the signal properties forced by the new geometry and the results are subject to discussion later in this chapter. As outlined earlier, the change to the transverse size of the beam stopper did not affect the dimensions of the entrance to the beam stopper cavity and the geometrical suppression of the ion-induced electron emission was not affected. Extensive discussion regarding this topic is presented in the following section.

3.3 Ion-induced electron emission and proton interactions

Ion-induced electron emission from the target surface of the charge collector may contribute significantly to the overall charge collection efficiency. Several different theories have been introduced over last few decades explaining the mechanisms of ion-induced electron yields, presenting various experimental results. [32][33][34] In general, the proton electronic stopping power comes from two interaction processes:

- Distant collisions that liberate large numbers of low-energy secondary electrons;
- Close collisions characterised by a large energy transfer to a small number of electrons that result in the kinetic energy of electrons being sufficiently high for

them to trigger further ionisation events in cascade processes and, with their kinetic energy being higher than the work function, allowing them to cross the surface barrier and escape.

Because of the above, two mechanism of electron emission are distinguished:

- *Potential emission*, γ_P;
- *Kinetic emission*, γ_K;

And ultimately both contribute to the total emission γ, equation (23).

$$\gamma = \gamma_P + \gamma_K \tag{23}$$

Here, γ is defined as the number of electrons emitted per an impinging primary particle. These are emitted into the half space in front of the irradiated target surface creating a backward emission. The majority of the emission curves reported in the literature are presented as a function of an angle with respect to the normal to the surface of particle incidence, where the particles hit the surface at a normal angle. The emission coefficient rises with the particle energy with a distinct threshold for the kinetic energy. The potential emission then becomes only a constant that diminishes further with the energy increase. The distribution of electrons with respect to the solid angle (Ω) has been shown to follow the dependence (24). [32]:

$$\frac{d\gamma}{d\Omega}(\vartheta) = \frac{d\gamma}{d\Omega}\Big|_{\gamma=0} \cdot \cos\vartheta \tag{24}$$

where :

ϑ - Angle of emission with respect to the normal of the surface.

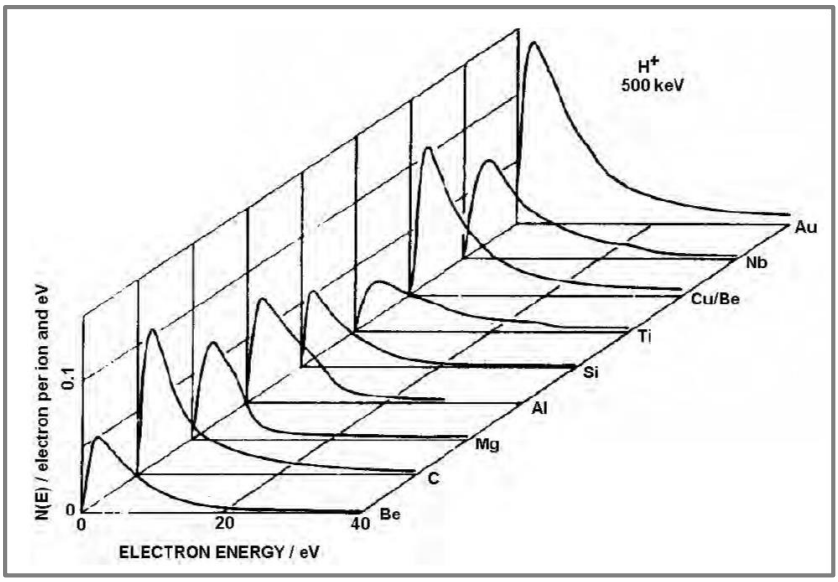

Figure 11: Ion-induced electron emission spectra for electron emission induced by protons of $\mathrm{E} = 500\ \mathrm{keV}$ impinging on various metal surfaces. [32]

The potential emission depends on the ionisation potential and the work function for electrons in the irradiated material. This type of emission is important for energies of up to 300 keV. Beyond this threshold kinetic emission is pronounced because of many other mechanisms, e.g. molecular electron capture. It has been shown that the kinetic electron emission is proportional to the electronic stopping power. [34] Electrons exited inside metal drift towards the surface in straight lines with the assumption that the excitation takes place in just a few first tens of Angstroms on entering the metal. Their distribution of emission is proportional to $\cos\vartheta$, as in the case of the low-energy potential emission in equation (24). [34]

In general, the election emission spectra in the low energy region have a peak at around 2-4 eV which falls down towards higher energies (figure 11). At the same, it is independent from proton energy, yet, it does show dependence on the material type because of the specific stopping power and surface barrier. For proton energies $\mathrm{E} > 250\ \mathrm{keV}$ there are two distinctive regions of electron emission:

- Low energy region for electron energies below $50\ \mathrm{eV}$ which remains impact-energy independent;
- High energy part, beyond the mentioned threshold, which manifests energy-dependence, explicitly, the number of electrons building the spectrum increases with the impact energy.

The low energy spectrum is believed to be caused by cascade processes of highly energetic, ionising δ-electrons. The high energy region, which may extend to hundreds of keV, is associated with both the direct kinetic energy transfer to electrons and further molecular processes. [32] The latter, associated with an electron loss by the projectile, may lead to electron emission at energies centred on the energy corresponding to the velocity of the impinging particle. The mechanism it triggered, when a proton picks-up an electron from the target material which in the next stage can be lost. Therefore, those two spectra are always superimposed of a discrete part originating from the electron loss close to or at the surface, corresponding to the impinging particle energy, and a continuous part created by the electrons liberated just below the surface, which degrade their energy during migration towards the surface. Production of δ-electrons is associated mainly with the proton kinetic energy losses in the inelastic collisions with orbiting electrons when slowing down in the medium. As previously mentioned, their kinetic energy gain is large enough so that they can cause further ionisation of other atoms and contribute to the increase of electron emission in the lower energy region.

A Kapton window, at the entrance to the vacuum vessel, also contributes to the electron emission seen by the collector. The electron energy spectrum can be estimated based on the Binary Encounter Peak connected with the maximum energy transfer of a fast heavy projectile of mass M_p and energy transferred E_p to a quasi – free electron of mass m_e. The energy of such electrons follows the dependence described by equation (25), [32]:

$$E_{BEA} \approx \frac{4m_e}{M_p} \cdot E_p \cdot \cos^2\theta \qquad (25)$$

where: θ - Scattering angle of the electron with respect to the direction of the incoming projectile.

The maximum electron energy is therefore obtained by electrons in the forward direction, following the projectile ($\theta = 0$). The energy depends on both the material type and thickness. These electrons, due to their low energy, can be easily supressed by a guarding ring, which repels them back toward the window. The effectiveness of the guarding ring is additionally supported at this point by the positive charge build-up in the dielectric window.

With regard to chapter 2, the average kinetic energy lost by a proton per unit distance is referred to as a *stopping power* [MeV/(g/cm^2)]. Small amounts of energy lost in collisions with

electrons lead to beam energy spread, which puts limit on the exact value of the penetration depth of protons. The alternative possible effect, outlined previously, is Multiple Coulomb Scattering as a result the small deflections in the proton path caused by electric potential of the target nuclei. The probability of proton experiencing a reversal of direction is small and, additionally, decreases with proton energy. [35] In unison, the range of penetration can be defined. [35]

For proton energies above 1 MeV the contribution to the energy transfer in elastic nuclear collisions is less than 0.1 % compared to the inelastic interactions. Elastic proton collisions with atomic nuclei play an important role for impact energies below $20\ \mathrm{keV}$ [34] and are negligible for the investigated $60\ \mathrm{MeV}$ beam at CCC. Abrupt energy loss in non-elastic nuclear reactions becomes significant for impact energies above $100\ \mathrm{MeV}$. As a result, they were not included in the modelling of the beam stopper described in the following section.

3.4 Modelling of the FC design

3.4.1 Geometry considerations

Modelling of the FC was performed to minimise the signal losses induced by the proton beam terminated beneath the target surface of the beam stopper (figure 12). Various phenomena described in the previous section give rise to a fluence of ion-induced particles and were modelled using the Monte-Carlo method. The simulations comprised of investigations of different materials and geometries of the target surface beam collector. The estimators of fluence (or current through a given surface) for both primary and secondary particles were used in FLUKA multi – particle transport code [36]. In general, particle transport supported by the program was possible for energies above $1\ \mathrm{keV}$. The ion-induced electron emission falling below that threshold had not been included and, therefore, was addressed as literature studies presented in the previous section and relied on a number of publications in [37] [38] [39] and [40].

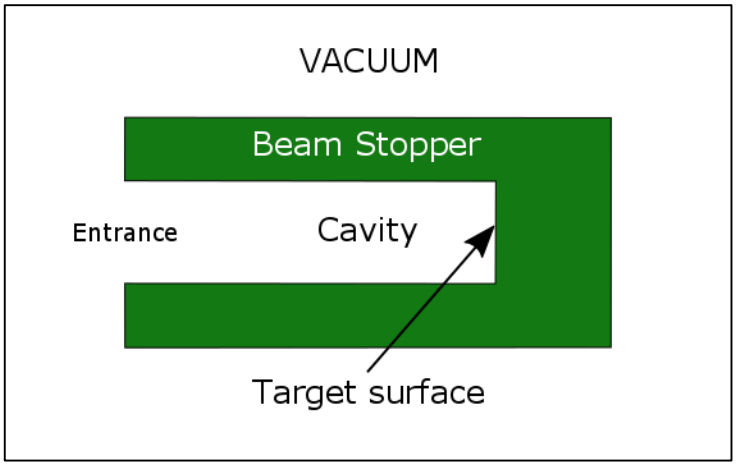

Figure 12: A model of the FC built in FLUKA. The boundary crossing estimators were set on all surfaces of the beam topper. The charge losses because of un-supressed fluence of both proton-induced emission of electrons or back-scattered protons were assessed by a boundary crossing estimator located at the face of the beam topper (left) covering the area of the entrance to the cavity.

The signal induced by the charge collection in the bulk of the beam stopper is additionally influenced by fluence of different particle species across two surfaces of interest. These, in regard to the final design of the FC (figure 21) and the model built in FLUKA (figure 12), can be defined as:

- The physical target surface inside the collector cavity accountable for emission of particles;
- An imaginary surface at the entrance to the cavity of the charge collector through which the unsuppressed particles escape to the vacuum.

There are three current components that give rise to either positive or negative contribution to the measured charge value in a following way:

- Backscattered protons give *negative* contribution,
- Ion-induced electrons emitted from the surface of the collector give positive contribution that increases the recorded signal;
- Ion-induced electrons ejected from the surface of the Kapton window reaching the collector give negative contribution to the signal.

The fluence of electrons in both the second and third case were supressed by different means depending on their energy. The depth of the cavity of the beam stopper was used to minimize the losses of electrons for energies above $1\ \mathrm{keV}$ whilst a guarding ring interacted with

the part of the spectrum falling below that threshold. The ring was fitted at the entrance to the FC with a circular opening of the diameter equal to the FC cavity entrance, $\Phi = 4.0\,\mathrm{cm}$, preventing any interception of the proton beam. A negative DC bias potential was applied to build an electric barrier of the minimum value $\mathrm{U} = -500\,\mathrm{V}$ on the central axis of the beam stopper.

With the aim of finding the bias potential, which would satisfy the above requirements, simulations were performed in Computer Simulation Technology Suite (CST). [41] For a voltage of $\mathrm{U} = -1000\,\mathrm{V}$ applied to the ring, the potential barrier on the central axis was found to be $\mathrm{U_{centre}} = -700\,\mathrm{V}$. The obtained results of the modelling are illustrated in figure 13.

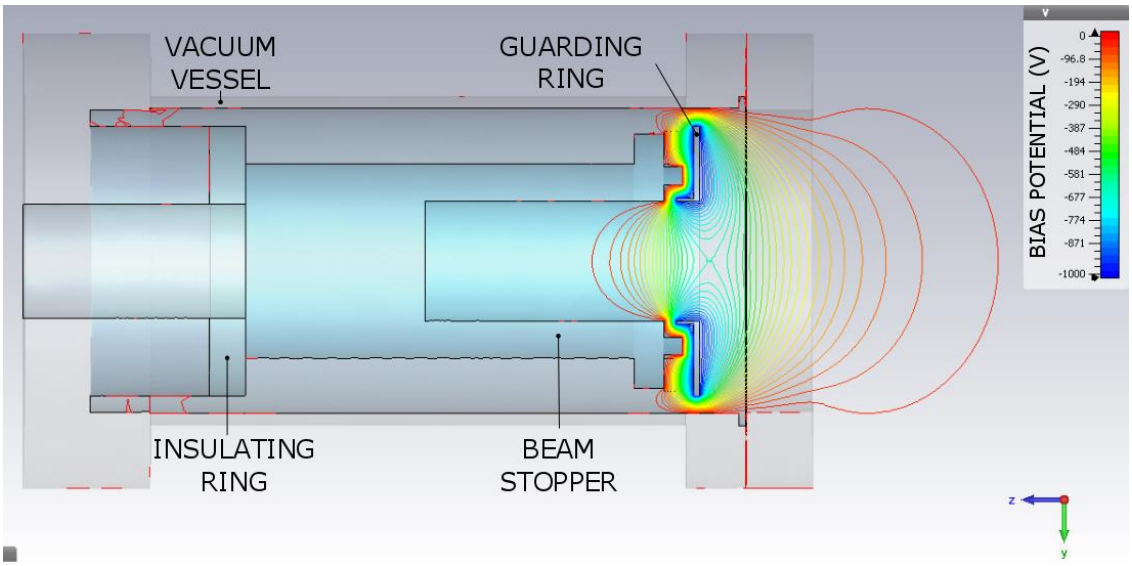

Figure 13: Distribution of the potential around the guarding ring for the bias potential U_{bias} = 1000 V.

The distributions of backscattered protons and electrons emitted for the target surface were tackled in simulations preformed in FULKA. The settings of transport of both charged practices and photons can be examined in table 3. Here, a set of models was run to find both the optimum geometry and suitable material that would provide a low magnitude of signal losses. A number of boundary crossing estimators, embedded in the code, were set on the surfaces of the beam stopper and were corresponding to the stated target surface of the beam stopper and the entrance to the cavity.

The first boundary was used to assess the fluence of the proton-induced emission of particles into the half space in front of the surface. The angular bins were set every 1.047 steradians, which corresponds to the equivalent intervals in the polar angle of $15°$.

The same set of estimator properties was used to establish binning for the second surface to assess the amount of escaping charge. The shape of the target surface was additionally varied between *flat*, *conical* and *spherical* to find the lowest forward emission.

The series of figures 14 to 20 demonstrate the charge fluence carried by both protons and electrons estimated in FLUKA for the nominal proton intensity $\mathrm{I} = 1.6\ \mathrm{nA}$. For each type of particle the first two plots illustrate the emission spectrum from a flat target surface made of aluminium whilst the following figures depict spectra of particles escaping from the beam stopper to the vacuum through the cavity entrance. Both of them were calculated as double differential charge fluence $\mathrm{d}^2\mathrm{f}/\mathrm{dE}\ \mathrm{d}\Omega$ with respect to energy and solid angle. For the clarity of interpretation, the solid angle was expressed in equivalent polar angle values with respect to the normal of the surface in the direction opposite to the beam direction. Integration of each of the curves produced the predicted total charge carried away by particles for each of the angular bins. At the same time the cavity attenuation coefficient k and measurement error were determined to support the decision on the final beam stopper design.

The predictions of proton-induced electron spectra for an aluminium target and the beam intensity $\mathrm{I} = 1.6\ \mathrm{nA}$ are depicted in figures 14 and 15. In each case the spectra emitted from the target surface are continuous with pronounced peak that falls below the maximum energy transfer from protons to an orbiting electron, where for the kinetic energy of protons $\mathrm{E_{kin}} = 60\ \mathrm{MeV}$ the value evaluated with equation (3) is $\mathrm{E_{max}} \approx 135.08\ \mathrm{keV}$. The angular intensity distribution falls down with larger angles of emission from the target surface as the electron path length to the surface becomes longer. The total charge carried away by electrons, both emitted from the beam stopper and escaping to the vacuum through the entrance to the cavity, are obtained by integration. For the three considered cavity termination types the largest electron emission takes place for the conical shape and was assessed to be at the order of 5 % of the nominal beam current intensity. The lowest relative emission was found for the flat geometry. The depth of the cavity supported the recollection of electrons. The flat and spherical shapes proved that only 0.15 % of the initial charge carried by the beam could escape to vacuum. For the conical geometry of the target surface, the losses were higher by 0.06 %. The detailed quantitative description of the electron emission studies and their geometrical suppression can be examined in table 4.

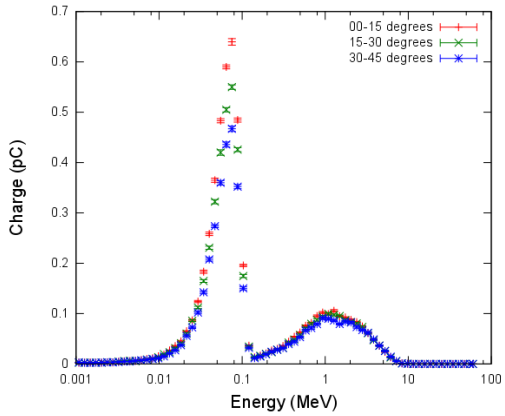

Figure 14: Charge distribution of proton-induced emission of electrons versus energy from the flat impact surface of the beam stopper for a proton beam intensity $I_p = 1.6$ nA and angles 0° and 45°.

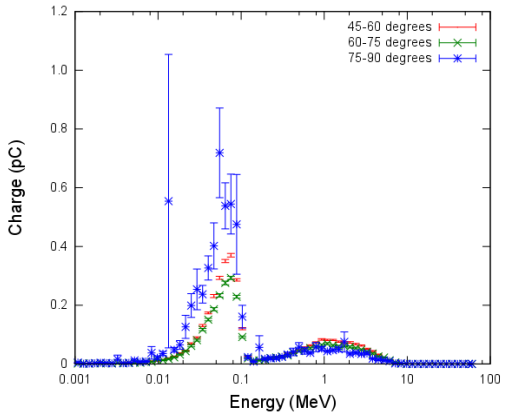

Figure 15: Charge distribution of proton-induced emission of electrons versus energy from the flat impact surface of the beam stopper for a proton beam intensity $I_p = 1.6$ nA and angles 45° and 90°.

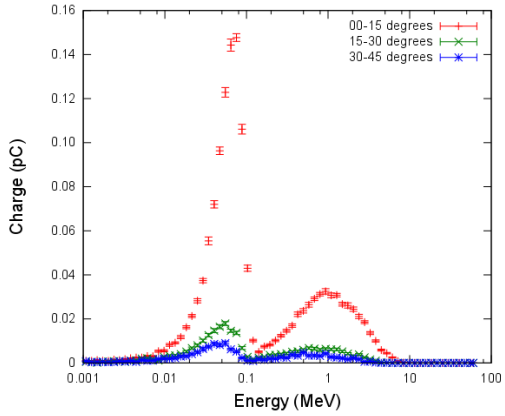

Figure 16: Charge distribution of electrons unsuppressed by the geometry of the beam stopper cavity and leaving to the vacuum versus energy for a proton beam intensity $I_p = 1.6$ nA and angles 0° and 45°.

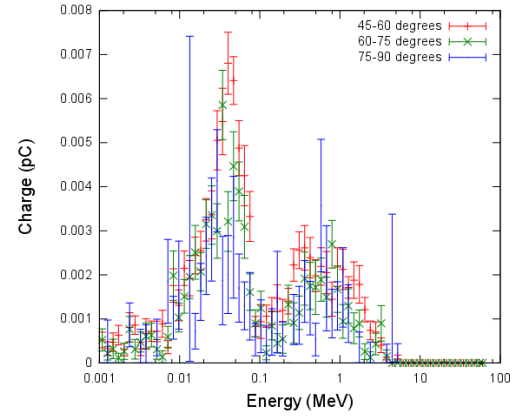

Figure 17. Charge distribution of electrons unsuppressed by the geometry of the beam stopper cavity and leaving to the vacuum versus energy for a proton beam intensity $I_p = 1.6$ nA and angles 45° and 90°.

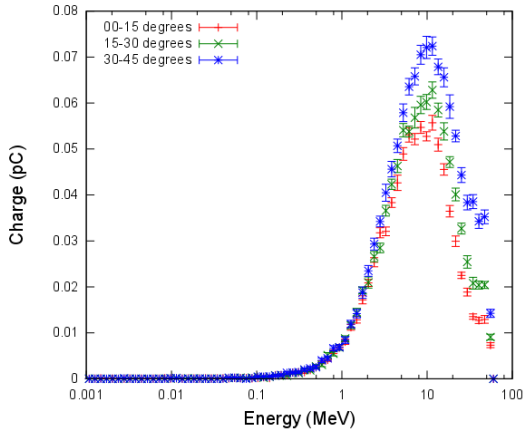

Figure 18: Charge distribution versus energy and angle of emission for protons backscattered from the flat impact surface of the beam stopper for an initial beam intensity $I_p = 1.6\ nA$ and the angle interval between $0°$ and $45°$.

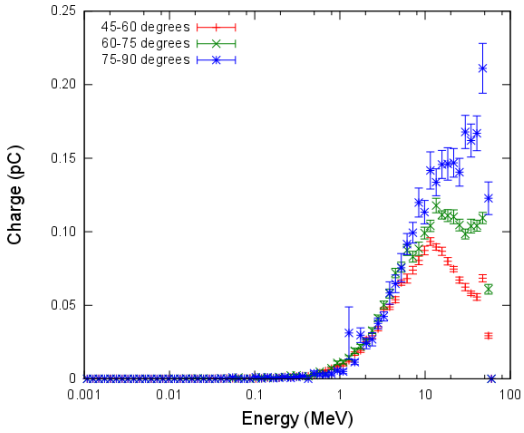

Figure 19: Charge distribution versus energy and angle of emission for protons backscattered from the flat impact surface of the beam stopper for an initial beam intensity $I_p = 1.6\ nA$ and the angle interval between $0°$ and $45°$.

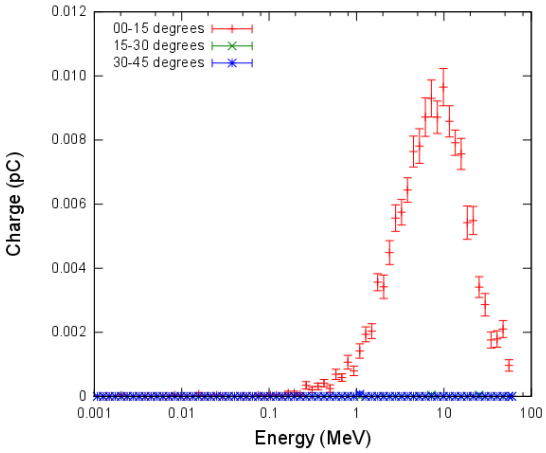

Figure 20: Charge distribution of protons versus energy and angle for the fraction of protons unsuppressed by the geometry of the beam stopper cavity and leaving to the vacuum for a proton beam intensity $I_p = 1.6\ nA$ and angles $0°$ and $45°$.

The number of backscattered protons at full energy is small due to the low probability of proton elastic scattering on the target nuclei with the reversal of their path (figures 18 and 19). The energy spectrum reaches maximum around $E = 10\ MeV$ at an angle $\alpha = 0°$ with respect to the normal of the surface with a gradual shift towards higher energies with increasing α, when a larger number of protons with kinetic energies around $60MeV$ experience Rutherford scattering. The majority of protons crossing the target surface are recollected and terminated in the side walls of the cavity. The attenuation coefficient k is much

larger than for electrons and reaches $k = 100.8$ for the conical design of the cavity termination. A more detailed quantitative description of the geometrical attenuation properties of the charge collector can be examined in table 5. In general, the charge collection process introduces an insignificant error due to escaping protons since they constitute only about 0.01% of the beam intensity $I = 5.0\ nA$ and the value of losses is independent from the geometry of the cavity termination.

As a result of the numerical predictions, the error introduced to the beam current measurement with the FC did not exceed 0.16 % of the nominal value and, for this reason, falls into the noise level of the readout electronics. The differences coming from the assessed variants of the cavity termination were small with the advance of the flat geometry over the others, table 4. Therefore, the simplest and both most cost- and machining-effective flat geometry was chosen for the final design.

Table 3: Summary of settings for transport and physical phenomena applied to simulations in FLUKA to assess the extent of secondary particles emission from the surface of the FC.

Type of particles in the beam	p^+	
Particle kinetic energy [MeV]	60	
Beam shape	Annular	
Number of particles	$1.0 \cdot 10^7$	
Transport options		
Electromagnetic interactions	Electrons / positrons	
	Kinetic energy threshold [keV]	1.0
	Phenomena	Bremsstrahlung, Pair production, Photoelectric effect
	Electromagnetic radiation	
	Transport energy threshold [keV]	0.1
Proton transport threshold [keV]	1.0	
Electron transport threshold [keV]	1.0	
δ-electrons production [keV]	100	
Multiple Coulomb Scattering	Enabled	
Neutron transport and self-shielding	Enabled	

Table 4: Ion-induced emission of electrons from the three geometrical types of the beam stopper impact surface and external surface for aluminium and efficiency of the suppression of the emitted electrons by the geometry of the Faraday Cup cavity.

Beam current, I_0 (nA)	5.00		5.00		5.00	
Geometry	Flat		Spherical ($r = 2.0\ cm$)		Conical ($\alpha = 45°$)	
Surface	I_e (nA) Rel I_e	$u(I_e)$ (nA)	I_e (nA) Rel I_e	$u(I_e)$ (nA)	I_e (nA) Rel I_e	$u(I_e)$ (nA)
Target	$8.90 \cdot 10^{-2}$ (1.79%)	$1.96 \cdot 10^{-3}$	$8.76 \cdot 10^{-2}$ (2.88 %)	$4.20 \cdot 10^{-3}$	$1.71 \cdot 10^{-1}$ (5.63 %)	$4.11 \cdot 10^{-3}$
External	$3.84 \cdot 10^{-3}$ (0.13 %)	$2.12 \cdot 10^{-5}$	$3.51 \cdot 10^{-3}$ (0.12 %)	$1.73 \cdot 10^{-5}$	$3.48 \cdot 10^{-3}$ (0.11 %)	$2.43 \cdot 10^{-5}$
Cavity opening	$3.90 \cdot 10^{-3}$ (0.13 %)	$2.17 \cdot 10^{-5}$	$4.73 \cdot 10^{-3}$ (0.16% %)	$2.23 \cdot 10^{-5}$	$7.07 \cdot 10^{-3}$ (0.23 %)	$2.73 \cdot 10^{-5}$
Absolute losses	$7.74 \cdot 10^{-3}$ (0.15 %)	$3.03 \cdot 10^{-5}$	$8.24 \cdot 10^{-3}$ (0.16 %)	$2.82 \cdot 10^{-5}$	$1.05 \cdot 10^{-3}$ (0.21 %)	$3.65 \cdot 10^{-5}$
Attenuation factor	11.5		10.6		16.2	

Table 5: Intensities of protons emitted from the three geometrical types of the beam stopper impact surface and efficiencies of the suppression of the emitted protons by the geometry of the Faraday Cup cavity.

Beam current, I_0 (nA)	5.00		5.00		5.00	
Geometry	Flat		Spherical ($r = 2.0\ cm$)		Conical ($\alpha = 45°$)	
Surface	I_p (nA) Rel I_p	$u(I_p)$ (nA)	I_p (nA) Rel I_p	$u(I_p)$ (nA)	I_p (nA) Rel I_p	$u(I_p)$ (nA)
Target	$2.79 \cdot 10^{-2}$ (0.56 %)	$1.68 \cdot 10^{-4}$	$2.47 \cdot 10^{-2}$ (0.55 %)	$2.47 \cdot 10^{-4}$	$5.64 \cdot 10^{-2}$ (1.13 %)	$9.13 \cdot 10^{-4}$
Absolute Losses	$4.37 \cdot 10^{-4}$ (0.01 %)	$6.67 \cdot 10^{-6}$	$4.51 \cdot 10^{-4}$ (0.01 %)	$6.99 \cdot 10^{-6}$	$5.60 \cdot 10^{-4}$ (0.01 %)	$8.04 \cdot 10^{-6}$
Attenuation factor	63.8		60.7		100.8	

The depth of the side walls of the beam stopper was also sufficient to effectively recollect the emitted particles by their termination and, this way, maintaining the charge equilibrium in the collector.

3.4.2 Material considerations

Signal losses, as a function of the charge collector material type were evaluated for copper, aluminium and graphite. This choice was based on the most common materials reported in literature for various FC designs. The flat target surface chosen for the final design was used in numerical predictions with the fluence estimators set in the same way as for the geometrical studies. The evaluated charge losses down to the proton-induced electrons emission can be examined in table 6. Among the studied materials, graphite showed the lowest proton-induced electron emission contributing to the beam intensity measurement with a relative error of 0.34 %. The geometry of the beam stopper decreased the error by recollection of electrons to 0.07 %. Although, graphite demonstrated the best predicted characteristics, aluminium was used as the final design material. The choice was a compromise between the measurement errors, reduced weight of the charge collector compared to copper and the mechanical properties for copper are better than for fragile graphite. The weight was a crucial factor in terms of pressure posed by the beam stopper on the PEEK mounting bolts and Teflon disc insulating it from the grounded vacuum vessel.

Table 6: Summary of the predicted beam intensity errors introduced by the proton-induced electron emission for different types of the beam stopper material and flat cavity termination related to nominal beam intensity $I = 5.0\ nA$.

Material	Emission			Losses		
	I_e [nA]	Rel. I_e (%)	$\sigma(I_e)$ [nA]	I_l [nA]	Rel. I_l (%)	$\sigma(I_l)$ [nA]
Copper	$3.31 \cdot 10^{-1}$	6.62	$1.10 \cdot 10^{-1}$	$1.00 \cdot 10^{-2}$	0.20	$4.96 \cdot 10^{-5}$
Aluminium	$8.90 \cdot 10^{-2}$	1.79	$1.96 \cdot 10^{-3}$	$7.74 \cdot 10^{-3}$	0.15	$3.03 \cdot 10^{-5}$
Graphite	$5.85 \cdot 10^{-3}$	0.34	$8.80 \cdot 10^{-4}$	$3.38 \cdot 10^{-3}$	0.07	$2.30 \cdot 10^{-4}$

3.5 Mechanical design

The final mechanical design of the FC is presented in figure 21. The vacuum vessel was a standard stainless steel DN100CF 4-way reducer cross. [42] The beam stopper was machined in an aluminium alloy consisting of 95 % of aluminium (99.9 % purity) and 5 % magnesium to give it better mechanical properties as opposed to pure aluminium.

The beam stopper was chosen to be a hollow cylinder with an outer diameter of $\phi_{\mathrm{FC}} = 63.0\ \mathrm{mm}$, an inner diameter of the cavity $\phi_{\mathrm{cavity}} = 40.0\ \mathrm{mm}$ and depth $\mathrm{d} = 80.0\ \mathrm{mm}$. The cylinder was sat on a Teflon insulating ring and was fixed with four PEEK insulating screws. The whole assembly was fastened to the aluminium back ring bolted directly with four long stainless steel screws to a DN100CF-to-DN40CF reducer flange. Both Teflon and aluminium rings have a centrally bored hole, with a diameter of $\phi = 38.1\ \mathrm{mm}$, to accommodate a $50\ \Omega$ coaxial BNC connector, which fit onto a readout pin on the charge collector. The signal was transferred along an Ultra High Vacuum (UHV) compatible shielded coaxial cable terminated with an SMA male connector. A double sided SMA coaxial feed-through transferred the signal outside the vessel. The impedance of the feedthrough was matched with the coaxial cables attached on either side, meaning it had an impedance of $Z = 50\ \Omega$.

A wide copper guarding ring was installed at the entrance to the cavity and was fixed to the beam collector with another Teflon ring and tightened with four PEEK screws. This arrangement provided the concentric alignment of the guarding ring with the beam stopper and was determined by the location of the mounting holes. The bias high voltage was applied by a grounded and shielded coaxial Kapton cable, terminated with a custom BNC push-on connector on the ring side and a push-on connector on the BNC feed-trough end. The BERTAN 205B-010R power supply was used as a source of a bias voltage, characterised by the specified noise level of 10mV in ripple. [43]

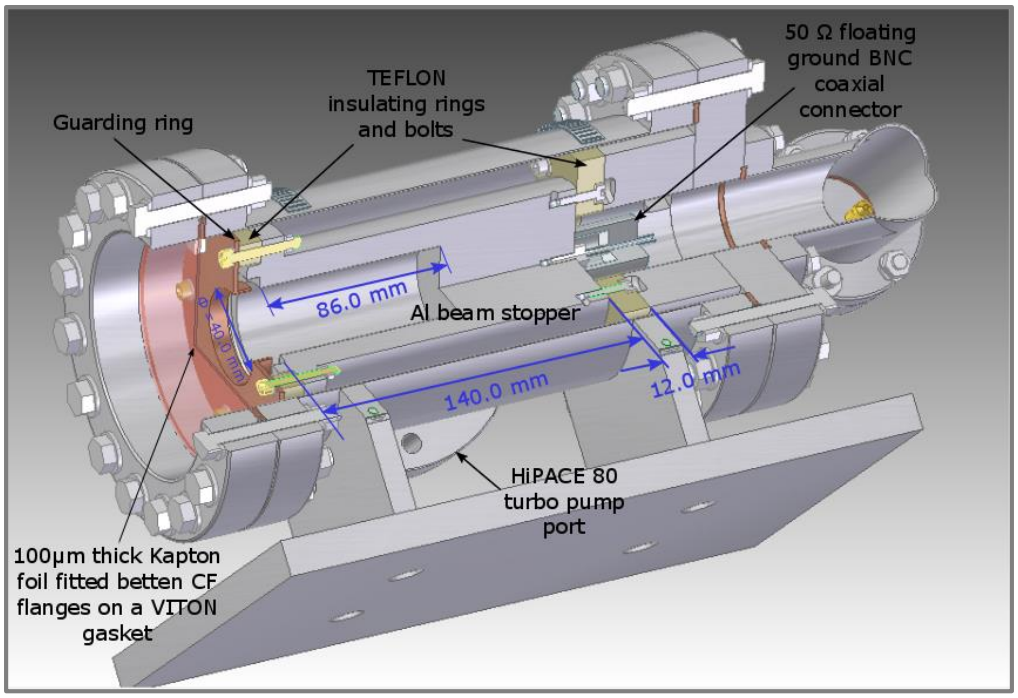

Figure 21: A cross-section of the technical drawing of the FC created in Solid Edge. [44]

The FC was surrounded by vacuum produced by a Pfeiffer HiPace80 turbo pump [45] bringing the average pressure down to $p = 1.2 \cdot 10^{-5}$ mbar. A $100\mu m$ thick piece of Kapton foil was spread evenly on a Viton gasket and clamped between CF flanges forming a vacuum window. The first tests of the window with a backing pump at a pressure $p = 2.2 \cdot 10^{-2}$ mbar verified that the applied solution was sufficient to build a vacuum-tight connection capable to withstand the achieved pressure difference (figure 22).

The FC assembly was mounted in front of the treatment nozzle on a dedicated stand made of light aluminium profiles. The alignment of the FC with the treatment isocentre was assured by a dedicated aluminium boss coupling the FC and the nozzle. The shape of the boss allowed for sub-millimetre accuracy of positioning in both the vertical and horizontal direction. The wider back part was fitted tightly inside the CF flange whereas a bore in the centre could accommodate the treatment nozzle (figure 22).

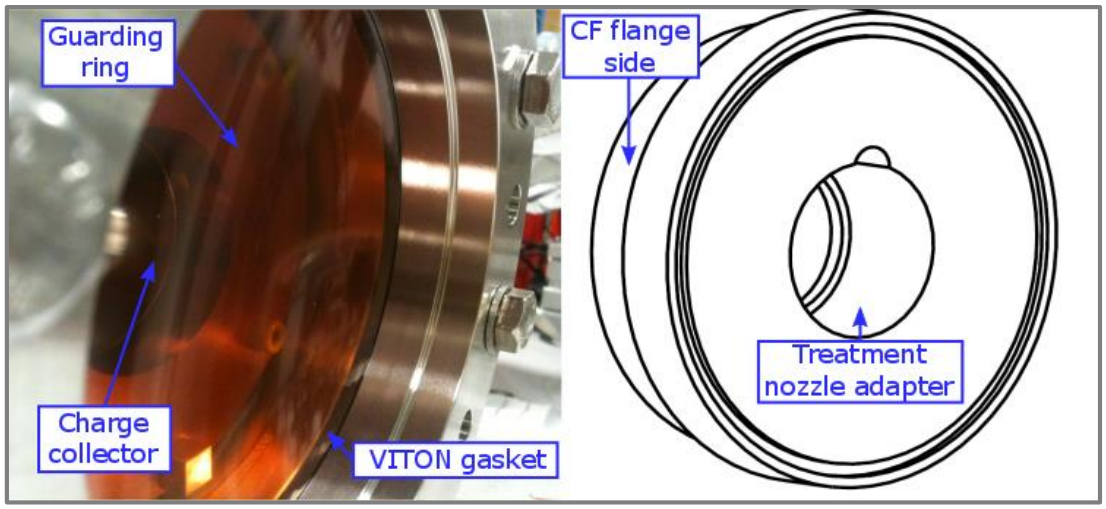

Figure 22: A picture of the Kapton window mounting with and a technical drawing of the alignment boss.

3.6 Faraday Cup readout and time domain response tests

The beam current measurements which, in the future, are to be taken in an attempt to resolve the timing of bunches at CCC require low noise electronic components in the readout chain. With regard to the nominal beam parameters (table 1), the average current of the beam is $\mathrm{I} \approx 5\ \mathrm{nA}$ and the peak current of a single bunch is $\mathrm{I_{peak}} = 0.139\ \mu\mathrm{A}$. Therefore, both the electronic readout and the design of the FC, including the set-up assembly, had to be tackled with attention to exclude any excessive sources of noise, except for those originating from the theoretical limits associated with the structure of matter. [46] Generally, the noise sources can be divided into several types depending on their origin:

- electromagnetic or electrostatic interference
- ionisation interference
- secondary particles emission
- leakage currents
- sputtering
- tribo-electric noise
- stereophonic noise
- offset currents (input offset) current
- thermal noise
- shot noise

Various types of noise appear at different places of the set-up and, therefore, the design has to consist of matched elements and had to be thought of globally to mitigate the effects of their existence. Electromagnetic interference is the most common cause of noise introduced to measured values coming from e.g. RF sources at accelerators, guarding ring, electrical installation of the building, fluorescent lamps etc. A remedy to the above includes introducing a metal shielding around the sensitive elements, similar to a coaxial cable, which is coupled to low impedance. Thus, any DC or AC noise current coming from an external source is kept away from the signal cable and flows only in the shield.

This cannot, however, happen when a capacitive coupling between the guarding ring and charge collector is considered. The current induced by ripple in the bias voltage V, which happens in a time interval t, leads to changes in the capacitance of the system (C) and is expressed by equation (26). [48]

$$\frac{dQ}{dt} = C \cdot \frac{dV}{dt} + V \cdot \frac{dC}{dt} \tag{26}$$

The most effective remedy here is the application of a low-ripple power supply and, preferably, a time constant between the two that would result in a low cut-off frequency.

Ionisation of remaining gas inside the vessel, caused by the irradiation with protons, produces electron-ion pairs. The bias voltage applied to the guarding ring separates these charges and electrons are repelled towards the charge collector decreasing the actual value of beam current reading. This effect is reduced by operation of the charge collector in vacuum with continuous pumping down of the system. In addition, geometrical suppression of particles has an effect on the measured pulse shape because of the time between the emission of electrons from the target surface and their re-collection by the beam stopper manifesting in a broadening of the measured peak as a response to a single bunch.

Any contamination of the surface of the insulator, between the metal stopper and the ground vessel, can lead to leakage currents. Here, not only dust or chemicals are considered but also water or sputtered metal from the beam stopper. That was eliminated by thorough cleaning of the elements to UHV standards, which was sufficient to eliminate chemical contamination. Sputtering happens when atoms of metal are removed from the surface due to ion bombardment and are deposited on other surfaces, where they can create short paths to the

ground. This effect can be only controlled by careful design of the device in order to avoid any deposition on critical insulating elements.

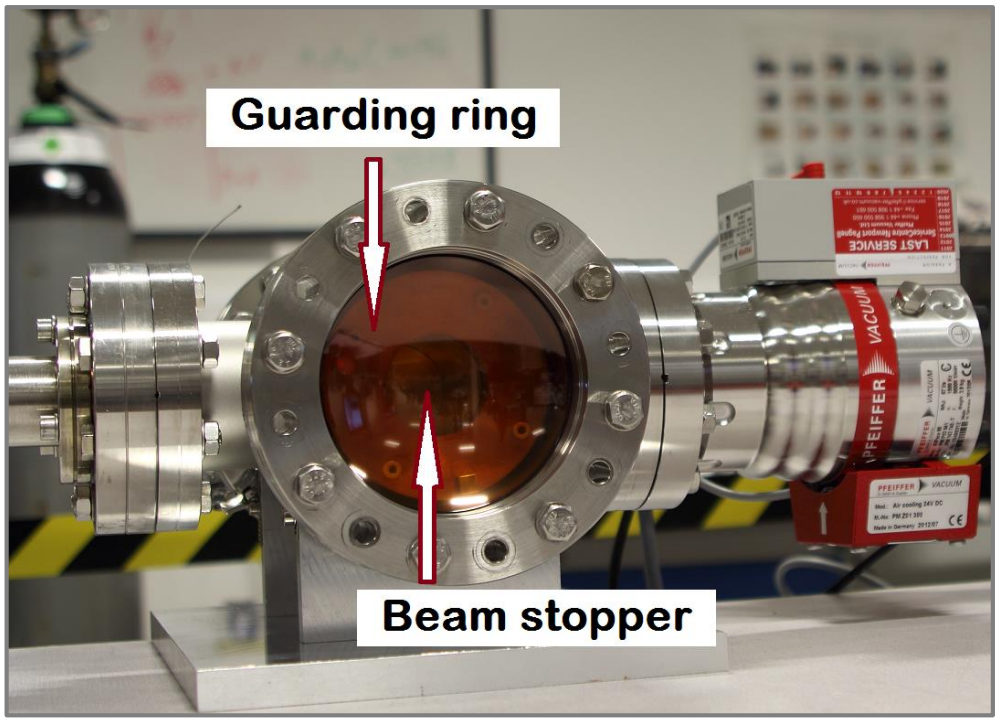

Figure 23: Photograph of the assembled FC with the turbo pump fitted on one of the ports.

The tribo-electric and stereophonic noise can, to some degree, be grouped together. They are caused my mechanical stress or vibrations of the readout elements, e.g. cables. In the first case additional current flow is induced between different points of the conductor when friction between the conductor and insulator takes place and may lead to local charging of the insulator. Any obstructions or movement of cables should for that reason be avoided, like originating from the mechanical elements of the set up or vacuum pumps. Low noise cables were applied in the readout chain of the FC, where the low friction coating was introduced between above layers. Furthermore, the stereophonic noise can also create local temperature gradients, which may increase the thermal noise.

Offset current or input offset current are directly linked with the amplifiers and their non-zero readout, when both input and output are open. This normally settles to the values specified for the device when sufficient warm-up time is allowed.

Thermal noise is directly connected with the structure of matter and sets theoretical limits on low level measurements. [46] It is associated with the thermal movement of electrons. The Johnson noise of resistance $\mathrm{R}\ [\Omega]$, in terms of both voltage and the current RMS (root mean square value), depends directly on the temperature $\mathrm{T}\ [\mathrm{K}]$ and the bandwidth of measurement $\mathrm{B}\ [\mathrm{Hz}]$:

$$E = \sqrt{4 \cdot k_B \cdot T \cdot R \cdot B} \tag{27}$$

$$I = \frac{\sqrt{4 \cdot k_B \cdot T \cdot B}}{R} \tag{28}$$

That last type of noise influencing measurements is Schotty noise (also called shot noise), which cannot be compensated for. The nature of it lies in quantisation of charges of an average current value $\bar{\mathrm{I}}$ and strongly depends on the bandwidth of the measurement B:

$$I_{shot} = \sqrt{4 \cdot e \cdot \bar{I} \cdot B} \tag{29}$$

The low noise charge or current amplification utilises advantageous properties of trans-impedance amplifiers. In such a case the most commonly set-up consists of an inverting operational amplifier characterised by a very high gain and input impedance, and very low output impedance coupled with a feedback resistor (figure 24). The gain of a trans-impedance amplifier is described by equation (30).

$$V_{out} = I_{in} \cdot \frac{-k}{k+1} \cdot \frac{R_F}{1 + j\omega C_T \cdot \frac{R_F}{k+1}} \tag{30}$$

Where the input capacitance C_T expressed by equation (31) has got a few constituents:

- Capacitance of the Faraday Cup, C;
- Capacitance of the elements building the amplifier, $\mathrm{C_{in}}$;
- Stray capacitance of all the other elements of the circuit.

$$C_T = C_{FC} + C_{in} + C_{stray} \tag{31}$$

The bandwidth of the amplifier is a result function of the source capacitance and ante feedback capacitance, together with the gain bandwidth of the actual amplifier.

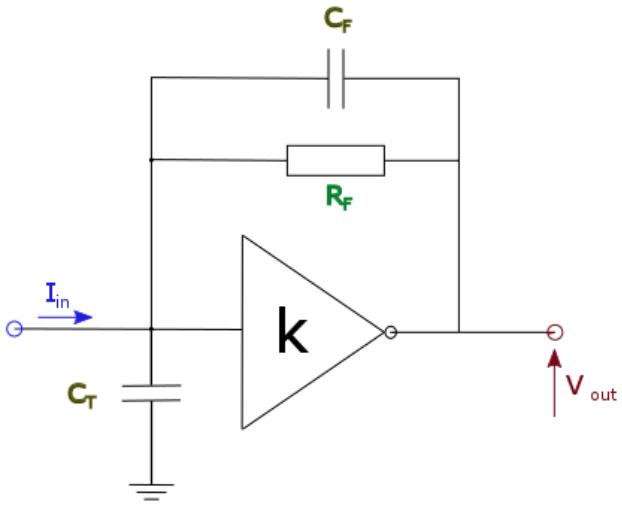

Figure 24: Layout of the trans-impedance amplifier with wide bandwidth. [47]

This basic concept applies to any trans-impedance amplification in readout of fast changing signals. In the discussed application of the FC a dedicated readout system resolving single bunches had not been devised owing to the fact that readout of the VELO detector was not envisaged to be synchronised with the exact bunch arrival time as it will be explained in the following chapters. Nevertheless, the design of a wide bandwidth amplifier for the future method development will have to be able to support amplification of the peak currents described in chapter 6. The average treatment beam current measured there was $\mathrm{I} \approx 0.112\ \mathrm{nA}$ and was equivalent to $\mathrm{N} = 1.17 \cdot 10^{2}$ protons carried in one bunch. The estimated peak current of the bunch of the length $\mathrm{t} = 1.35 \cdot 10^{-9}$ s is:

$$I_{peak} = \frac{N \cdot e}{t} = \frac{2.22 \cdot 10^{3} \cdot 1.602 \cdot 10^{-19}\ C}{1.35 \cdot 10^{-9}\ s} = 2.22\ nA \qquad (32)$$

The time response of the FC was tested using a Keysight 8110A pulse generator, which sourced an input signal fed directly onto the beam stopper. The connection was established on the cavity side of the charge collector, where the core of the coaxial cable was mounted. The screening braid was fed back to the housing vessel and shared the grounding with the readout system (figure 26). The amplitude of the input signal was $\mathrm{U} = 1.96\mathrm{V}$ and the frequency of the signal was varying in the range between $1\ \mathrm{MHz}$ to $32\ \mathrm{MHz}$. The leading and training edges of the pulse were equal and characterised by the rise time $\mathrm{t_r} = 2.0\ \mathrm{ns}$, where the pulse width at half maximum (FWHM) was $\mathrm{t_{FWHM}} = 3.1\mathrm{ns}$. The signal transfer lines were made of 50Ω

coaxial cables. Ultimately, the readout of the signal from the Faraday Cup was transferred through a concentric cable to a Yokogawa DL9550L oscilloscope (figure 25).

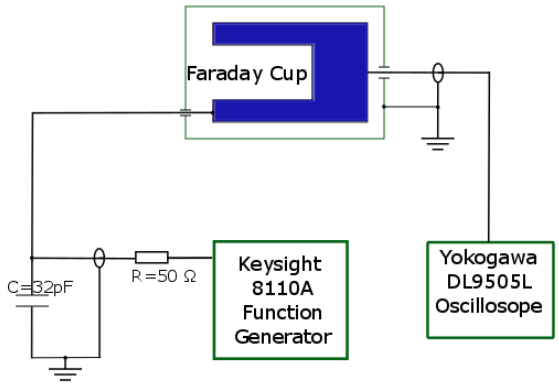

Figure 25: Diagram for the FC test set-up in the time and frequency domain.

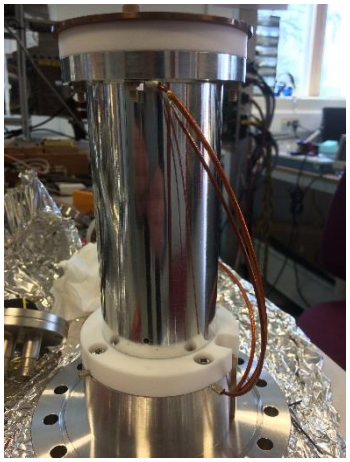

Figure 26: Wiring of the FC for the signal testing.

The impedance mismatch of the FC because of the decreased geometry of the device lead to reflections at the points of connection of the input cable and the readout side as a result of no impedance compensation applied between either end of the FC and the coaxial cables. In relation to equations (21) and (22) an expected amplitude of the signal arriving at the oscilloscope can be calculated. The reflection coefficients for both impedance mismatch points were obtained using the assumed system impedance $\mathrm{Z_{FC}} = 25.0\ \Omega$, as the actual value would have to be either measured or simulated. The estimated amplitude was found to be $\mathrm{U} = 0.87\ \mathrm{V}$ and is in agreement within 5% accuracy with the measured value for a frequency of $\mathrm{f} = 1.0\ \mathrm{MHz}$ (figure 28). The oscillations following the main peak pile-up with next arriving signal with an increase of frequency. An intermediate stage for the frequency $\mathrm{f} = 15.0\ \mathrm{MHz}$ is illustrated in figure 29 and was included in assessment of the performance of the amplitude value versus frequency to find the relative error with respect to the value measured for a frequency of $1\ \mathrm{MHz}$. The maximum signal pile takes place for frequencies around $20\ \mathrm{MHz}$, where the error in the main peak reaches $15\ \%$, the mismatch drops down to the local minimum of $-2.5\ \%$ for the cyclotron frequency (figures 31 and 32) and immediately rises up. Despite the demonstrated mismatch, the designed Faraday Cup allows single bunches arriving from the accelerator to be resolved. The usability of the device, however, depends on the time constant of the implemented readout circuit. Slow integrating devices, such as picoammeters, are suitable

for measuring average beam current from the proposed FC design as, regardless of the observed reflections, all the charge is ultimately collected by the readout circuit. Precise impedance matching must be applied for low time constant characterising the readout, such as trans-impedance amplifier, to exclude any distortions to the signal and provide a trigger for VELO detector. In practice, the impedance of the transmission line $\mathrm{Z_L}$ seen by the FC, treated as another transmission line with characteristic impedance $\mathrm{Z_{FC}}$, can be decreased by applying a shunt resistance R in parallel (figure 27). The appropriate value of resistance can be obtained following equation (33) and shall be $\mathrm{R} = 50\Omega$ for the impedance of the FC of $\mathrm{Z_{FC}} = 25\ \Omega$ fitted at the readout connection.

$$R = \frac{Z_{FC} \cdot Z_L}{Z_L - Z_{FC}} \tag{33}$$

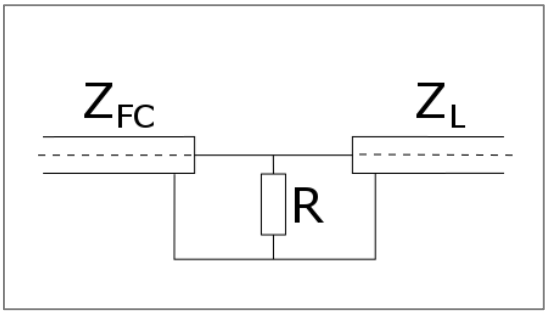

Figure 27: Impedance matching decreasing the value of the impedance of the transmission line L seen by the Faraday Cup.

To compensate for the impedance mismatch between the source transmission line and the FC, the impedance of the FC seen by the transfer line must be increased. A resistor of $\mathrm{R} = 25\ \Omega$ determined according to equation (34) shall be fitted in series with the transfer line and the FC.

$$R = Z_L - Z_{FC} \tag{34}$$

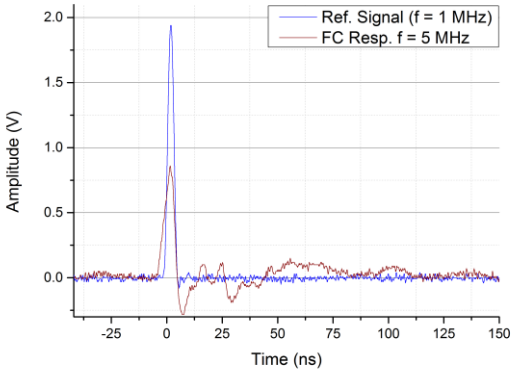

Figure 28: Response of the FC for the frequency of the input impulse $f = 1$ MHz.

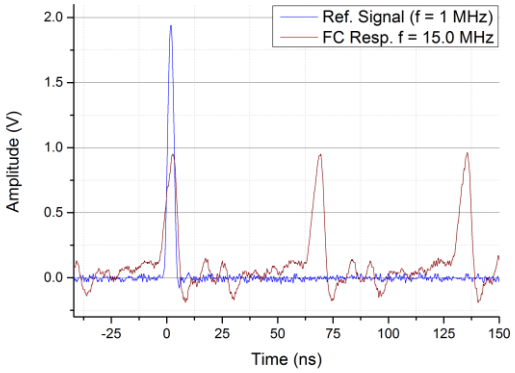

Figure 29: Response of the FC for the frequency of the input impulse $f = 15$ MHz demonstrating of the pile-up of the signal.

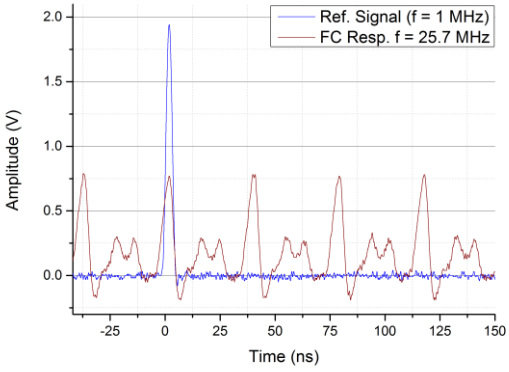

Figure 30: Response of the FC for the frequency of the input impulse $f = 25.7$ MHz demonstrating of the pile-up of the signal.

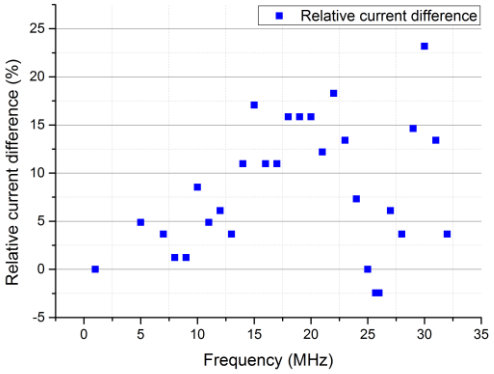

Figure 31: Difference between the measured amplitude as an output from the FC for various frequencies of the input impulse related to the amplitude for a frequency of $f = 1$ MHz.

For the first run of the non-invasive beam current monitor, the absolute treatment beam intensity determination was incorporated using a Keithely 486 Picoammeter [50]. A dedicated user interface was developed in LabVIEW (figure 32), to remotely manage the device during the experiment. The Picoammeter was placed in the direct vicinity of the FC to reduce both any signal losses along the cables and noise pickup due to their length. The measured average beam current was integrated in 50 ms intervals. A detailed description of the measurement method will follow in chapter 6.

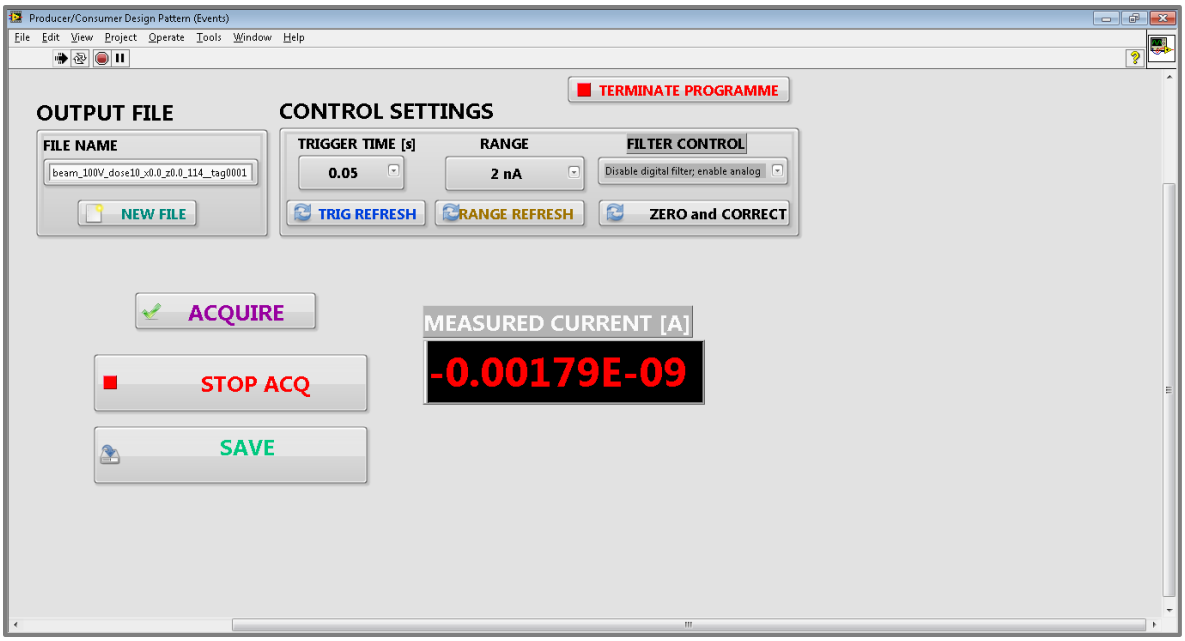

Figure 32. Interface for the FC cup GUI in LabVIEW.

Chapter Summary

This chapter gave a concise overview of beam current measurements for accelerators with a focus on Faraday Cups. The numerical modelling of the FC geometrical arrangement and material composition, in terms of induced charge loses when measuring with the proton beam at CCC, was presented. These supported the decision on the final geometrical arrangement of the beam stopper. The impedance matching theory was introduced and, ultimately, a response of the FC to nanosecond pulses was investigated in a laboratory to validate the final design.

4. LHCB VELO DETECTOR

The LHCb Vertex Locator (VELO) detector constitutes by far the most essential part of the proposed non-invasive beam current monitor. The architecture of the sensor was devised for the LHCb experiment at CERN to provide track coordinates of the secondary vertices from B-mesons decays in the investigations of CP violations and other rare phenomena [62][63][64]. To perform this task the detector must be placed several mm from the LHC beam without interacting with it as this would lead to irreversible damage.

The detector layout enables the precise position of particles crossing the sensors to be resolved by determining both the horizontal and radial coordinates. This advantageous arrangement was used in the final experiment at CCC, where the proton beam halo was monitored in the integration region with the beam line as a function of the radial distance from the beam axis. The radial information helped to find the sensitivity of the method as a function of different regions of the sensor.

Therefore, this chapter will provide an introduction to the principles of silicon detector operation, outline the sophisticated and complex architecture of both the VELO hybrids and the associated readout electronics and, ultimately, present the effect of work undertaken to allow operation of the detector in the air as a stand-alone beam current monitor for the proton facility at CCC.

4.1 Introduction to semiconductor detectors

Charged particle detectors make use of various available technologies and materials, e.g. digital or analogue readout systems, direct or indirect radiation-to-signal conversion, gaseous or solid state materials. In order to obtain a desired detection efficiency, their readout must be supported by sufficient levels of energy resolution and signal-to-noise ratio. The dense internal structure of semiconductors offers considerably better signal properties as opposed to the low density gaseous devices. This manifests in their reduced size and space requirement for operation. A shape of a silicon detector can be modified to adapt for the needs of an application. There is, however, a substantial cost associated with using silicon in physics experiments as it is prone to significant degradation of properties with a prolonged exposure to ionising radiation. Irreversible damages to the internal structure of the crystal lattice are invoked and often accompanied by chemical composition changes.

4.1.1 Semiconductor Materials

Semiconductors, such as silicon or germanium, are solid state materials. Their electric properties are determined by the internal crystalline structure, where electrons are allowed to occupy only certain energy levels, called *electron bands*. The separation between them, expressed in energy, is called the *forbidden band*. The value of the separation determines conductivity properties of solid state materials and for semiconductors it is of a few eV. [65]. As a result, solid state materials can be divided into three general groups:

- Insulators;
- Semi-conductors;
- Conductors.

The forbidden band in insulators has the largest energy separation, which reaches $5\ eV$ or more [66]. Both semiconductors and conductors fall below the above threshold and the conductivity properties depend on the structure of three bands:

- Valence;
- Forbidden;
- Conduction.

The lower band, called the *valence band*, contains electrons responsible for binding the atoms in the crystalline lattice with strong covalent bonds. Should these electrons gain sufficient energy to cross the *forbidden band*, they are relocated to the *conduction band* and become free to migrate. The excitation can happen by delivering energy to the crystal, for example as internal thermal energy or from outside by energy deposition by ionising or non-ionising radiation. Migration of electrons means they experience either diffusion in the crystal or are swept away by an external electric field becoming *conduction electrons*. A broken covalent bond left behind constitutes a positive charge in the valence band called a *hole*. Their charge also either diffuses in the crystal or get swept away by the same electric field. The movement of both electrons and holes characterises the conductivity of a semiconductor, where their contribution to the measured electric charge is equal, unlike in the gas-filled detectors. The movement of the electric charges in an external electric field in semiconductors, called *drift*, depends on the mobility of electrons and holes and for silicon at room temperature (300 K) they differ roughly by a factor of 2:

mobility of holes: $\mu_h = 1.1 \cdot 10^4 \ \mathrm{cm}^2/\mathrm{V} \cdot \mathrm{s}$ (35)

mobility of electrons: $\mu_e = 2.1 \cdot 10^4 \ \mathrm{cm}^2/\mathrm{V} \cdot \mathrm{s}$ (36)

The external electric field can be increased to a level, when the drift velocity of the charge carriers reaches saturation. Despite this, semiconductors have the highest response time to radiation among all the contemporary detectors. [66]

The pure (intrinsic) semiconductors have high resistivity at room temperatures as a result of concentrations of electrons in the conduction band and holes in the valence band being equal. This equilibrium can be changed by doping the crystal with donor or acceptor atoms, thus shifting the concentration of the charge carriers. Dopants substitute silicon in the crystal lattice and can either donate electrons to the conduction band or accept them and bind in the valence band. In either case the charge neutrality of a given semiconductor is maintained, however, the number of recombination events between the electrons and holes changes. Consequently, this leads to their unbalanced concentrations and influences the conductivity properties determined by migration of the majority charge carriers, hence giving rise to the conductivity of a doped semiconductor.

The *n-type* semiconductors are established with implementation of donor atoms. Their lightly bound electrons can be easily excited and raised to the conduction band. The equilibrium of an intrinsic material is lost at this stage and shifted towards higher number of electrons in the conduction band. This increases the recombination rates with holes and electrons become majority carriers.

The *p-type* semiconductors are established when acceptor atoms are introduced to the semiconductor lattice. The equilibrium of charge carriers shifts towards higher concentrations of holes in the valence band, which bind with electrons from the conduction band and holes become majority charge carriers.

4.1.2 Operation principles

When a charged particle traverses though a silicon detector it loses part of its energy in many interactions that lead to ionisation producing electron-hole pairs. In the normal operating conditions an external bias voltage is applied across a detector to separate the charges and decrease their recombination rate. Their drift happens consequently in the opposite directions,

where electrons migrate to a positive and holes to a negative contacts. These are made of blocking electrodes minimising the leakage current, typically $\mathrm{I_{leakage}} = 10^{-9}\,\mathrm{A}$. When the p- and n-type semiconductors are brought in contact, a favourable *p-n* junction is created. Here, electrons diffuse across to the p-side of the junction and holes to the n-side and recombine. This leads to a charge build-up on each side of the junction: negative on the p-side and positive on the n-side, creating a blocking contact called the *depletion region*. Any further diffusion of the charge carries across the junction is at this time stopped. Thus, any electron-hole pairs created in this region are separated and holes drift to the p-side whilst electrons to the n-side of the junction leaving this region without any free charges (figure 33).

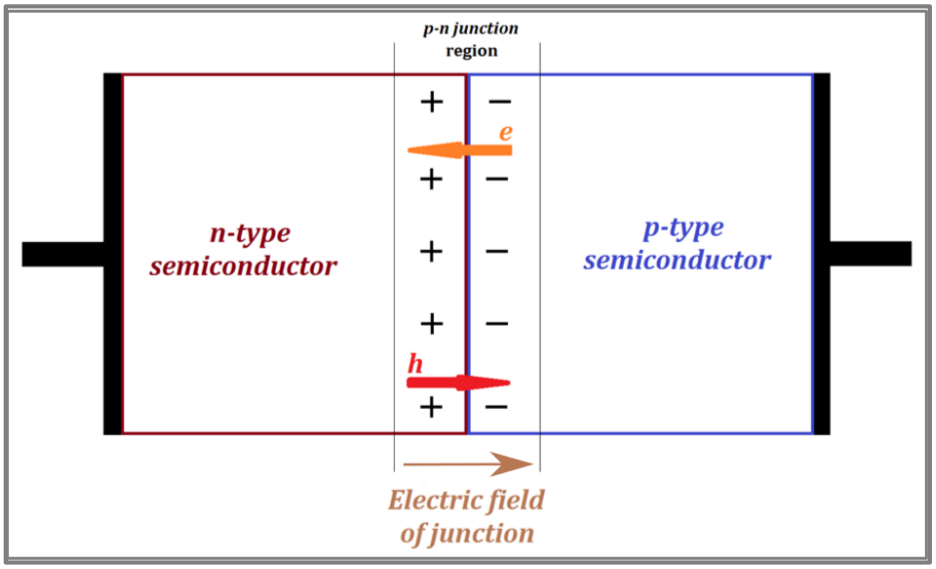

Figure 33. A schematic view of a depleted *p-n junction*. The orange and red arrows respectively indicate directions of diffusion of electrons and holes in the electric field induced in the junction. The junction can be extended to the full volume of the detector by applying a bias voltage to the electrodes.

The created *depletion region* can be extended further to cover the whole volume by polarisation of the crystal with an external, reversed bias voltage. Here, the negative potential is applied to the p-side and the positive potential to n–side of the junction. The required bias voltage necessary for the whole volume depletion can be estimated using the following formula:

$$V_D = \frac{eNT^2}{2\varepsilon} \tag{37}$$

where:

V_D - Full-volume depletion voltage, V;

N - Concentration of impurities, m^{-3} ;

T - Thickness of the wafer, m;

ε - Electric constant of the material, $\mathrm{F/m}$.

As a result, the capacitance of the junction decreases and the time / frequency response of the detector considerably improves. The lateral diffusion of the charge carriers becomes reduced due to short time of their collection. This is in contrast to the properties of either an unbiased or under-depleted mode of operation and allows fully-depleted silicon to be exploited as a position sensitive detector.

Concurrently, the *p-n junction* blocks the diffusion and drift of the majority carriers in one of the directions serving as a rectifier. The undesired diffusion of the minority carriers across the junction, known as the *leakage current*, can be reduced further by applying blocking contacts on each side of the bulk, preventing the charge injection. The contacts are created by heavy doping of the surface with atoms chosen to match the type of the semiconductor.

The leakage current plays a vital role in monitoring the extent of damage to the detector giving rise to its value with accumulation of the radiation-induced changes to the crystal structure. At the same time the higher leakage current flow decreases the effective value of the bias voltage, which is compensated for by constant rising of the bias potential with the lifetime of the detector, until it reaches the threshold of the crystal break down.

4.2 VELO technology

The VELO detector consists of a series of multi-strip silicon detectors that provide precise measurements of track coordinates of the charged particles originating from the interaction region of the LHCb experiment. Extensive studies had been carried out throughout the years to optimise the material performance and geometry. These can be studied in references [62][63][64][69][70]. The device was tailored to meet both the stringent requirements of operating in a high-level radiation environment in conjunction with facilitating data collection at high frequencies matching the bunch crossing at the LHC. A system of detector hybrids, figure 36, provides coordinates of the vertices in the polar coordinate system, r and ϕ, where the geometry of the sensors enables their sensitive area to approach the beam as close as 8.2

mm in the radial distance from beam axis. The proximity to the beam enables tracks to be resolved at high spatial resolution. This has also proven to be an advantageous design for the discussed application for the non-invasive beam current monitor tested at CCC, where the proton halo around the core of the beam was investigated without any interference with the very core. The design features, established for the operation at CERN, will be covered in the sections to follow. The principles of the detector integration with the LHC vacuum system will be explained to the extent, which is required to introduce the features of the monitor design discussed in this thesis.

4.2.1 History of the design

The VELO detector had to conform to the standards set for efficient operation of the detector on the LHC accelerator. These included a number of requirements involving *performance*, *geometry*, *environment* and *machine integration*.

The first and major task of the VELO detector is to precisely reconstruct tracks. Therefore stringent *performance* criteria had been set for the overall diode strip efficiency, essential in terms of the *geometry*, to preserve high spatial cluster resolution in the track reconstruction. [69] The cylindrical coordinate system of the sensors was introduced to decrease the execution time of the reconstruction algorithms and their semi-circular shape permitted for the inner sensors edges to be kept at a low distance of from the orbit of the beam, creating a safety margin for any undesired direct interactions. The signals had to be read out at the bunch crossing time, $\mathrm{f} = 40\ \mathrm{MHz}$, with the relative remnant of the peak after $25\ \mathrm{ns}$ not being higher than 0.3.

Harsh environmental conditions of operation, namely high radiation levels, necessitated using technology, which would not show fast degradation of properties owing to radiation-damage, and thus allowing for their operation at sustainable levels for three consecutive years. For the same reason, the heat generated by the readout electronics had to be efficiently dissipated by a dedicated cooling system, keeping the sensors at temperatures below $0℃$. This was also advantageous in slowing down the gradual increase of the bias voltage towards the break down value extending the life of the detector. The above aspects had to be incorporated in the design of the non-invasive monitor and will be outlined in the subsequent sections.

4.2.2 Architecture of sensors

Each VELO hybrid hosts two semi-circular multi-strip sensors manufactured as enriched *n-type* semiconductor strips in n-*type* base ($\mathrm{n}^+ - \mathrm{in} - \mathrm{n}$). Extensive studies on feasibility of materials showed that $\mathrm{p} - \mathrm{in} - \mathrm{n}$ technology demonstrated inferior spatial resolution due to larger lateral charge spread caused by under-depleted region forming around the p^+ strips. In due course, the under-depleted region acted like an insulator slowing down the collection of electrical charges. This was not observed for n^+ strips even for a low bias voltage and the cluster formation accuracy in signal processing was not affected for this type of technology.

Each sensor comprises of 2048 strips capacitive coupled (AC) to the readout lines. The electric isolation between them was achieved by exposing the silicon side hosting the strips to p^+spray.

The R-side sensor is arranged in four sectors, each hosting 512 diode strips. The pitch between them increases linearly with the radius of the detector r, providing the radial coordinates of crossing particles (figure 34), and can be expressed following equation (38). [63]

$$pitch = 40 + (101.6 - 40) \cdot \frac{r - 8190}{41949 - 8190} \ [\mu m] \tag{38}$$

The ϕ-side senor provides for the angular coordinates of hits utilising 2048 radially arranged diode strips. They are located in two regions, the inner embedding 683 strips and the outer hosting reaming 1365 strips. The radial coordinates of the strips span from $8.186\ \mathrm{mm}$ to $17.2105\ \mathrm{mm}$ in the inner region whilst the outer region extends from $17.2895\ \mathrm{mm}$ to $41.9894\ \mathrm{mm}$. [67] In both regions the strips are skewed anticlockwise and a stereo angle was introduced of 20° in the inner and 10° in the outer region (figure 34). This supports the real hits recognition in two adjacent detectors creating a pattern called a *dog-leg* shape. The pitch, in the inner region, increases with the radius: from $37.7\mu\mathrm{m}$ ($\mathrm{r} = 8.2\ \mathrm{mm}$) to $79.5\ \mu\mathrm{m}$ ($\mathrm{r} = 17.25\ \mathrm{mm}$). Respectively, in the outer region it changes from $39.8\ \mu\mathrm{m}$ ($\mathrm{r} = 17.25\ \mathrm{mm}$) to $97\ \mu\mathrm{m}$ ($\mathrm{r} = 42\ \mathrm{mm}$) and both can be described by two equations (39) and (40). [63][68]
Inner region:

$$pitch = 37.7 + (79.5 - 37.7) \cdot \frac{r - 8170}{17250 - 8170} \ [\mu m] \tag{39}$$

Outer region:

$$pitch = 39.8 + (96.9 - 39.8) \cdot \frac{r - 17250}{42000 - 17250}\ [\mu m] \tag{40}$$

Each type of the sensor is made of 300 μm-thick silicon with the back plate implanted with p^+ dopants to create a blocking contact. The side accommodating the strips was similarly exposed to $\mathrm{p-type}$ spray constituting the mentioned electrical insulation between the n^+ strips and the bulk of the semiconductor. Furthermore, this reduced the surface currents and micro-discharge events. In addition, an oxidised SiO_2 layer creates an AC coupling between the strips and routing layers, which feed signals to the readout electronics located at the circumference of the sensor (figure 35). The silicon plate is reversely biased by applying a depletion potential to the strip implants through $1\ \mathrm{M\Omega}$ poly-silicon resistors, which at the end of the life cycle of the detector may reach $\mathrm{U} = 500\ \mathrm{V}$. The main design features of the detector are summarised in table 7.

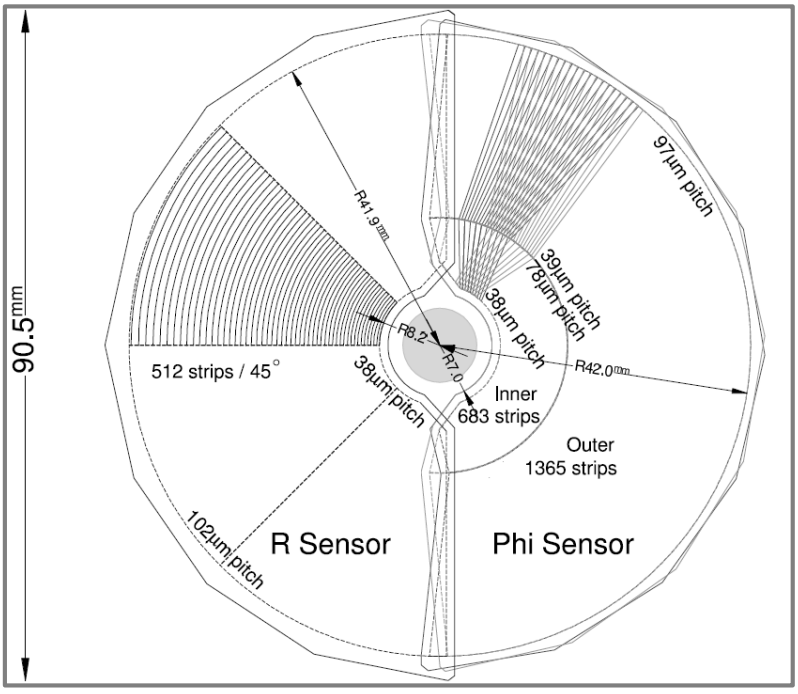

Figure 34. A sketch of two overlapping VELO modules summarising the features of architecture of the R- and ϕ- type sensors. [69]

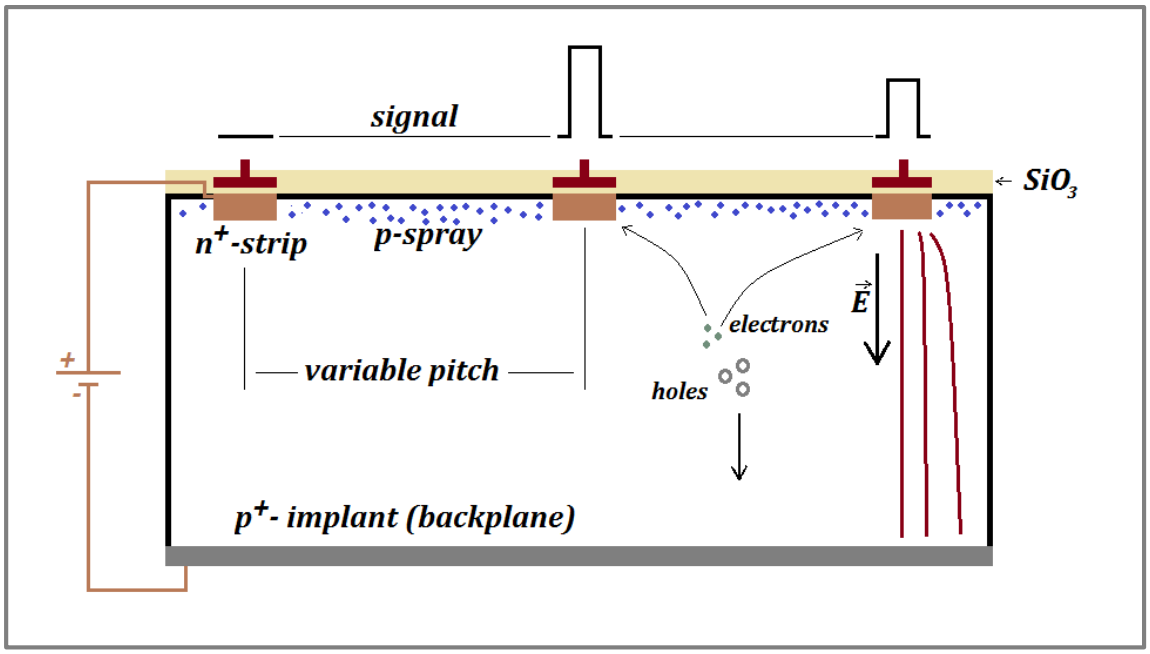

Figure 35. A cross-section through the VELO sensor. The bias voltage depletes the whole volume of silicon allowing separation of the electron-hole pairs created by a crossing charged particle. The differences in registered amplitude between the two adjacent strips caused by charge sharing allows the path through the sensor to be determined.

4.2.3 Detector hybrid

The VELO detector hybrid can be divided into three fundamental components:

- Sensors;
- Supporting base;
- Readout electronics.

The rigid mechanical structure creating the base provides reproducible fixing substrate of the sensors and accounts for their precise positioning in the experiment. It consists of a Thermo-Pyrolitic Graphite (TPG) core wrapped on each side with carbon fibre giving it good mechanical rigidness and also constitutes a base for the laminated circuits for the electronic components. The design is characterised by high thermal conductivity ($1700\ \mathrm{Wm^{-1}\,K^{-1}}$) allowing temperature control of both the sensors and Beetle chips. [71] The chips and sensors are glued to the hybrid following procedures sustaining high and reproducible accuracy of their distribution. The chips are responsible for the read out of signals from the sensors, first storing and, eventually, transferring them to further electric components for pre- and post-processing.

Table 7. Design features of the VELO sensors.

	$R-$ sensor		$\phi-$ sensor	
Silicon technology	n^+-in-n		n^+-in-n	
Number of readout channels	2048		2048	
Thickness of the sensor [µm]	300		300	
Number of sectors (R) / regions (ϕ)	4		2	
Smallest pitch [µm]	38.0		37.7	
Largest pitch [µm]	101.6		97.0	
Radius of active area [mm]	Min.	8.1700	Inner	8.1860 – 17.2105
	Max.	42.0000	Outer	17.2895 – 41.9840
Angular coverage [degrees]	180		≈ 182	
Stereo angle [degrees]	Min.	-	Outer	10.35
	Max.	-	Inner	20.00

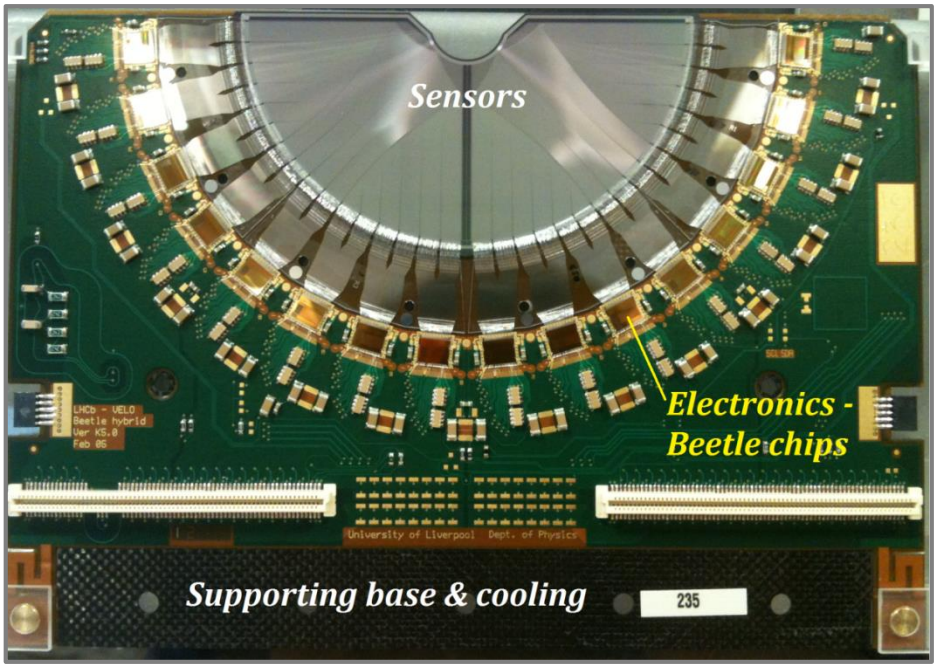

Figure 36. The VELO hybrid N$^{o.}$ 235 as an example depicting of three fundamental constituents of the detector.

There are, altogether, 32 Beetle chips mounted on one hybrid, 16 per side, each reading out 128 strips at a time. The significant power required for their operation releases approximately 27.5 W of waste heat, which needs to be dissipated. To support this process, the

chips are coupled with the TPG base connected to heat sinks, at CERN in the form of *cooling cookies*, containing liquid CO_2. Thus, the sensors are kept at a steady temperature of -7 ℃, falling between the boundaries of the long life-cycle operation temperatures determined to be between -30 ˚C and 0 ˚C. [74] The above assumptions were accommodated and implemented in the design of the cooling system for the non-invasive beam current monitor and are subject to discussion in the sections to follow. The continuous monitoring of the hybrid temperature was implemented though two Negative Temperature Coefficient (NTC) sensors.

4.2.4 Electronic components

The readout electronics includes both the analogue and digital elements. This is strongly linked to the environmental conditions and available space at the LHC. The signal processing itself is performed at several stages on dedicated processing cards. Normally, the layout of electronics can be grouped as:

- Primary analogue part: front-end electronics (Beetle chips) and boards responsible for signal amplification and transfer to the processing cards. This is managed by the repeater cards, which also distribute power to the hybrids, transfer the bias voltages and receive Time and Control Signals;
- Secondary digital part: performing digitisation and signal processing on TELL1 cards (figure 47).

In terms of the readout management, these can also be divided into two groups: L0 and L1 electronics. The L0 elements, the Beetle chips, accept the readout triggers from repeater cards and TELL1s. The L1 trigger signals come from the L1 components, explicitly the LHCb experiment data acquisition triggers and are accepted by TELL1 cards.

Beetle Chips

The Beetle chips were custom-made for readout of the VELO sensors and, in order to withstand harsh radiation environment at LHC, the CMOS technology was implemented. More specific information on their architecture can be found in reference [71]. Each chip accommodates 128 charge amplifiers that receive signals from the routing layers. The collected charge is formed by active CR-RC shapers and sent to the buffer storing 160 sampling intervals in a pipeline. The signals are multiplexed on four differential output lines transporting them to the repeater cards. The chips accept events at the frequency matched with the LHC bunch

crossing at $f = 40\ \mathrm{MHz}$ by receiving commands from the repeater cards via I^2C protocol. The pipelines on the chips release the data at the same frequency, however, the readout trigger arrives every 900 ns downgrading the data transfer frequency to 1.1 MHz (L0 trigger). There is one additional channel, called a *dummy channel*, which provides output signal that can be subtracted from the analogue signals to compensate for the common mode effects. Timing of the chips plays an important role in accepting the events by the Higher Level Trigger (HLT) in the experiment. On leaving the chip, pulses are ought to meet very strict requirements: the rise time must not exceed 25ns and the reminder of the maximum peak amplitude, after 25 ns, must be lower than 30% (figure 37). These can be tested using charge injectors integrated on every line, which can source test pulses.

The mentioned data synchronous readout with the bunch crossing frequency was not implemented in the first run of the non-invasive monitor due to the extent of complexity of its adaptation.

Data pulses leave the hybrid via Kapton cables. In the original design they constitute a flexible connection between the retractable modules and the stationary feed-though flanges. For the purpose of the application here, they were modified and created a fixed connection between the hybrid and the dummy cards permitting to introduce a sealed border between the dry air shroud and the ambient air. The flexible connection was provided by ribbon cables instead, connecting the dummy cards with the repeater boards. The cables supplied hybrids with low voltage (LV) for powering the Beetle chips, bias voltage for the sensors and I^2C commands. From here the signals were transferred onto repeater boards

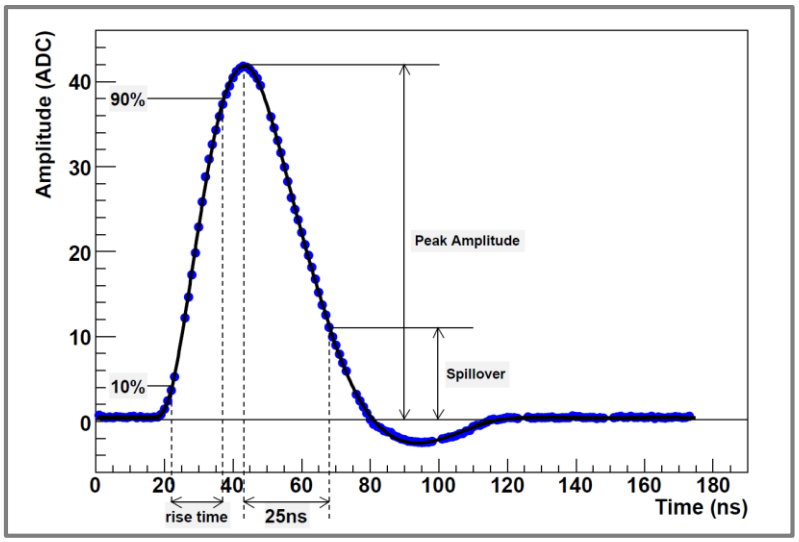

Figure 37: The Beetle chip test pulse shape. [71]

Repeater Boards

They accommodate 6 mezzanine cards which accept data from 64 links coming from one side of the hybrid (sensor), manage both power and command distribution and enhance shape of the pulses for sending them to the digitizers via 60 meters long, shielded twisted pair cables (CAT6 cables). The amplification is essential to equalize the pulses accordingly to account for signal distortions introduced by the long transfer cables. Two repeater cards are required per hybrid to readout data from both R- and ϕ-sensors.

One of the on-board mezzanine cards, the LV card, receives the Time-and-Fast Control (TFC) signals and sends them further to the Beetle chips, the L0 trigger. The LV card supplies power for the front end chips, analogue driver cards and Experiment Control System card (ECS). TFC system supplies beam-synchronous clock from so called *Beam Supervisor* to all the readout systems in the experiment in order to synchronise them with LHC orbit receiver / clock. [5] This system was removed and bypassed in the adaptation of the detector to work outside CERN environment.

The last on-board mezzanine card – ECS - forwards $\mathrm{I}^2\mathrm{C}$ commands to the chips and controls the LV regulators.

TELL1 boards for LHCb VELO

High radiation level in the proximity of the VELO detector is damaging to the optical links of the TCS network or signal receivers from the Beetles. Therefore, the digital components involved in data processing together with the CS components are hosted on a separate dedicated card, called *TELL1*, located outside the LHC tunnel. They receive the analogue signals, transmitted via the transfer cables, and perform various pre-processing operations:

- Digitisation;
- Pedestal calculation;
- Header cross-talk correction;
- FIR filtering;
- Channel reordering;
- Common mode suppression;
- Clustering.

The pre-processed data is stored in buffers until the L1 trigger arrives to start transfer to the HLT computers. Two formats of the output data, produced by the TELL1s, are supported and can be accepted by HLT: *zero-suppressed* (ZS) and *non-zero-suppressed data* (NZS), where the latter carries the full raw data information per strip and was used in the experimental data analysis outlined in chapter 6.

Four analogue receivers - ARx cards – accept signals on the TELL1. Each card has 16 links to accommodate data coming from the Beetle chips on one side of the hybrid. The cards digitise data with a 10-bit precision at frequency of 40MHz. ADC digitisation is synchronised with time of the data arrival from the Beetle chips, namely adjusted to nanosecond skew delay that originates form the transfer along the CAT6 cables. A new set of the calibration parameters was determined to the shortened cables, which were assembled for the experimental work in this dissertation.

Once the digitisation has been performed, data pre-processing can be commenced on 4 pre-processing FPGAs to prepare it for sending to the HLT.

The first operation of pre-processing that takes place is *pedestal subtraction*. It compensates for individual signal response of the channels originating from both chip-to-chip and link-to-link variations. This correction forces data in the consecutive channels to have more

uniform distribution (figure 38) providing also compensation for their variations in time. The values of pedestals are set to approximately 512 ADCs, equal to half of the available range for 10-bit data. In order to monitor the pedestals, a moving average pedestal following algorithm has been developed, where the values are either calculated based on the current data set or saved beforehand in the HLT databases, accessible and restored by ECS. This approach allows avoiding any additional operations to be performed on TELL1s. The pedestal following algorithm was disabled in the course of the data collection and analysis. A fixed value of pedestals per strip was used, calculated for the events collected before the actual measurements with the proton beam for the detector installed in the experimental space.

Header cross-talk correction is essential due to the way the analogue data transmission is organized. As the data from 32 channels is sent from Beetle chips via four links, the first four bits of the data train, called the *headers*, carry information about the pipeline column number as an identifier of the origin of the signal.

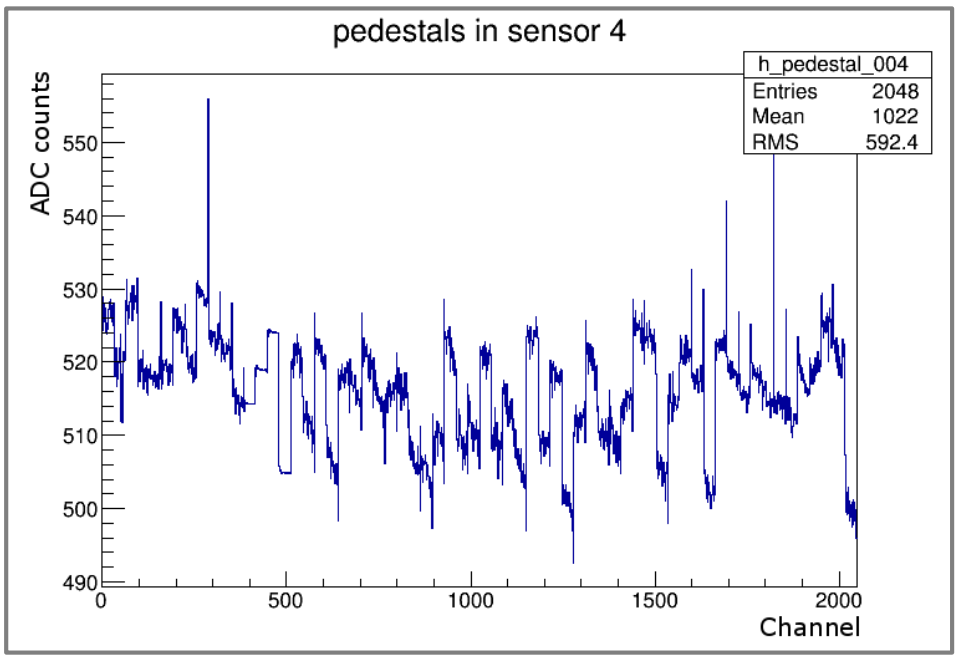

Figure 38: An example of the calculated pedestal values for the $\mathrm{R}-$ sensor.

The last bit of the headers frequently spills over on the first bit of data distorting it. Additional deformation may also come from the long transmission cables between the Beetle chip and TELL1. Uncorrected headers could contribute to the false cluster seeding due to the

values exceeding the seeding thresholds. [78] To compensate for it, the previously mentioned set of calibration parameters for the new cables was determined.

A finite impulse response (FIR) filter corrects for effects of pulses distortions once they pass through the low-pass, long transfer cables between the repeater and TELL1 cards.

Channel reordering links the physical channels on the sensors with electronic channels assigned to Beetle chips. Physical channels readout is not arranged in ascending or descending order. On the ϕ-sensor the second and third strip, out of a group of four, are read out in an inverse order. On the R–side the readout channels are arranged according to geometry of the sectors, namely two external channels of the chip carry information from strips from 0 to 255, whilst strip channels from 256 to 511 are transferred on two middle external links. The pattern is repeated for each sector. The physical order of the channels is essential to determine the common noise shape in the data.

Common mode suppression corrects for any common noise there might appear on the sensors using Mean Common Mode Suppression algorithm (MSCS). This type of noise is produced by RF pickup from an accelerator, variation in the front-end chips performance triggered by power instabilities or simply any noise picked up by the analogue readout. The correction is applied to 32 channels on each of the links of one Beetle chip. A simple linear regression function is used for event-by-event data as a measure of the baseline offset for an event. [70] The MCMS algorithm was disabled during analysis what will be addressed and explained in chapter 6.

Clustering is performed once all the previous steps have been completed. It takes place on TELL1 boards and depends on the amplitude (ADC counts) of the digitised charge value. There are two thresholds that determine the extent of the cluster: seeding threshold - when the cluster is determined - and inclusion threshold – when additional strips constituting the cluster are added to the seeding strip. There can be up to four strips building one cluster. A centre of it can be also determined using a weighted average, where the weights depend on the ADC values. [79][80] Although clustering wasn't used in the data processing, a threshold equivalent to the seeding threshold was introduced to suppress noise and events with low quality of amplitude. More detailed threshold determination is also discussed in chapter 6.

4.3 Detector integration with the treatment beam line at CCC

With regard to the previous paragraph, the VELO detector was designed to be operated in vacuum. Integration with the accelerator and the treatment line at CCC required necessary adaptations of the existing technology to adjust it to the environmental conditions of the medical facility without any potential alterations to any of the characteristics of the treatment beam. This significantly restricted space availabale for the integration and the only possible area was indetified that fell between the modulator box and diagnostic box, integrating the parallel-plate ionisation chamber (ppic), figure 39. Therefore necessary adjustments were initiated to permit operation of the detector in air.

A precise positioning of the detector in both the beam propagation direction (z) and the transverse plane (x) had to be devised. To reduce the radation damage to the sensors, a dedicated cooling system was designed to keep the hybrids at temperatures below $0°C$ at the waste heat load of 32 W. Operation of the detector at temperatures below the dew point of the air necessitated protecting the hybrids from water condensation. Therefore, the integration of the detector considering the above requirements is subject to discussion in the following sections.

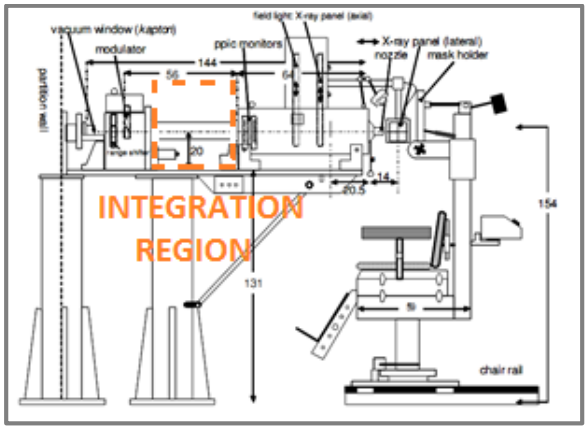

Figure 39: CCC treatment beam line: the integration space is between the beam modulator box and parallel-plate ionisation chambers in the diagnostics box.

4.3.1 Integration

With reference to figure 39 the outlined space was the only possibility for accommodating the VELO detector to characterise the performance of the non-invasive beam

current monitor based on beam halo measurements. A number of different requirements were set for the performance and positioninig of the detector:

1. Operation of the detector in ambient air at the temperature of the silicon sensors between -5 ℃ and 0 ℃.
2. Positioning of the detector in the beam propagation direction z with an accuracy 0.1 cm.
3. Available stroke in the z direction: 15.0 cm from the initial position of the detector set to no more than 10 cm from the exit of the modulator box.
4. Poitioning of both VELO modules in the transverse plane (x) to the beam proagation direction with an accuracy of 0.1 cm.
5. Stroke of the detector travel in x from 0.0 cm, when both modules are adjacent, to 9.0 cm.
6. Each VELO module should be positioned co-centrically with the beam axis when both detectors are at $x = 0.0$ cm at any point along the z axis.

A dedicated stand was designed and comissioned on the beam line prior to the experiment to cover the requirements. Three MacLennan THK translation stages [84] fitted with independently controlled MacLennan stepper motors [83] were used to provide for precise postioning in both axes. The achieved accuracy was better than stated above, namely 10.0 μm in the z axis and 5.0 μm in the x (table 8). The slides were fitted on a thick and rigid top stainless steel plate mounted on an aluminium frame. The stepper motors were powered and controlled by SM9859 three axis control unit, custom made and delivered by McLennan.

Table 8. Characteristics of MacLennan THK linear slides integrated with a stand for VELO positioning. [21]

Slide type	Axis	Steps / revolution	Distance / revolution [mm / rev]	Resolution [μm]	Travel range [mm]
THK KR20	X	20000	1.0	10.0	94.0
THK KR26	Z	20000	2.0	5.0	165.0

The latter hosted three microprocessor-based ST5-Q controller / driver units [83] which provide the control and drive outputs for McLennan 17HS motors [85]. They operate independently on shared communication channels using RS485 USB connection. The full control of the motors can be either remote or manual, when a MSB811 jog is used.

Table 9. Basic characteristics of McLennan 17HS stepper motors coupled to the translation slides.

Motor type	Axes	Steps / revolution	Coupling
17HS-240E	X,Z	200	With the slides

The controllers are coupled with the motors using RS232 ports and cables, one for each controller-motor pair. They also store information about the driving currents and motor address for the communication. *Baumer swithes*, fitted at every end of the slide, determine the detector movement limits within a micro-metre precision. [86] To account for the reroducibility of positioning, precautions were made to avoid bringing the system to a halt in an abrupt manner when reaching the switch and calibration of the limits was intorduced. These were saved in the controllers, for each of the slides separately, to prevent loosing / skipping of steps due to the inertia of the set-up. Furthermore, decceleration before the switches was introduced to guarantee the nominal positioning reproducibility and a smooth movement of the detectors. The control of these parameters was commenced by a dedicated motor controller interface written in National Instruments LabVIEW environment [87]. At the startup of the system, a full calibration of the limits was performed after the translation speed had been decrased to $5\,\mathrm{mm/s}$ and acceleration / deceleration rate were set below the default value. The interface also allowed to either re-calibrate the limits at any time of operation or alter the translation speed. The movement in either of the axes could be performed in idependent or coupled increment in x for either of the hybrids.

The interface communicated with the ST5-Q motors via RS485 using Serial Command Language (SCL) developed by Applied Motion. [88] The hardware required was minimized to a computer sending out the comands in a form of simple strings for invoking e.g. triggering of the motion, control of the inputs and outputs or changing configuration of the motors.

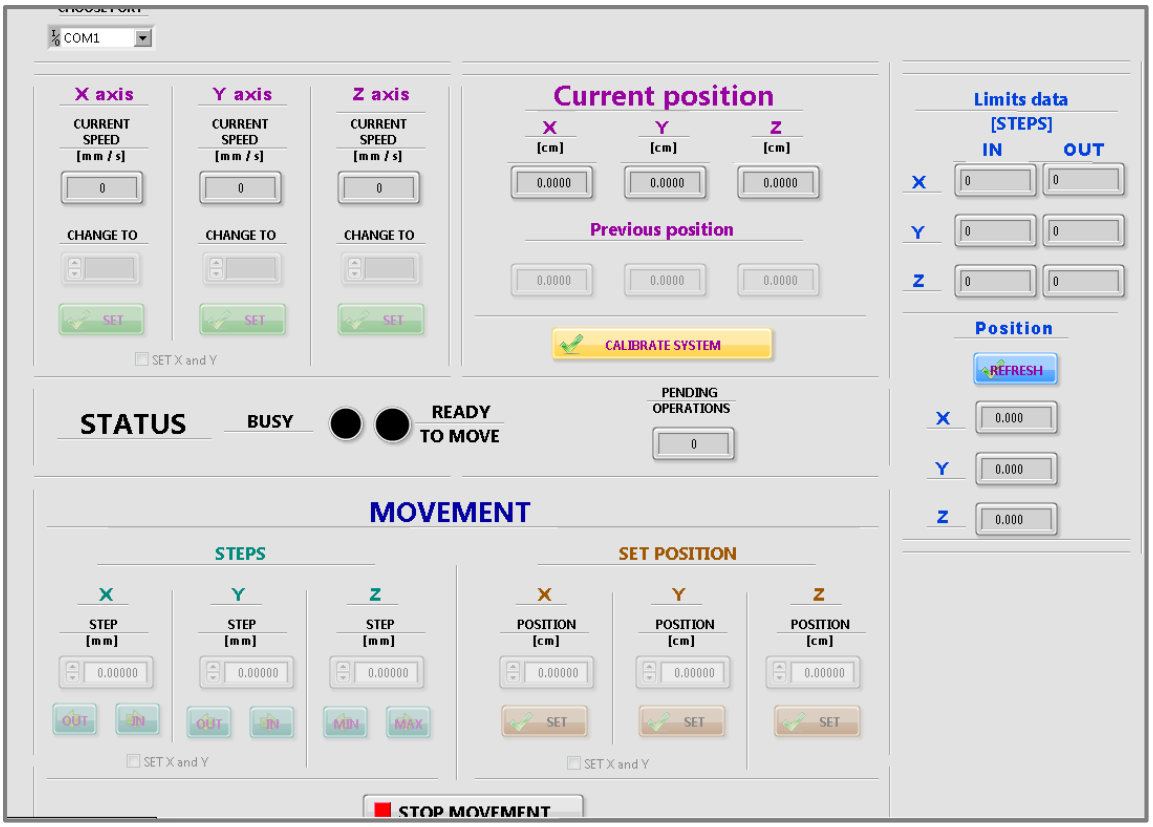

Figure 40: Layout of the motor controller pane in the NI LabVIEW code.

The top base plate hosting the slides, as outlined previously, was suppported on a rigid frame made of aluminium profiles by Machine Building Systems. The stand was coupled to a bottom base plate placed directly on the treatment beam line. Four height – adjustable feet screwed into each of four aluminium stems were used to level the stand and correct for uneven surface creating a stable support (figure 41).

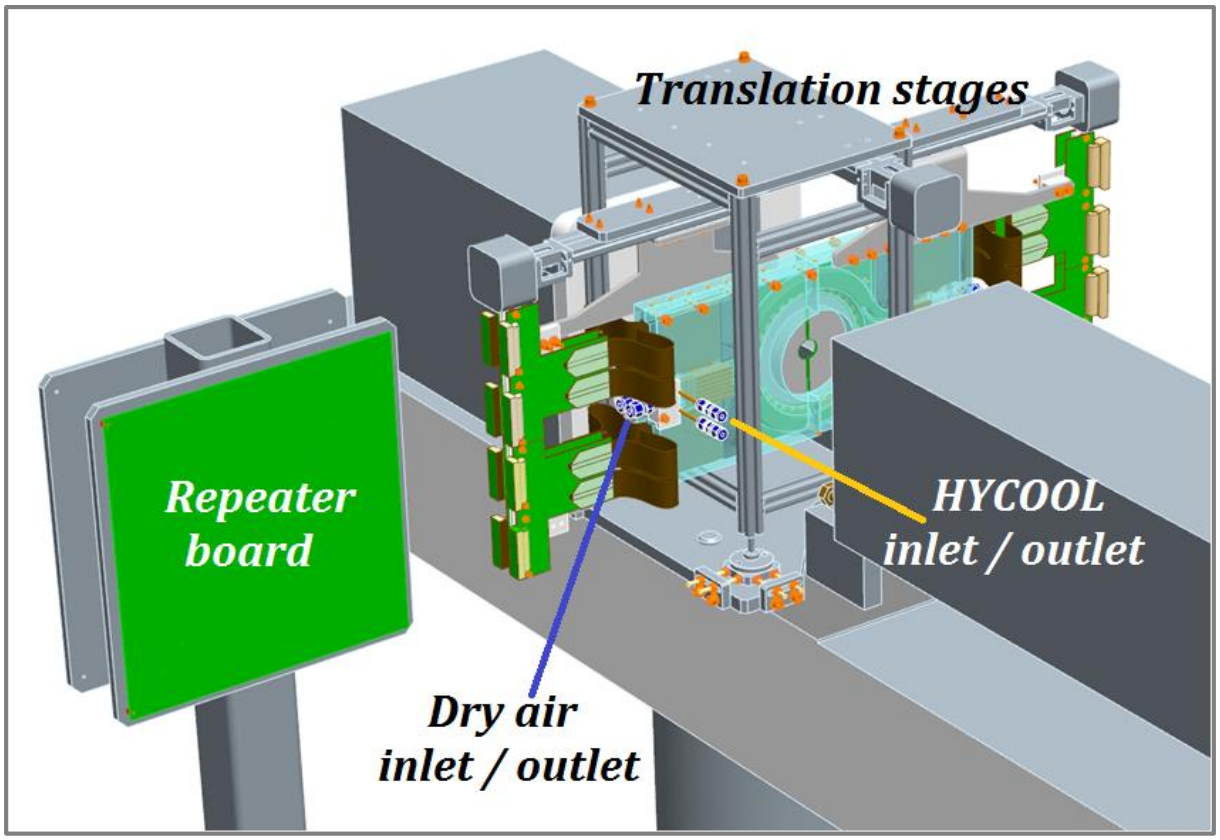

Figure 41: Outline of VELO integration with the treatment line at CCC.

Each of the VELO hybrids was fitted inside a machined acrylic dry air shroud. A semi-circular opening of the shrouds enabled the silicon sensors to be exposed to the treatment beam halo. The clearance between the rim of the semi-circular area of the shroud and the TPG base of the hybrid was $5\ \mathrm{mm}$, sufficient to accommodate the *vias* (bondings) transferring signals to the read out chips. At the same time the clearance was sufficient to create a quasi-laminar flow of dry air along the whole area of the sensors. Operation at a full power of both the cooling system and Beetle chips showed that the dry air shrouds were capable of maintaining the surface of the sensors free of condensation at temperatures around $-15\ ℃$ creating an efficient isolation of the modules from the ambient air. Dry air was supplied form Ekom DK50 2V-S/M air compressor with a dryer at the pressure of $4.0 - 4.5\ \mathrm{bars}$ for the dew point defined by the manufacturer at $\mathrm{T} = -20\ ^{\circ}\mathrm{C}$.

4.3.2 Cooling and handling of waste heat

The silicon sensors require operation at stable low temperatures to protect them for excessive increase of radiation damage and maintaining constant noise level. One of the

available options to compensate for these changes in the structure of silicon is a gradual increase of the bias voltage, limited by the mentioned *breakdown voltage*. Beyond this, silicon structure sustains irreversible damage and loss of properties. Additionally, as outlined earlier, the produced heat load of 27.5 W per hybrid must be taken away in order to prevent the glue, used for fixing the chips, from melting. The above factors and especially the increase in the leakage current can be controlled throughout the lifespan of the detector by keeping it at low temperature of around -7 ℃. The designated VELO Thermal Control System (VTCS) manages the thermal aspects of the detector operation at CERN [74], where it is a 3 tier system utilising commercially available chiller units. The waste heat is taken away through evaporators, small rectangular aluminium blocks with embedded coolant pipes inside that attach on one side to an exposed part of the TPG/carbon fibre base of the detector, called a *cooling strip* (figure 36).

The concept of utilising the VELO detector as a stand-alone monitor at CCC demanded re-investigation of the thermal aspects of operation. A set of simulations of the heat transfer were carried out, in collaboration with the STFC Design Office, using Finite Element Analysis (FEA) in order to determine the minimum requirements for the elements for the cooling system, such as a chiller or pipework.

Heat transfer, either within the same material or between different materials, occurs whenever there is a difference in temperature. The heat exchange can be either direct or indirect and there are three general models distinguished: *conduction*, *convection* or *radiation*. The first two take place at a molecular level, whilst radiative heat exchange is performed through either infrared or nearly visible spectrum of the electromagnetic waves. The quantity of heat transferred by conduction in one dimension between two points at different temperatures $\mathrm{T}_1$and T_2, can be expressed by the *Fourier's law* [89]*:*

$$\rho c \frac{dT}{dt} = -k \frac{dT}{dx} \tag{41}$$

where:

$\frac{dT}{dt}$ - Heat flow, W;

$\frac{dT}{dx}$ – Temperature gradient between two points of temperatures $\mathrm{T}_1$and T_2;

ρ - Density of a given material, $\mathrm{kg/m^3}$;

c – Heat capacity, $\mathrm{J} \cdot \mathrm{kg}^{-1} \cdot \mathrm{K}^{-1}$;

k – Thermal conductivity, $\mathrm{W} \cdot \mathrm{m}^{-1} \cdot \mathrm{K}^{-1}$;

The convective heat transfer takes place in gases and liquids. The molecular velocity of these particles depends on the temperature of medium. When a molecule or a particle is in contact with a surface of higher temperature, thermal energy transfer takes place increasing its speed. Therefore, they drift away from the surface of contact crating convection. The convective heat transfer can be described by equation (42). [89]

$$Q_c = h(T_S - T_F) \tag{42}$$

where:

Q_c – Convective heat flux, W;

h - Convection heat transfer coefficient, $\mathrm{W} \cdot \mathrm{m}^{-1} \cdot \mathrm{K}^{-1}$;

T_S, T_F – Respectively: the temperature of the surface and the fluid of gas.

The radiative heat losses occur because of emission of the electromagnetic waves from a surface of a real body. A mathematical description of the phenomena can be expressed using the *Stefan Boltzmann's* law [89]:

$$Q_E = \varepsilon \cdot \sigma \cdot T_S^4 \tag{43}$$

where:

Q_E – Radiative heat flux, $\mathrm{W} \cdot \mathrm{m}^{-2}$,

σ – Stefan Boltzmann's constant, $5.699 \cdot 10^{-8}\ \mathrm{W} \cdot \mathrm{m}^{-2} \cdot \mathrm{K}^4$,

T_S – Temperature of the surface, K.

Solving the heat transfer problems for bodies with complicated geometries may be difficult to obtain using analytical methods as, in general, the solutions of analytical methods are based on solving a system of differential equations. This calculation process can be simplified to solving a set of simple linear equations when numerical methods, such as FEA, are used. [91] The process is made out of four stages:

- *Discretisation* of the system, when the complex geometries are divided into an assembly of finite number of smaller elements interconnected one to another by nodes. Elements may be approximated by different interpolation functions both linear and non-linear. Their shape depends on the geometry of the body and gives an approximation of the overall shape;
- *Characterisation*, when a set of equations describing the thermal properties of the element is created. Each node is characterised by an unknown temperature value and but known heat load;
- *Assembling* when equations of all the elements are assembled together creating a matrix of the equations describing the behaviour of the whole system;
- *Solution* of the linear equations.

The linear notation of the global system is reduced to an equation:

$$[K] \cdot (T) = (f) \tag{44}$$

where:

$[K]$ – Global conductivity matrix that consists of a set of single element (e) conductivity matrices for all the elements:

$$[K]_e = \frac{k}{l} \begin{bmatrix} 1 & -1 \\ -1 & 1 \end{bmatrix} \tag{45}$$

k – Thermal conductivity,

l – Distance between the nodes of the one-dimensional element

(T) – Global temperature vector for every single element

(f) – Global load vector that consists of the load vectors for single elements e:

$$(f)_e = \begin{pmatrix} Q_i \\ Q_j \end{pmatrix} \tag{46}$$

Q_i, Q_j - total heat transferred to the nodes building the element.

Pro/Engineer Mechanica software package was used to resolve the heat transfer problem for the VELO module. The detector was divided into smaller elements to reflect on the geometry especially in the area of the Beetle chips and the waste heat was uniformly divided between 16 corresponding spots. The hybrid itself was modelled as uniform slab of Thermo-Pyrolytic Graphite of the thickness $x = 1\,mm$ and the thermal conductivity coefficient $\mathrm{k} = 1800\ \mathrm{W \cdot m^{-1} \cdot K^{-1}}$ (figure 42).

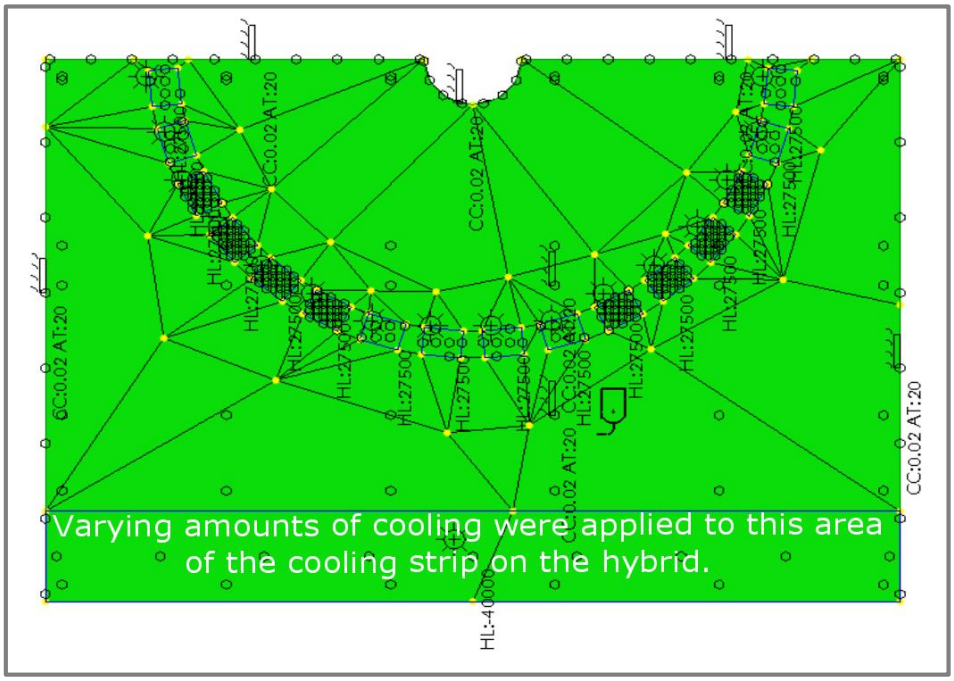

Figure 42: FEA discretised model of the VELO hybrid as an input for the Finite Element Analysis of the heat transfer.

The dry air shrouds in the model were assumed to consist of dry nitrogen at the temperature of $20\ ℃$ and the air flow rate of $1\ \mathrm{m/s}$. A convection model was applied to the whole area of the hybrid with an exception for the cooling strip, which was attached to a cooling copper block. The maximum convection factor was assumed to simulate the heat transfer from the gas molecules to the hybrid, $\mathrm{h} = 20\ \mathrm{W \cdot m^{-2} \cdot K^{-1}}$.

The thermal coupling between either the copper cooling block or the chips and the hybrid were set to have perfect thermal conductivity. This brought forth the overestimated power of the chiller as opposed to the case, when a non-perfect coupling of the elements had been considered.

Rough calculations demonstrate that the total heat-load should be approximately $\mathrm{Q_T} = 34.6\ \mathrm{W}$ consisting of the heat flux to the hybrid due to convection of the dry air $\mathrm{Q_C} = 7.1\ \mathrm{W}$ and the waste heat produced by the chips $\mathrm{Q_B} = 27.5\ \mathrm{W}$. The outcome of the FEA simulations proved furthermore that in order to keep the sensors at a temperature of approximately $\mathrm{T} = -7\ ℃$ the cooling power per hybrid should not be lower than 40 W. The results can be investigated in figure 43 and a summary is to be found in table 10

. A contingency of at least $15 - 20\ \mathrm{W}$ per sensor was added to account for heat transferred to the coolant in the pipe work between the chiller and the inlet to the detector shrouds. The sum of all the values provides an indication for the minimum power of the chiller required $\mathrm{P} = 130\ \mathrm{W}$ at the temperature $\mathrm{T} = -27\ ℃$.

To reduce the heat absorption in the pipework, 19 mm thick Amaflex polyethylene insulation was used. This efficiently eliminated issues with the condensation build-up on the tubing.

The provided insulation had to be yet thick enough to exclude condensation build-up on its surface. To find the temperature of the surface, the heat conduction (41) and convection (42) formulae were equalised for a steady state case. The amount of the heat transfer due to the convection must be equal to the conduction across to the insulation. As a result, the temperature of the surface can be found by solving the equation:

$$T_{surface} = \left(\frac{k}{x} \cdot T_{inside} + h \cdot T_{air}\right) \cdot \frac{1}{h + \frac{k}{x}} \tag{47}$$

where:

k - Polyethylene thermal conductivity coefficient, $0.034\ \mathrm{W \cdot m^{-1} \cdot K^{-1}}$;

h - Surface convection coefficient for polyethylene $\mathrm{h} = 5\ \mathrm{W \cdot m^{-2} \cdot K^{-1}}$;

x - Thickness of polyethylene layer, $\mathrm{x} = 19\ \mathrm{mm}$.

For the temperature of the coolant in the pipe $\mathrm{T_{inside}} = -27\ ℃$ and the ambient air temperature $\mathrm{T_{air}} = 20\ ℃$, the temperature at the surface of the insulation should be equal to $\mathrm{T_{surface}} = 7.6\ ℃$ and overlaps with the dew point of the air at the relative humidity of 90.0 %. As the treatment room at CCC was equipped with air conditioning, bringing the actual

dew point lower, the thickness of the insulation proved to be sufficient to support the dry operation of the set up.

Table 10. A summary of the results of the FEA for the VELO detector cooling system.

	Silicon sensor temperature [℃]	
Cooling power [W]	Lowest	Highest
10.0	14.6	15.6
40.0	-8.8	-7.6
50.0	-32.4	-30.1

The tubing was terminated with a copper heat exchanger bought in thermodynamic contact with the cooling areas of the VELO modules by applying a layer of 1 mm thick silicon based $\alpha - Gel$ COH-6000LVC by Taica Corporation. [95] A careful treatment of the coupling allows to re-use the gel for a few runs. A pipe, bronze-welded in copper, carried the low viscosity coolant – HYCOOL – allowing for sufficiently high transfer thought the system owing to low viscosity at $\mathrm{T} = -22$ ℃. [93] In addition, two square radiators were fitted symmetrically on the copper block to make available heat exchange with the dry air to lower its temperature (figure 44).

The cooling pipes were fed outside the shrouds and connected to the elastic tubing wrapped in the described polyurethane insulation leading them to a chiller (figure 44). A K3 series chiller [92] has been selected because of high cooling capacity if offered, 3200 W, defined for water at the temperature of $+17$ ℃. The chiller was able to keep the coolant at a steady temperature of -27 ℃ at the entrance to the shrouds for the fully powered Beetle chips.

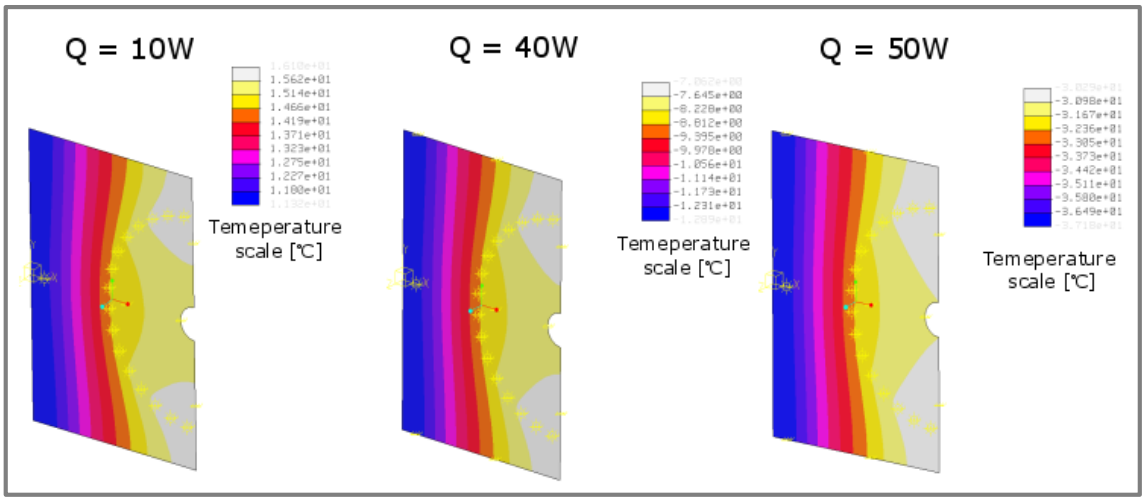

Figure 43: Results of the FEA simulations where the rainbow temperature scale presents the results of the simulations for three different cooling power values applied to the cooling strip on the hybrid.

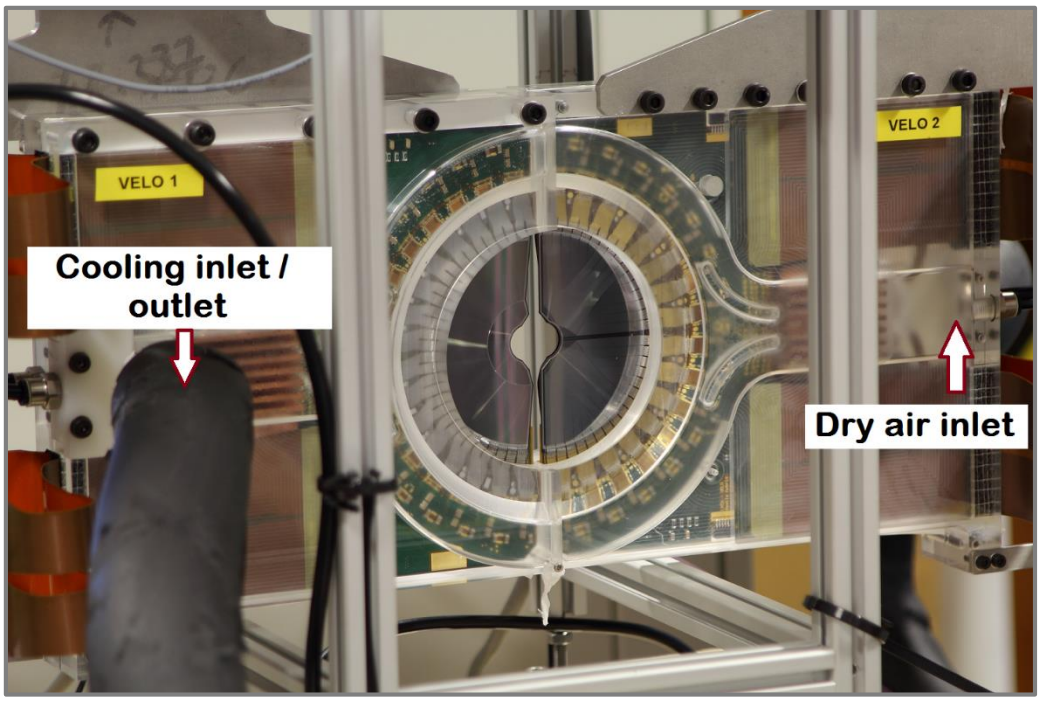

Figure 44: The final design of the stand for integrating the VELO detector with the treatment beam line at CCC.

4.3.3 Alignment

Two cross-shaped stainless steel targets were machined to align the detector with the axis of the beam through their precise positioning on the stand at its two opposite ends in the beam propagation direction (z). The reproducibility of the positioning was assured by carefully chosen geometry of the holders. The intersection points of crosses were co-centrically aligned

at the same time with both the beam axis and the centres of the sensors at the transverse position $x = 0.0$ cm (figures 45 and 46).

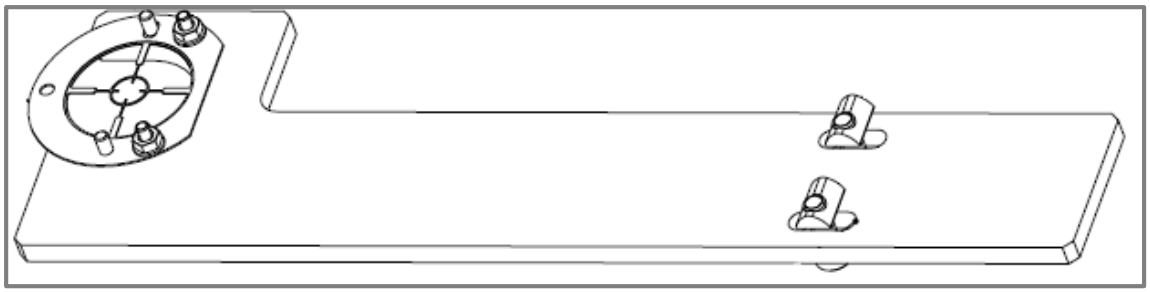

Figure 45: The aluminium holders for marking the position of the axis of the beam and the central axis of the stand.

The adjustment of the level in the axis perpendicular to the beam axis was obtained by using a digital spirit level resting on the top base plate. A dedicated aluminium boss was designed to sit tightly on the end of the beam line Kapton window assembly hosting a diode HLM1230 laser to simulate the proton beam axis.

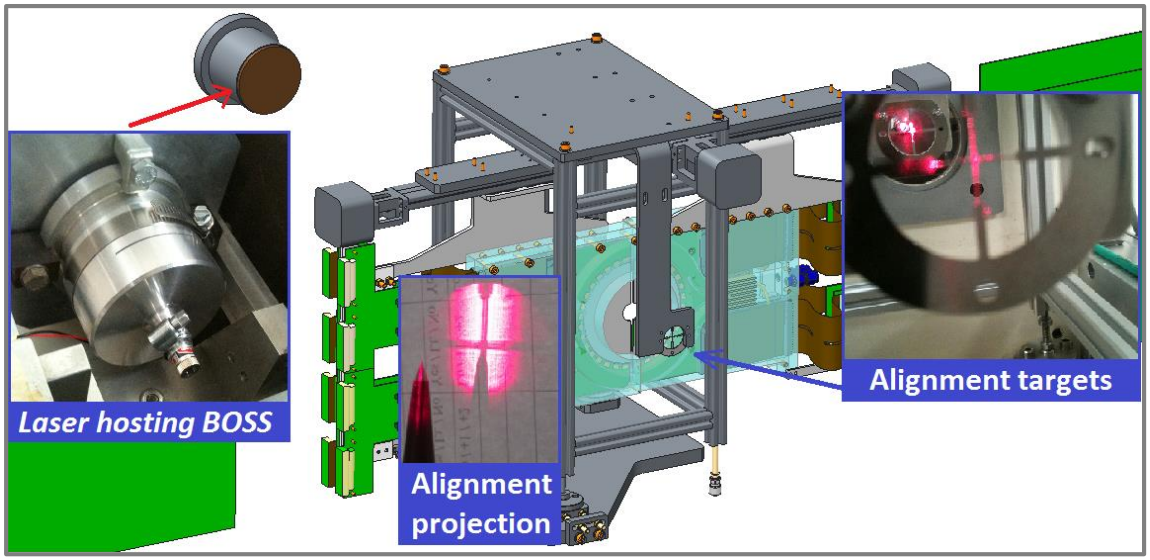

Figure 46: The alignment of the VELO detector with the beam axis.

The laser beam was shone along the beam propagation direction to the treatment iso-centre on the other side of the treatment box. The iso-centre was marked with a pin pointer mounted on the treatment chair. The laser beam was defocused to allow projecting shadows of both the vertical and horizontal arms of the crosses on a screen placed behind the pin. The longitudinal levelling was achieved by matching the horizontal arms of both targets with the iso-centre pin. To enhance matching along the z axis only one cross, proximal to the treatment box, was used

in conjunction with a thin copper wire, $\phi \approx 100\ \mu m$, attached to one of the shrouds, where both detectors were brought to $x = 0.0\ cm$ (figure 66). The wire simulated the edge of the shroud, which was removed to create the semi-circular opening for the sensor. Alignment was achieved when the copper wire shadow was matched with the vertical arm of the cross at every available position in the *z* axis (figure 46).

4.3.4 Electronics integration

The layout of the readout electronics for the VELO detector in the experiment was simplified for the purpose of the non-invasive beam current monitor prototype (figure 47). A detailed description of the original set up can be found in reference [69] and references therein. Modifications were introduced to a number of components followed by disabling of a few interlocks to support operation of the detector outside CERN environment:

1. The Experiment Control System card on the repeater board was permanently removed and the functionality of the card was reinstated by short-circuiting some of the connections. Additional modifications were introduced to the functions of the on-board chips.
2. The trigger signals from the beam supervisor were replaced with signals coming from EDA-00978-V1 trigger adapter implemented as a small mezzanine card on TELL1. There were 4 adapters used in the experimental set up, one on each of the TELL1s.
3. The temperature interlock was inactivated and temperature was monitored by four Lascar EMT 1900 LCD thermometers.
4. Both the low and high voltage interlocks were removed.

Table 11. Specification summary of the EHS 82 05P-F-XXX source-measurement unit at the maximum load. [34]

Positive channels per module	4	Ripple and noise [mV_{P-P}]	5.0
Negative channels per module	4	Stability (no load/load) [V]	0.05
Nominal output voltage [V]	500.0	Accuracy of voltage measurement [mV]	150.0
Nominal current output [mA]	10.0	Accuracy of current measurement [µA]	12.0
Voltage setting resolution [mV]	1.0	Min. voltage ramp up /down [V/s]	$5 \cdot 10^{-4}$
Current setting resolution [nA]	30.0	Max. voltage ramp up/ down [V/s]	$1 \cdot 10^{2}$

5. The $60\ m$ long CAT6 signal cables between the repeater board and the TELL1 cards were replaced by shorter, 10 m long cables assembled at STFC. A new set of input parameters to account for the length of the cables had been determined.
6. Long Kapton cables were redundant for this application. Instead 40 cm ribbon cables were introduced to build flexible connection between the stationary repeater cards and the VELO detector allowing the movement in x and z direction.

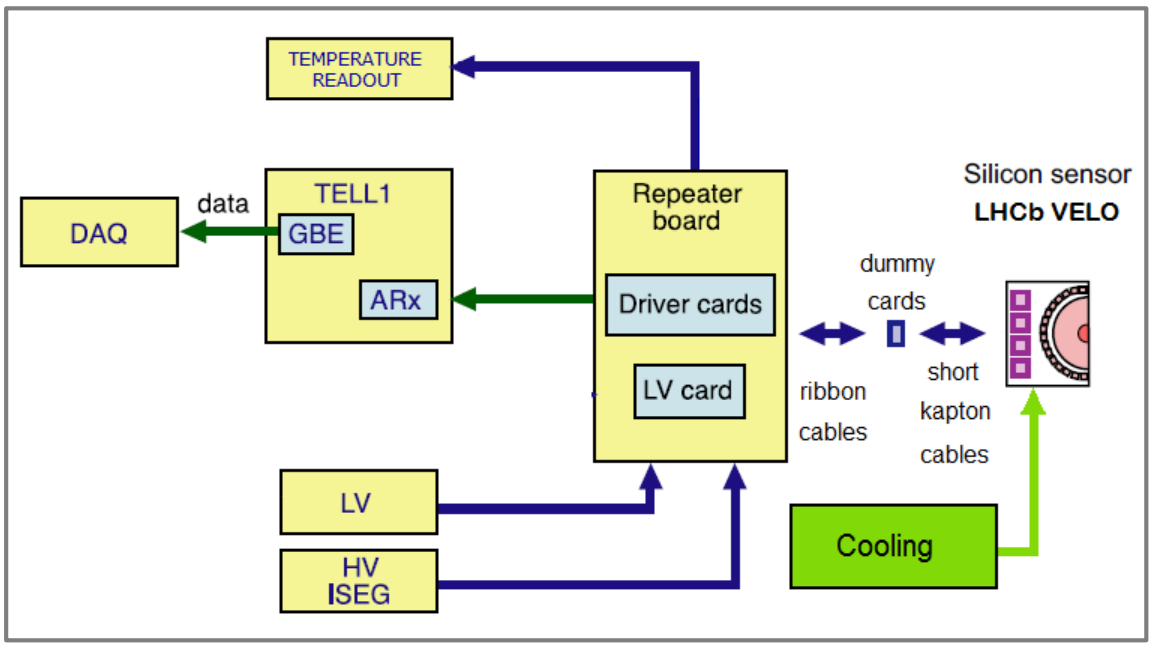

Figure 47. Layout of the modified electronics of the VELO detector. Many interlocks have been removed from the original design for operation at CERN, see reference [69].

A floating ground high voltage source-measurement unit (SMU) type EHS 82 05P-F-XXX by ISEG was used to supply the bias voltage between -500 V and 500 V. The SMU had been equipped with eight channels in total: four with positive and four with negative polarity. Thus, it can be used in measurements involving both available VELO sensor types, namely $\mathrm{n}^{+}-\mathrm{in}-\mathrm{n}$ and $\mathrm{p}^{+}-\mathrm{in}-\mathrm{n}$. The supplied voltage had stability defined by the ripple $\mathrm{V}_{\mathrm{source\ ripple}} = 5.0\ \mathrm{mV}_{\mathrm{P-P}}$ at the maximum load. The accuracy of the measuring unit and the SMU specification are summarised in table 11.

The low voltage cards on the repeater boards were powered by two commercially available bench-top power supplies: ISO-TECH 2023 $(\mathrm{U} = +/-6\ \mathrm{V})$ and DIGIMESS SM5020 powering the Beetle Chips, $(\mathrm{U} = 4.5\ \mathrm{V}, \mathrm{I} \approx 13\ \mathrm{A})$.

Chapter Summary

This chapter gave an insight to the design of the VELO detector outlining properties of the system architecture fundamental for the proposed stand alone, non-invasive method for the proton beam intensity measurements. A summary of the necessary modifications was introduced for effective integration of the detector with the treatment line at CCC, focusing on the operation of the detector without vacuum. Essential adjustments to the readout electronics were also made known supporting operation without various systems associated with the detector at CERN. In preparation to the discussion of the experimental results of the first run of the detector at CCC, studies to the beam transport will be presented in the next chapter, emphasising the beam shape in the integration area. These will establish a base to the theoretical predictions of the detector response to assess any possible and undesired saturation effects gathered in the last chapter.

5. PROTON BEAM HALO PROPAGATION AND BEAM DYNAMICS

This chapter holds a discussion on the determination of a concise beam line model for CCC and the formation mechanism of the beam halo to be monitored in the treatment room by the proposed non-invasive method utilising the VELO detector. The extent of the halo was used to determine the proton intensity maps and study the expected signal amplitude in the following chapter.

The treatment beam line model covered the area from the beginning of the scattering foils system to the treatment iso-centre and was built and executed in FLUKA. The input parameters, constituting the beam spot size and divergence, were obtained through the beam dynamics studies carried out in collaboration with the TERA Foundation (CERN) [43] and Dr Oleg Karamyshev (Cockcroft Institute). The transverse beam dimensions were measured using a scintillating screen with varying quadrupole magnet strengths.

Before summarising the beam halo modelling results in the detector integration area presented at the end of this chapter, the beam emittance measurement methods will be described, with particular attention to the quadrupole variation scan, and followed by the results of the analysis of the beam dynamics in the beam line section between the accelerator and the scattering foils.

5.1 Introduction to measurements in beam dynamics

Measurements of beam transverse dimensions are an essential part of any accelerator diagnostics. Among them, there are a number based mostly on destructive methods that demand interaction with the beam. These lead to the degradation of beam properties, e.g. affecting the space the beam occupies expressed as emittance or lead to the degradation of energy and energy spread. As in the case of the FC, the undesired effects of the interaction with the beam are of a less concern when measurements take place on machines with a single pass of particles, for instance on low energy beam transport sections of injectors or LINACs. Otherwise, the time of interaction with the beam and associated effects have to be reduced to a reasonable minimum required by the method, especially when measuring on synchrotrons or storage rings. There are a number of techniques available to assess the characteristics of the beam examining their profiles, which employ a variety of physical phenomena:

- Synchrotron light emission;
- Ionisation;
- Secondary particles emission;
- Optical photons emission (luminescence and optical transition radiation).

The above were organized to follow a scale of degradation introduced to the beam, where the synchrotron light emission is the least destructive, as no interference with the beam takes place at any point, and the most interceptive optical photons emission. There are certain limitations associated with these techniques that depend on either the investigated energy, beam intensity, complexity of the method or space required for integration.

Synchrotron radiation monitors do not interact with the beam as they emission of either optical or X-ray photons by charged particles when undergoing acceleration, for instance when their trajectory is bent by a dipole magnet. [44] For electrons the power of emitted radiation is expressed by equation (48). [17]

$$P_s = \frac{c \cdot e^2}{6 \cdot \pi \cdot \varepsilon_0 \cdot (m_0 \cdot c^2)^2} \cdot \left[\frac{dp}{dt}\right]^2 \tag{48}$$

The term $\mathrm{dp/dt}$ denotes the momentum change of the particle. This detection method is mostly used for electrons, however, it has been recently applied to measure light produced by protons of TeV energies at CERN. Further details can be found in reference [45].

Monitors that make use of ionisation comprise of two types, which depend on the level of beam interception. The first and least interceptive group is favoured to be implemented on storage rings or high intensity accelerators, for example gas jet curtains or residual gas monitors. In this case, the destructive monitors would either unacceptably disturb the beam or suffer irreversible damages. Their principles of operation rely on the ionisation of gas that either resides in the beam pipe or is injected across the chamber at very high velocities, including the ultrasonic range. The produced signal can be in a form of electrical current of either ions or electrons or emitted optical photons. Direct electrical current readout for gas jets curtains is implemented using either electrodes or multi-channel plate amplifiers. Ultimately, ionisation of residual gas, especially when higher concentrations of nitrogen are involved, may lead to excitation of the inner electron shells of atoms. Their relaxation manifests in emission of the visible electromagnetic waves, which can be collected by optical readout systems matched with

the wavelength of the emitted radiation. The last type of detectors in the group using ionisation methods are multi-wire proportional chambers. Their application leads to a more pronounced beam emittance blow-up [57] because of their construction, where they are permanently filled with gas enclosed between the walls of the detector.

The secondary emission of particles constitutes a base for the beam profiling methods using wire scanners or secondary emission girds as a source of electric current [17] [44]. The wires can be made of either light or heavy metals, typically a few tens to hundreds of μm in diameter, for instance made of an alloy of $W - Re$ for high intensity beams. The choice of material and adjustment of the diameter depend on the investigated size and intensity of the beam. The wire is swept across the beam at speed adjusted to the requirements of the machine. To minimize the interaction effects, very fast moving wires are a good choice for circular machines (storage rings) to minimise effects they have on the emittance. [44]

The optical transition detectors and scintillating screens constitute the last group that uses emission of optical radiation. Each of them however has got different emission mechanisms:

- Optical transition detectors use time-dependent polarisation of the detector material induced by the electromagnetic field of an approaching particle. Relaxation of the induced charge leads to emission of visible light. [17]
- Scintillating screens operate on luminescence induced in the crystal lattice. When a charged particle passes through a detector, part of the kinetic energy is transferred leading to ionisation and production of excited states of atoms. Their de-excitation manifests in emission of optical photons and the crystal returns to the base energy state.

The luminescence centres in the scintillating crystals are located around impurities introduced in a form of activator atoms. The performance characteristics of this type of detectors are required to have:

- Highly linear emission of light as a function of the beam intensity to exclude any saturation that would lead to incorrect beam profile determination;
- No or minimal absorption or straggling of the emitted light to avoid any stray radiation;

- High radiation hardness to provide long lasting operation without degradation of properties.

For the best performance results, the emission spectra need to be matched with the sensitivity of the optical readout system.

The described detectors, especially scintillating screens, are widely used in beam emittance measurements to calculate the beam Twiss parameters. [46][47] They are frequently incorporated in various complex detection methods, like slit beam scanners and pepper pots, or in quadrupole variation scans (QVS). The latter was used in emittance studies performed at CCC in collaboration with Dr Alberto Degiovanni (TERA Foundation, CERN) and Dr Oleg Karamyshev (QUASAR Group, Cockcroft Institute), where the aims of the investigation were set to find:

- Beam Twiss parameters at the extraction from the cyclotron to assess suitability of the CCC cyclotron as an injector for a LINAC booster by TERA;
- Preliminary model of the beam line for future projects at QUASAR Group;
- Transverse beam dimensions at the position of the scattering foils system, which were used as input parameters for the model of the proton transport through the treatment beam line. As a result, beam halo maps in the VELO detector integration region in FLUKA were found to quantify the response of the detector and to address any possible saturation effects.

The QVS described in the following paragraph were implemented using a $\mathrm{CsI(Tl)}$ scintillator disc coupled with a digital CCD camera. They were integrated with the beam line at two independent measurement locations, one in the vault of the accelerator and the other in the treatment room.

5.2 Beam transport and quadrupole variation scans at CCC

Beam transport of particles in a beam line can be expressed in linear transport formalism. [46] A set of particles can be described in a phase-space, where their distribution is contained in an ellipse, figure 48. Assuming there are no correlations between the transverse and horizontal directions of particle motion, their distributions can be expressed in a form of a matrix:

$$\sigma = \begin{pmatrix} \sigma_{11} & \sigma_{12} \\ \sigma_{21} & \sigma_{22} \end{pmatrix} = \begin{pmatrix} \langle x^2 \rangle & \langle xx' \rangle \\ \langle xx' \rangle & \langle x'^2 \rangle \end{pmatrix} = \epsilon^2 \cdot \begin{pmatrix} \beta & -\alpha \\ -\alpha & \gamma \end{pmatrix} \quad (49)$$

Where:

α, β, γ - Parameters of the ellipse enclosing the distribution of particles:

$$\gamma \cdot x^2 + 2\alpha \cdot x \cdot x' + \beta \cdot x'^2 = \varepsilon \tag{50}$$

$$\alpha = \frac{\sigma_{12}}{\varepsilon} \tag{51}$$

$$\beta = \frac{\sigma_{11}}{\varepsilon} \tag{52}$$

$$\gamma = \frac{\sigma_{22}}{\varepsilon} \tag{53}$$

ε - Emittance of the beam equal to the area of the ellipse;

$\langle x^2 \rangle$ - Second order moment of particles coordinate (beam width);

$\langle x'^2 \rangle$ - Second order moment of particles divergence;

$\langle xx' \rangle$ - Correlation between the coordinate and divergence of the particles.

The elements on the right side of equation (49) are called Twiss parameters of the beam. The two dimensional area of the phase-space ellipse can be found following the formula:

$$\pi\epsilon = \pi \cdot \sqrt{\det \sigma} = \pi \cdot \sqrt{\sigma_{11} \cdot \sigma_{22} - \sigma_{12}^2} \tag{54}$$

The beam parameters can be propagated through any beam line when a transfer matrix R through the consecutive components is known. The basic elements of any transport line consist of:

- Drift space, when the divergence of the particle x' is preserved and it undergoes only a displacement in the transverse plane due to difference in location l_{drift}. The transport matrix R_{drift} is expressed by:

$$R_{drift} = \begin{pmatrix} 1 & l_{drift} \\ 0 & 1 \end{pmatrix} \tag{55}$$

- Quadrupole magnets that have effect on the beam by focusing it the horizontal plane and defocusing in the vertical direction at the same time throughout the

length of the magnet l_q, or exactly the opposite. The transformation matrices R_F and R_D are expressed respectively by:

$$R_F = \begin{pmatrix} \cos(l_q \cdot \sqrt{k}) & \frac{1}{\sqrt{k}} \cdot \sin l_q \cdot \sqrt{k} \\ -\sqrt{k} \cdot \sin l_q \cdot \sqrt{k} & \cos l_q \cdot \sqrt{k} \end{pmatrix} \quad (56)$$

$$R_D = \begin{pmatrix} \cosh l_q \cdot \sqrt{k} & \frac{1}{\sqrt{k}} \cdot \sinh l_q \cdot \sqrt{k} \\ \sqrt{k} \cdot \sinh l_q \cdot \sqrt{k} & \cosh l_q \cdot \sqrt{k} \end{pmatrix} \quad (57)$$

where:

k - Quadrupole magnet strength defined by the quadrupole gradient G, the particle momentum p and the charge of the particle, q:

$$k = q \cdot \frac{G}{p} \quad (58)$$

As a result, any known set of beam parameters σ_i can be transported through a beam line optical system producing a set of Twiss parameters at the new location, using a generalized transfer matrix R and a matrix transposed to it R^T, following the equation:

$$\sigma = R\sigma_i R^T \quad (59)$$

The above apparatus can also be used to find the initial Twiss parameters of a given beam at the entrance to the quadrupole by varying the strength of the magnets. Depending on the strength, the beam changes the transverse dimensions x_i. The measurement normally takes place at a distance l form the exit of the quadrupole, characterised by a simple drift transformation matrix for the beam (55). In this way a system of linear equations is created with one equation for every quadrupole strength k (60).

$$x_{1,k}^2 = \sigma_{11}(k) = R_{11}^2(k) \cdot \sigma_{i11} + 2R_{11}(k)R_{12}(k) \cdot \sigma_{i12} + R_{12}^2(k) \cdot \sigma_{i22} \quad (60)$$

A solution has to be found for a set of redundant linear equations using either a least square fit to the best parameters of $\sigma_{ij}(0)$ or by solving the regression problem via so called normal equations. A solution vector is produced, equation (61) and the emittance $\epsilon_{\sigma(0)}$ can be obtained according to the equation (62).

$$\sigma(0) = \begin{pmatrix} \sigma_{11}(0) \\ \sigma_{12}(0) \\ \sigma_{13}(0) \end{pmatrix} \quad (61)$$

$$\epsilon_{\sigma(0)} = \sqrt{\sigma_{11}(0) \cdot \sigma_{22}(0) - \sigma_{12}{}^2(0)} \tag{62}$$

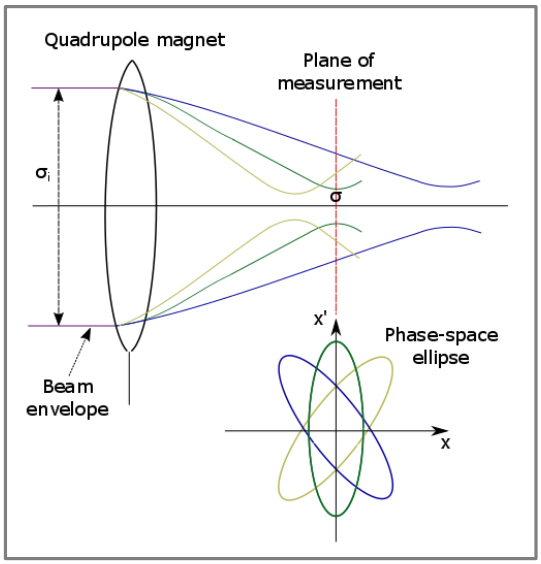

Figure 48: The principles of quadrupole variation scan method for Twiss parameters transport.

Down to the fact that in normal conditions the measurement is performed at location l from the quadrupole magnet, the transformation matrix can be simplified using a thin lens approximation. [17][24] The transfer matrices reduce for both the focusing F and defocusing direction D producing the total transfer matrix (65):

$$R_F = \begin{pmatrix} 1 & 0 \\ -\frac{1}{f} & 1 \end{pmatrix} = \begin{pmatrix} 1 & 0 \\ -K & 1 \end{pmatrix} \tag{63}$$

$$R_D = \begin{pmatrix} 1 & 0 \\ \frac{1}{f} & 1 \end{pmatrix} = \begin{pmatrix} 1 & 0 \\ K & 1 \end{pmatrix} \tag{64}$$

$$R = R_{drift} \cdot R_{focusing} = \begin{pmatrix} 1 + lK & l \\ K & 1 \end{pmatrix} \tag{65}$$

With regard to [16], it can be shown that for the measured beam width combined with the above transfer matrix follow a quadratic formula:

$$\sigma_{11} = l^2 \cdot \sigma_{i\,11}(0) \cdot K^2 + 2\big(\sigma_{11}(0) + l^2 \cdot \sigma_{12}(0)\big) \cdot K + \sigma_{11}(0) + 2l \cdot \sigma_{12}(0) + l^2 \cdot \sigma_{22}(0) \tag{66}$$

Therefore, a parabolic fit to the beam size with regard to the quadrupole strength for the fit parameters a, b and c shows that the equations (67) and (66) are similar, and by equating them the consecutive parameters can be obtained accordingly:

$$\sigma_{11}(K) = a \cdot K^2 - 2ab \cdot K + ab^2 + c \tag{67}$$

$$\sigma_{11}(0) = \frac{a}{l^2} \tag{68}$$

$$\sigma_{12}(0) = -\frac{a}{l^2}\left(\frac{1}{l} + b\right) \tag{69}$$

$$\sigma_{22}(0) = \frac{1}{l^2}\left(ab^2 + c + \frac{2ab}{l} + \frac{a}{l^2}\right) \tag{70}$$

Ultimately the emittance of the beam is given by:

$$\epsilon_{\sigma(0)} = \sqrt{\sigma_{11}(0) \cdot \sigma_{22}(0) - {\sigma_{12}}^2(0)} = \frac{\sqrt{ac}}{l^2} \tag{71}$$

5.2.1 Measurements

With regard to chapter 2, the $60\ \mathrm{MeV}$ proton beam is delivered to the treatment room through two straight beam line sections. There are three quadrupole triplets separated by a switching magnet in-between the first and the second triplet, where the beam is diverted by approximately 5 degrees. Parts of the beam line had to be removed to permit integration of the measurement chamber with the existing set-up. There were two measurement locations envisaged in the experiment (figure 49):

- In the vault of the accelerator: at the exit from the first quadrupole triplet Q1 - in place of the collimator BC1;
- In the treatment room past the third quadrupole triplet Q3 and the XY steering magnet XY4 – replacing the flip screen FS3.

The experimental set up consisted of a $\mathrm{CsI(Tl)}$ scintillating disc mounted on a dedicated arm, designed by TERA Foundation at CERN, which was tilted at an angle $\alpha = 45°$ with respect to the beam direction, where the 1:1 aspect ratio between the beam size and the image of the beam registered by the camera was preserved. Two orthogonal laser beams, parallel to the vertical and horizontal axes of the beam, were used to align the scintillating screen to the centres of the vacuum vessel flanges. In this manner, the disc was positioned co-centrically with the expected beam axis in the beam line (figure 50). The prompt fluorescence light emitted from the screen was fed outside via a glass windowed flange positioned centrically on the top of the cross. Detection and digitisation of the signal was performed with an 8 bit-depth, 1.3 Mega pixel u Eye U-1540-M-GL camera. The housing vessel was connected to the vacuum system of the

accelerator with a KF-CF reducer and pumped down to exclude any possible proton scattering from the residual gas molecules (figure 50).

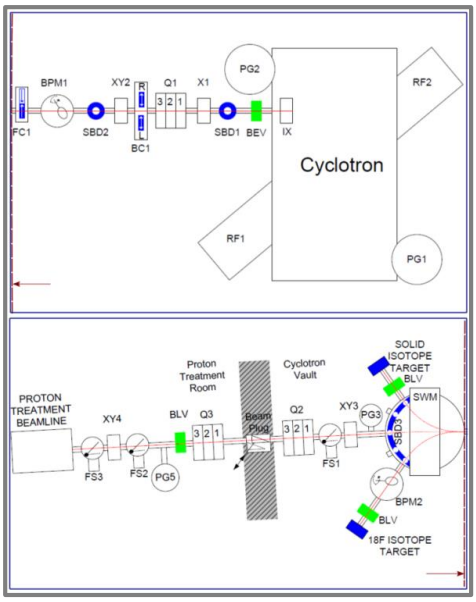

Figure 49: Lay out of the beam line at CCC presenting the quadrupole variation scans integration regions: BC1 and FS3. The dashed line is the stitching place of the two parts of the beam line.

Collateral beam intensity measurements, using a Faraday Cup fitted in place of the screen proved that no beam losses due to the incorrect set up of the quadrupole magnets between the vault and the treatment room had place. The measured beam current value was $I = 3.12\ nA$ at both the measurement locations and the beam images were fully contained within area of the scintillator (figure 51).

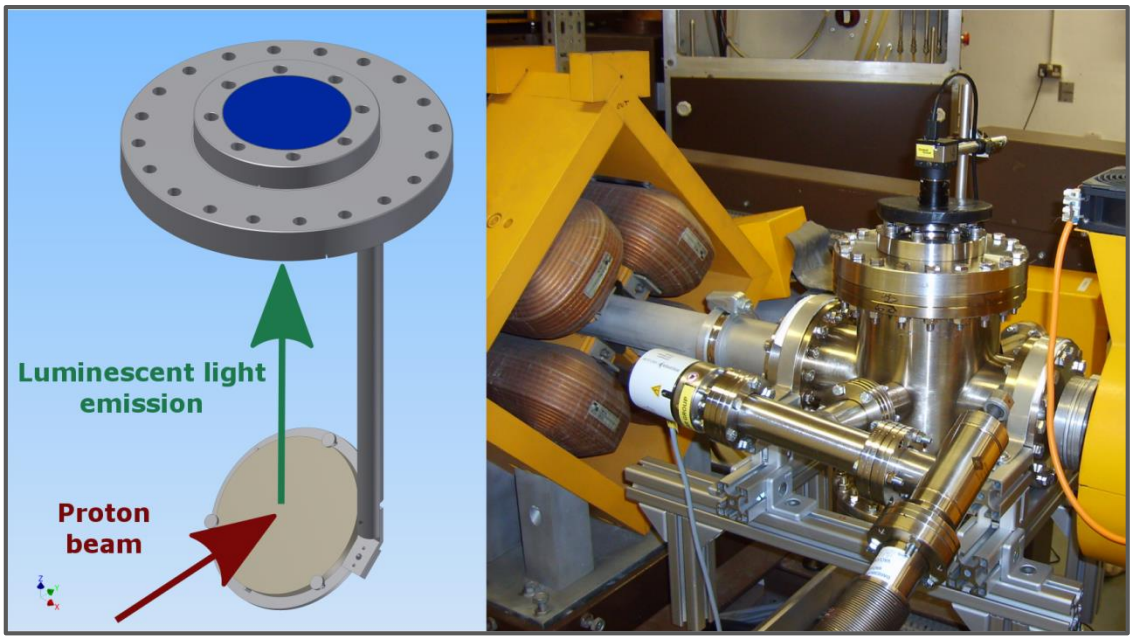

Figure 50: The quadrupole variation scans experimental chamber. The scintillating screen was fixed in the middle of the chamber on the beam axis. The emitted light was fed outside through a windowed flange at the top and was collected by a CCD camera aligned with the centre of the screen.

5.2.2 Data analysis

Transverse beam dimensions for both test locations were obtained varying the strengths of the consecutive lenses in the quadrupole triplets by adjusting their electric current values. The measurements were completed for lenses:

- L2 (proximal to the cyclotron) and L3 (proximal to the treatment room) in the quadrupole triplet Q1;
- L3 in the quadrupole triplet Q3, figure 49.

A summary of the varied current values can be found in table 12. A closer investigation of the captured images shows that the beam has a trailing tail in the horizontal direction, on the side of the inner orbits in the accelerator, noticeable as a smear towards the bottom of the image in figure 51. Increasing focusing strength in the horizontal direction had an immediate effect on the tail shifting it to the other side of the vertical beam axis. This is believed to be associated with the extraction of bunches from the cyclotron, when a few lower energy internal orbits are partially extracted together with the last orbit. Non-uniformities in the vertical plane, horizontal axis in figure 51, originate from the CCD camera - screen geometry because of the optical lenses between them. Here, the tilt introduced to the screen affects the light collection efficiency due to their different path lengths depending on the emission point in the scintillator. Emission into

different stereo angles changes the ratio between the physical distances on the screen per pixel in the camera. Therefore, the distances in the vertical direction were calibrated against a reference image with a scale of evenly spaced bars every d_{bars} = 10 mm.

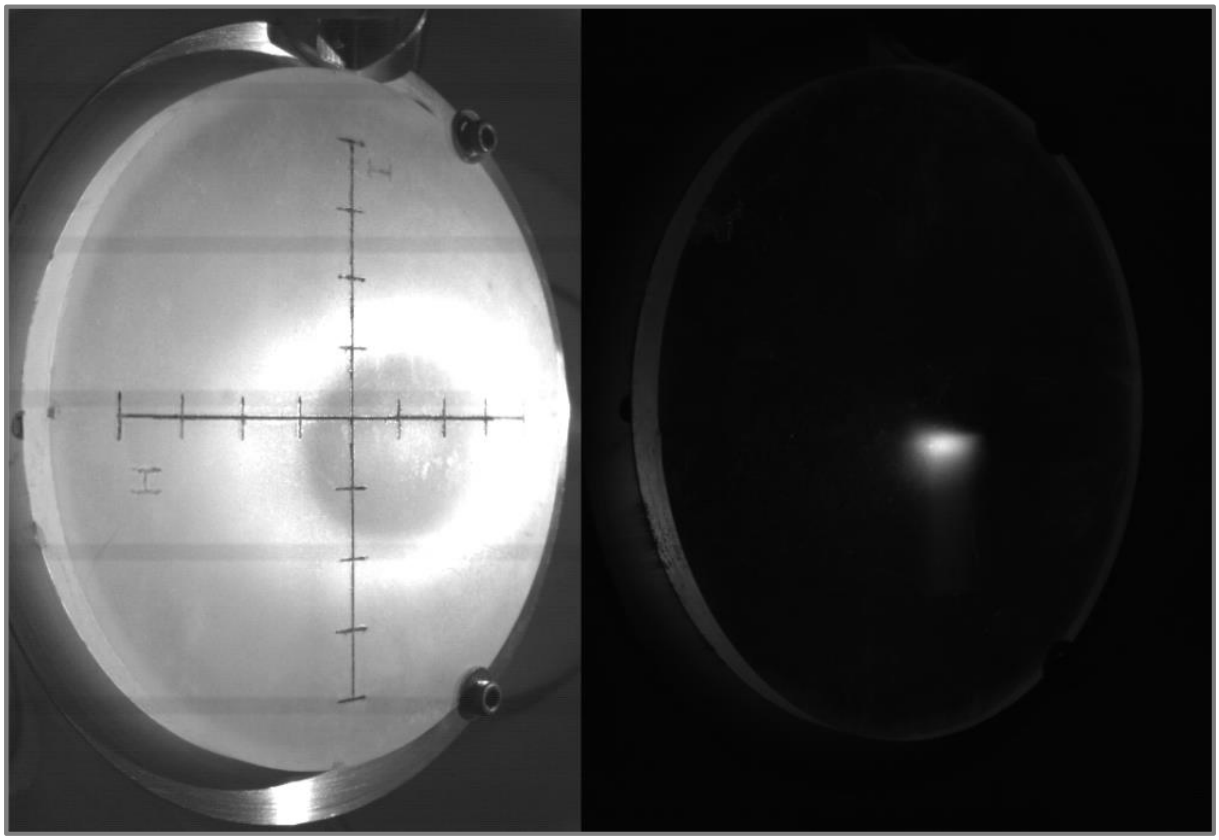

Figure 51: Images of the reference image for pixel – to – distance calibration on the left and beam spot size on the right, both obtained during the quadrupole variation scans at CCC.

Table 12: QVS used magnet currents range.

Element	Current [A]	
	Quadrupole 1	Quadrupole 2
L1	19	13
L2	-20 to 40	37
L3	-26.7 to 30	22.9 to 32.6

The pixel number-to-position relation in the horizontal direction was described by a first order polynomial, equation (72):

$$p_H = 0.0171 \cdot x + 0.7638\ cm/pixel \quad (72)$$

A higher order polynomial was fitted to the calibration data in the vertical direction and was expressed by equation (73):

$$p_V = 3.4540 \cdot 10^{-8} \cdot x^3 - 1.9818 \cdot 10^{-6} \cdot x^2 + 0.0192 \cdot x + 0.0798\, cm/pixel \qquad (73)$$

Results of both are graphically presented in figure 52.

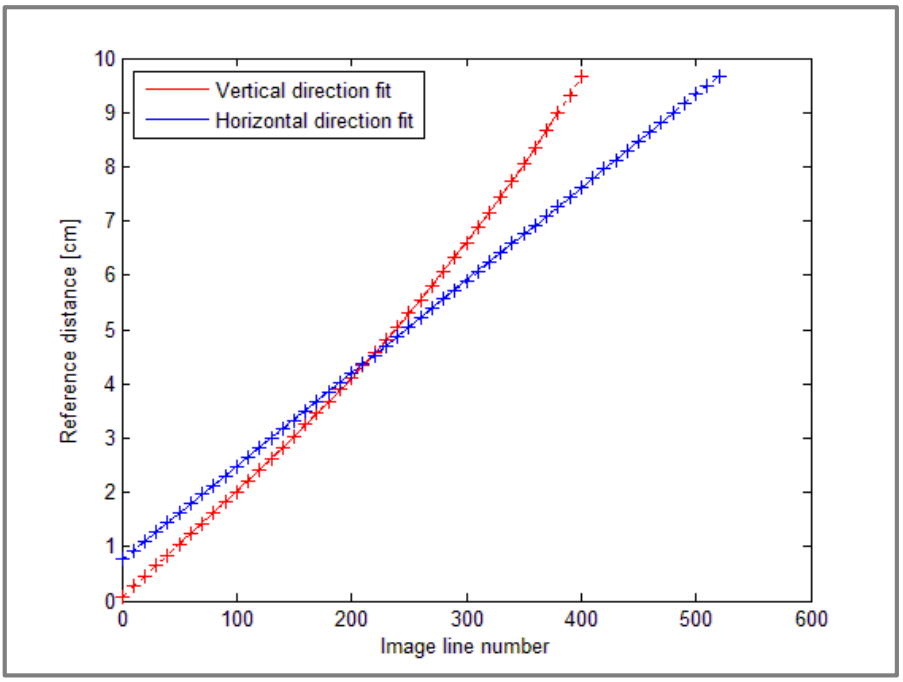

Figure 52: Calibration curves for pixel number-to-real distance relation for the captured images.

The pixel to distance conversion for every profile, together with image post-processing and further fitting with Gaussian curves, was automated in a purpose-written MATLAB script. The integration of the background signal, in the areas outside the beam, was used to correct the obtained profiles for the ambient brightness that influenced the measurement sensitivity. Distortions to the images, due to noise induced in the active elements of the camera or originating from the non-uniformities of the scintillating screen, were corrected for in MATLAB applying a built-in *smoothn()* function [53] similar to a moving average filter. An arbitrary area of interest was chosen to exclude profiling outside the region of the scintillating screen, namely areas containing glares at the edge of the screen. Thus, the local maxima other than the beam image, which could introduce errors to the algorithms, were suppressed.

The extraction tail, mentioned previously, adds to the Gaussian image of the bunch distorting the image. Limited information about the beam line optical components, especially

gradients of the magnets, did not allow for precise modelling of its evolution through the length of the beam line to fully exclude it from the analysis in the treatment room. There, it becomes strongly pronounced because of the switching magnet between the two sections of the beam line, where the particles are separated depending on their energy giving raise to their different bending radii. Therefore, three different methods were tested for that set of data to discover the most reliable algorithm for determining the beam sizes in both directions: single Gaussian, FWHM and double Gaussian. A comparison between the calculated sizes is presented in figure 53. The FWHM and single Gaussian method exposed that their results are in agreement. The double Gaussian fit is more precise in determination of the beam waist by approximately 10 % with respect to the other methods. As depicted below, the magnitude of the tail region constitutes approximately 50 % of the main peak and the single Gaussian fit is insufficient to represent the bunch profile (figure 53). Therefore, both the FWHM and single Gaussian fits were overestimating the beam sizes for the smallest beam dimensions by integrating those two components. A double Gaussian fit to the data had to be used in the analysis in the treatment room incorporating an assumption that, due to the linearity of response of the scintillating screen with the beam intensity, the area of the peak representing the tail, found for the widest separation from the main bunch, was constant. Consequently, the beam sizes in the waist region decreased becoming more parabolic than for the two previous fitting functions, and were in agreement with the theory. The double Gaussian fit, however, treats the tail only perfunctorily as the full understanding of the behaviour was not possible to be known at the time of data collection. Nevertheless, in normal operation of the accelerator the intensity of the tail is decreased due to absorption in an actuated collimator located in the vault, which was removed in order to accommodate the experimental vessel. For the scope of this investigation, the tail region did not require any in-depth modelling.

The single Gaussian fit, excluding the analysis in the tail region, was sufficient to find the initial beam Twiss parameters at the extraction from the accelerator in the vault, as there the tail region is not influencing the beam shape to such a significant extent. A rough estimation of the beam size in the treatment room was sufficient for the described purpose of investigation.

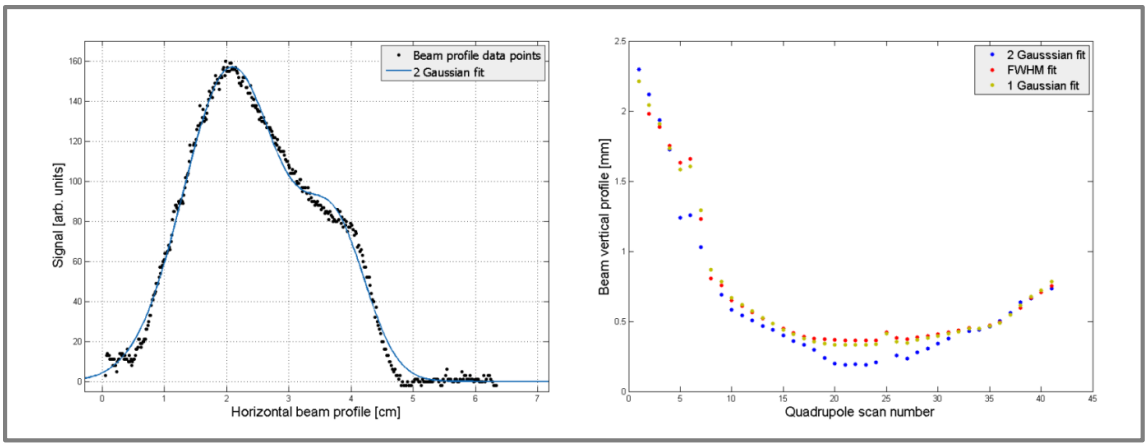

Figure 53; Horizontal beam spot profile showing two beam components fitted with a double Gaussian curve.

The model of the beam line and proton transport presented below was created by Dr O. Karamyshev (QUASAR Group) at the Cockcroft Institute. Different quadrupole focusing strengths provided a set of redundant differential equations that were solved in MATLAB to find the initial set to Twiss parameters satisfying equations (table 13).

Table 13: Results of the QVS scan in the treatment room and the beam spot size at the entrance to the scattering foils system as an input to FLUKA simulations.

	Extraction from the cyclotron			Entrance to the scattering foils system	
	Twiss parameters		$\epsilon\ [mm\ rad]$		
	α	$\beta\ [m]$		$\beta\ [m]$	FWHM [mm]
Horizontal	0.86	1.9897	5.0	2.6	4.4
Vertical	0.2685	1.0629	1.0	8.8	3.2

The beam Twiss parameters at the extraction point from the cyclotron were benchmarked against the measured profiles by transporting them back to the measurement point and comparing with the experimental results (the solid line behaviour in figure 54). There is a considerable discrepancy in the results for the four points corresponding to the current values between 18 and 24 amperes in the vertical direction. Careful study of the images in this region revealed a step like change in the beam dimensions. Should more detailed studies of the beam dynamics be undertaken in the future, the results obtained here provide a clear indication as to where research ought to be focused; excluding unknowns that were associated with the limited knowledge about the beam line.

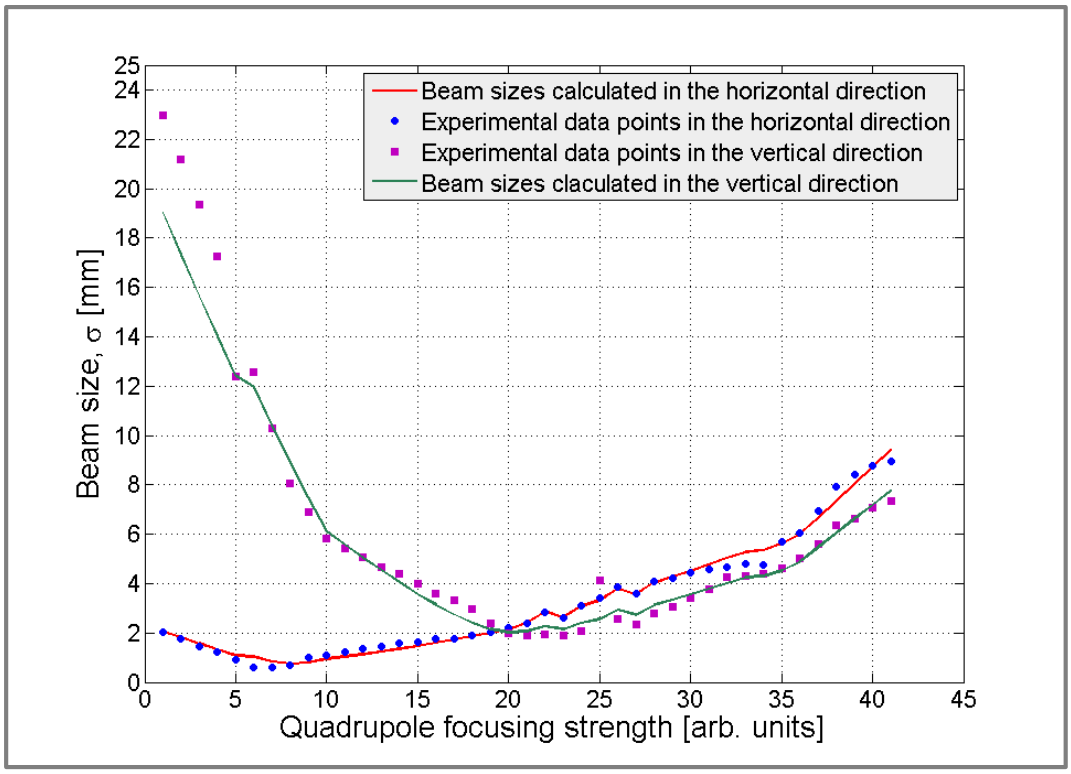

Figure 54: Comparison between the experimentally obtained beam sizes and beam sizes calculated by transporting beam Twiss parameters through the Q1 quadrupole triplet to the location of the experiment.

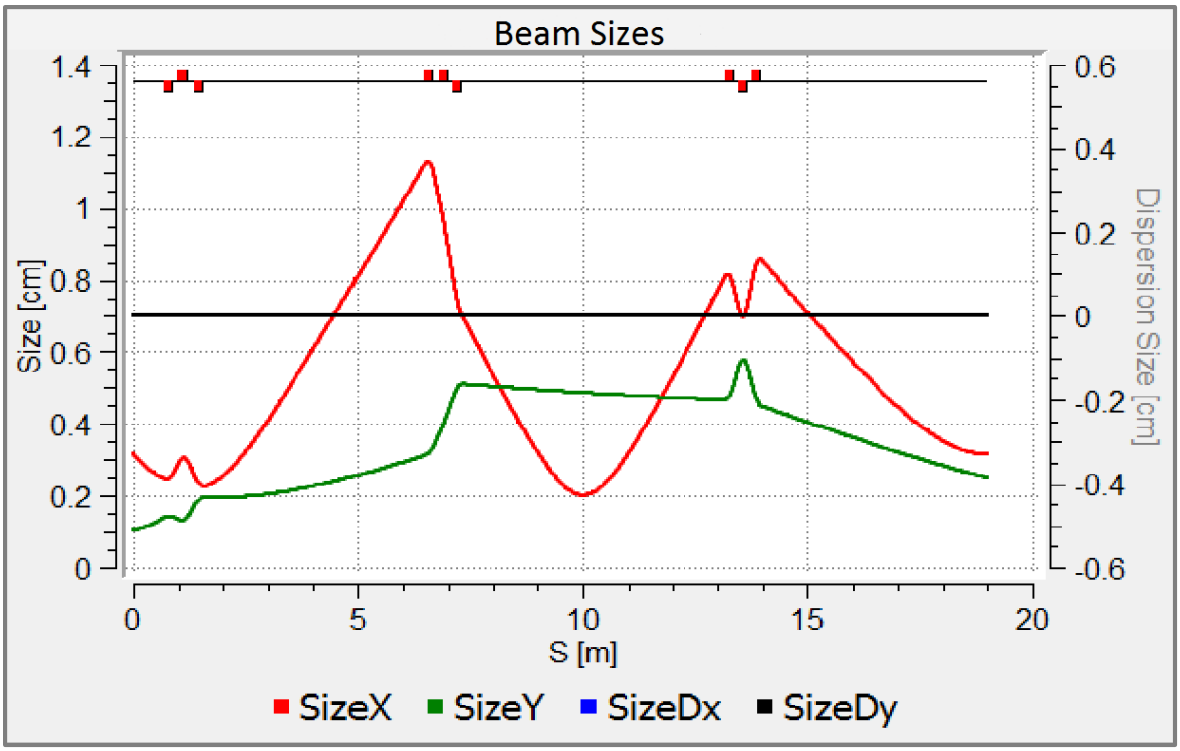

Figure 55: Caculated proton beam sizes along the transport beam line as simulated in OptiM. [61] (Courtesy of Dr O. Karamyshev)

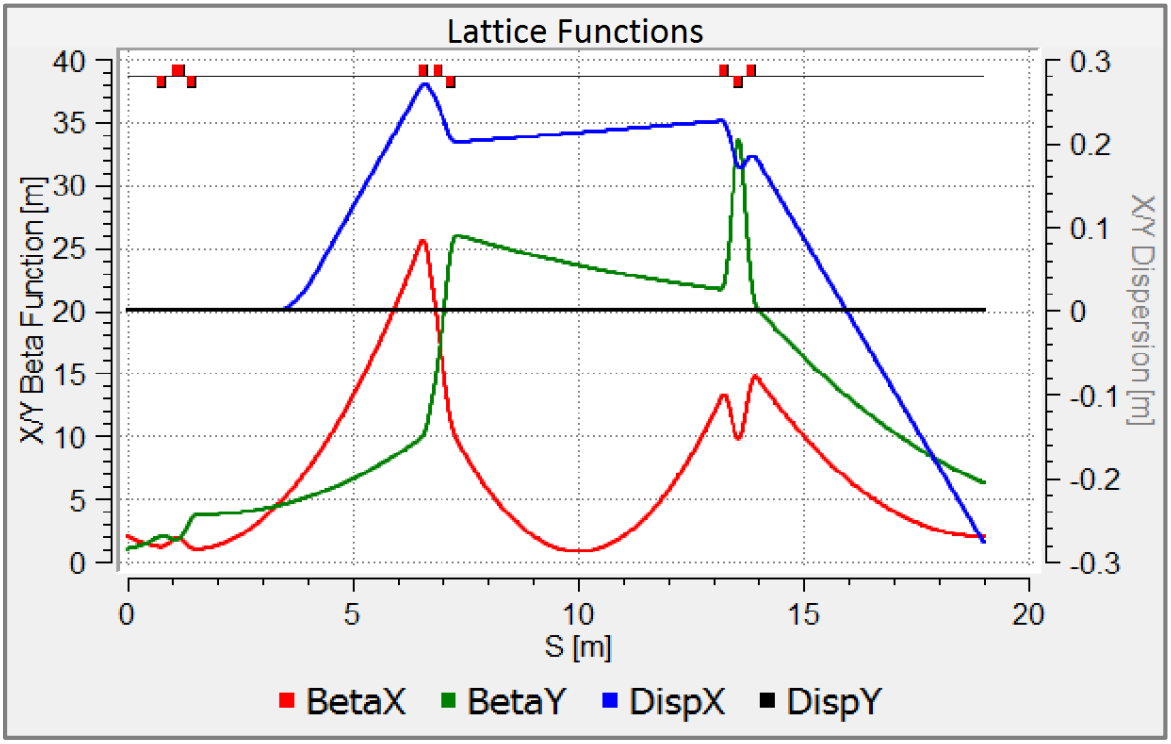

Figure 56: Calculated proton beam β functions along the transpost beam line as simulated in OptiM. [61] (Courtesy of Dr O. Karamyshev)

5.3 Simulation of proton beam shape and beam halo evolution

The treatment beam line at CCC consists of a scattering beam delivery system depicted schematically in figure 58. In principle the beam profile is spread into a Gaussian shape and only the central part of it is used in the treatment. There are four general models of scattering systems used on medical facilities, each producing different beam flatness properties:

- Single scattering foil with flat scatter, when only narrow central part of the beam passes through a collimator. Most of the beam is terminated in the collimator.
- Double scattering system with contoured scatter, when a single scattering foil is used and the collimator clearance is wide. A flattening filter is used to flatten the beam profile.
- Double scattering system with dual ring that is the solution at CCC (figure 57).
- Double scattering with occluding rings.

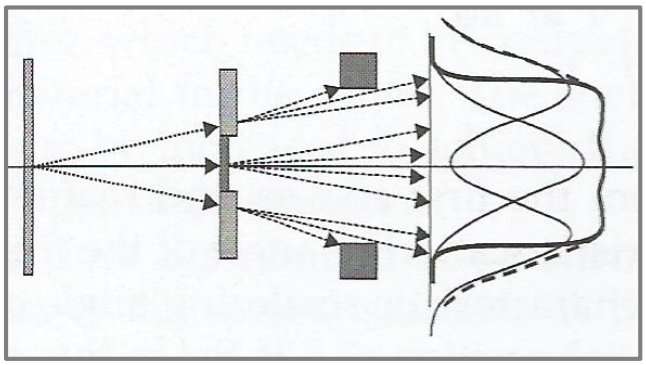

Figure 57: Double scattering foils delivery system with two rings. [5]

The double scattering system with contoured scatter has two stages of scattering. The first foil spreads the beam to pre-shape it for the second scattering foil layer. The latter normally consists of two rings, the central built with a high Z material and the external incorporating a low Z material placed around the central stopper. Normally the stopper is built of tungsten and creates Gaussian distribution of proton spectrum. The thickness of the outer ring is adjusted to create proton spectrum that adds to the Gaussian part producing a flat profile. [5]

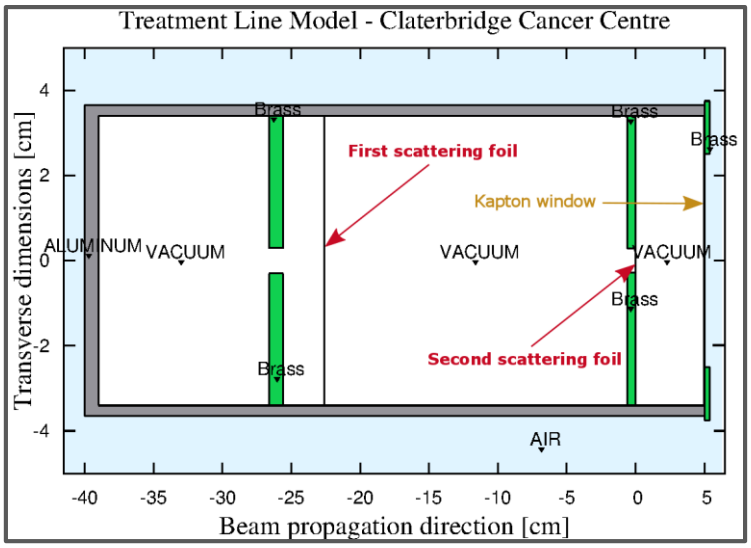

Figure 58: Model of double scattering foils system at CCC created for beam transport simulation in FLUKA.

The double ring design has been implemented at CCC with a modification, where the outer ring was made of brass. A detailed summary of the scattering foils system dimensions can be found in table 14. The beam arrives first at the brass collimator where the mentioned chromaticity of energy spectrum is removed (extracted by the switching magnet from the passing bunch). The central part of the bunch passes through the nozzle and spreads on the first scattering foil, which is $x = 25\ \mu m$ thick. Further down, the beam arrives at a second brass collimator, which hosts another tungsten scattering foil of the same thickness. The second ring is different from the described double ring design and is made of heavier metal, which terminates the proton spectrum around the central aperture (figure 58). The transverse beam shape on leaving the second scattering foils system is Gaussian with no intensity compensation from the outer ring.

Table 14: Summary of the geometrical arrangement of the scattering foils system at CCC.

Element name	Pre-collimator	1st Scattering foil	Stopper	2nd scattering foil	Vacuum window	Brass termination ring
Material	BRASS	TUNGSTEN	BRASS	TUNGSTEN	KAPTON	BRASS
Start location [cm]	-25.60	-22.60	-0.60	0.00	4.95	5.00
Thickness $[cm]$ or (μm)	[1.0]	(25.0)	[0.6]	(25.0)	(50.0)	[0.4]
Radius [cm]	0.300	3.500	0.286	0.286	3.4	Inner [2.5]

On leaving the vacuum pipe terminated with a Kapton window, the beam transport takes place in air and passes through various elements of the treatment line:

- Beam modulator box.
- Drift pipe.
- Diagnostics box.

The overall distance covered by the beam along the propagation direction equals to $\mathrm{z} = 131.0\ \mathrm{cm}$. The consecutive components of the beam line passively shape the distribution of protons around the core of the beam, especially in the VELO integration area. The scattering foils system with the Kapton window is the first stage of halo formation and gives rise to it. Further, the back plate of the modulator box determines the transverse dimensions of the halo in the integration region. This thick metal plate has got a circular opening of a diameter $\mathrm{d} = 6.8\ \mathrm{cm}$. A similar plate creates an entrance to the diagnostics box, before the parallel-late ionisation chambers. In the clinical operation both boxes are interconnected with a metal pipe absorbing the scattered protons. The third and the last plate terminates the diagnostics box on the patient side and is composed of metal hosting a brass treatment nozzle (figure 7).

A detailed model of the treatment beam line was built in FLUKA to perform studies of the proton transport and obtain the expected beam halo extent at different locations along the beam propagation direction (z) in the detector integration region. The dimensions and positions of the consecutive elements can be inspected in table 15. The term beam halo, in this particular application, is defined differently to what is understood in beam dynamics in accelerator science. This is due to the different nature of formation, namely within the accelerator science the halo results from particles that arrive at angles and distances different from the acceptance of the beam line optics. In the proposed monitoring method the raise of the halo in the integration region is purely caused by scattering of protons from the treatment line elements and air molecules.

Figure 60 illustrates an estimated proton fluence though the treatment line with an origin in the vacuum part. The input parameters were determined in the previous section, where they follow Gaussian distribution and are described by a set of properties summarized in table 13. To obtain good statistical representation of the results, Monte Carlo tracking was executed for the initial number of particles of $N = 1.0 \cdot 10^7$. The settings of FLUKA particle

transport for various physical phenomena can be examined in table 16. The FLUKA estimators were set in the beam line before the scattering foils, in the integration area and at the exit from the treatment nozzle. The VELO detector integration region could not be used in the full range of available space along the z axis because of the limitations caused by the size of the detector stand and minimum clearances from the modulator and diagnostics boxes required. As a result, the minimum distance from the exit of the modulator box to the first available position of the VELO detector was $\Delta z = 6.9\ \mathrm{cm}$. This was marked as $z_1 = 0.0\ \mathrm{cm}$ in the detector coordinate system (figure 66) and together with $z_2 = 9.0\ \mathrm{cm}$ and $z_3 = 15.0\ \mathrm{cm}$ constituted three longitudinal experimental locations. Beam profiles were extracted here for a square area of $9\ \mathrm{cm}$ by $9\ \mathrm{cm}$ divided into 361 bins in both horizontal and vertical directions resulting in the bin width of $x_{\mathrm{bin}} = 0.49\ \mathrm{mm}$. The longitudinal size was set to the thickness of the detector, that is $th_{\mathrm{VELO}} = 0.3\ \mathrm{mm}$.

The first set of estimators, situated at in the beam line before the first brass collimator, and the latter at the exit of the nozzle, was used to find the theoretical ratio between the beam current value measured by the FC at the isocentre and the initial number of particles impinging at the first scattering foil. The results of simulation showed that the expected ratio in the beam intensity between these two points shall be in the region of $R = 3.2$. As a consequence, the proportionality between the intensity of the beam halo in the integration area and actual beam intensity measured at the isocentre was determined.

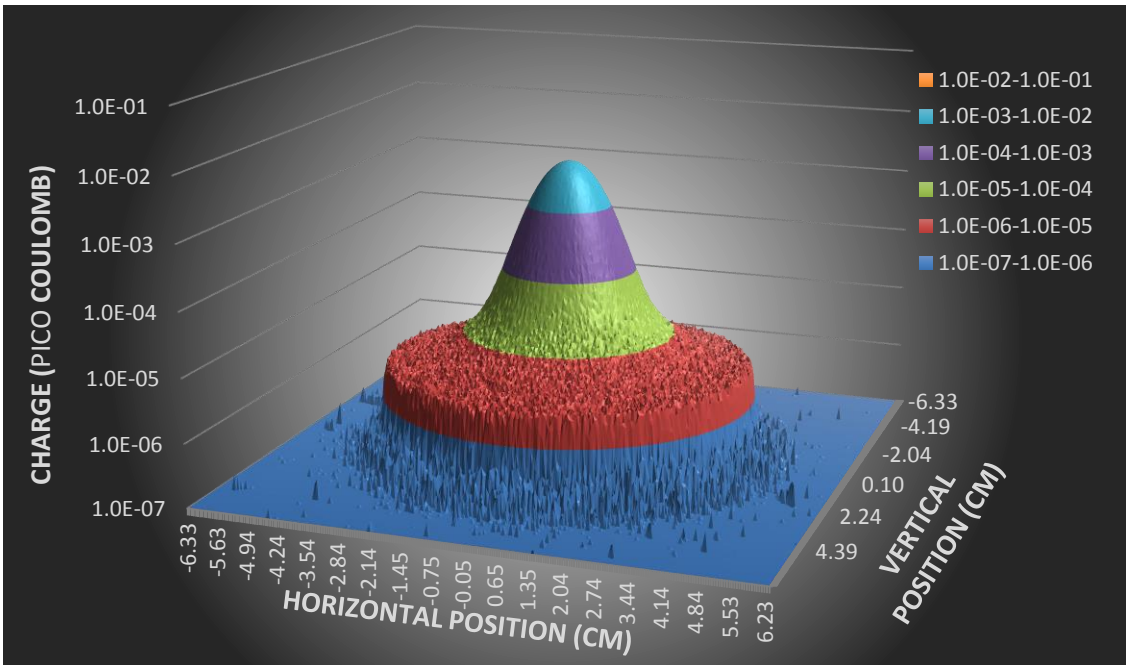

Figure 59: Transverse charge distribution of the proton beam the the location z = 0.0 cm of the LHCb VELO detector for the beam intensity in the beam line, $I_{BL} = 3.2\ nA$ corresponding to the beam intensity at the treatment isocentre $I_{ISO} = 1\ nA$.

The remaining estimators, situated in the integration area, generated proton distribution maps in a function of distance from the beam axis. The evolution of the beam shape and halo around it can be inspected in a series of figures 60 to 62. The beam shape reflects adequately on the design of the beam line elements, where three regions in the beam can be distinguished (figure 59):

- The central, which contains the core of the Gaussian part of the beam formed by the scattering foils;
- The middle formed by the Gaussian edge of the distribution until the sharp fall-off marked by a circular rim as a result of the aperture of the modulator box representing the first halo region;
- The outer, defined beyond the rim where only very few protons can be found based on the calculated distribution probabilities.

The halo has a continuous symmetrical intensity distribution falling down with an increasing distance from the central axis. The probability distributions were normalized to $\text{particles} / \text{cm}^2 / \text{primary}$, which meant that the expected intensities of the proton maps are a linear function of the beam current. The low values of the beam current, being fractions of

nano-amperes, did not have to involve considerations of the space charge effects as it comes about for high intensity beams accelerators with currents of the order of mA.

Table 15: Table 4: CCC beam line dimensions of constituent elements used for proton transport modelling in FLUKA.

Element name	Modulator box plate	Main box entrance plate	Main box exit plate	Patient's nozzle
Assigned material	ALUMINIUM	ALUMINIUM	ALUMINIUM	BRASS
Start /end location [cm]	32.6	75.0 / 77.0	145.0 / 147.0	147.0 / 154.0
Thickness [cm]	2.5	3.0	2.0	7.0
Radius / W x H [cm]	30.6 x 30.1	30.6 x 30.1	30.6 x 30.1	Inner: 1.7 Outer: 3.5

Table 16: Settings for particles transport for CCC beam line modelling in FLUKA.

FLUKA default card	PRECISIOn	
Particle type	$\mathrm{E_{min}}$ [MeV]	$\mathrm{E_{max}}$ [MeV]
Protons	0.1	60.0
Delta rays production threshold	0.1	-
Electrons / Positrons	0.001	60.0
Neutrons	0.001	60.0

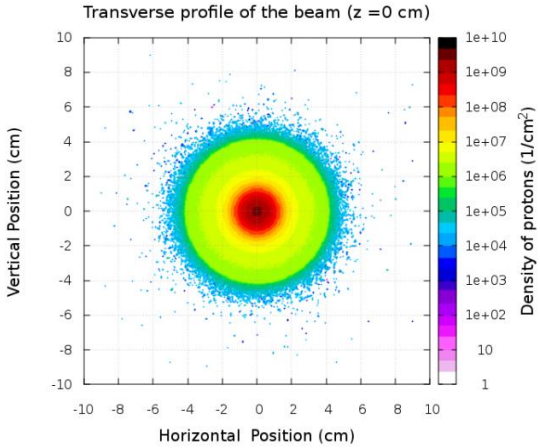

Figure 60: Theoretical distribution of protons in the transverse plane at z = 0.0 cm in the integration region for the initial number of particles $N = 1 \cdot 10^{10}$, corresponding to $I = 1.6$ nA.

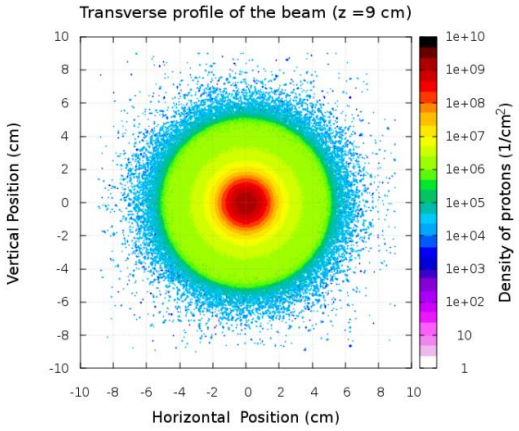

Figure 61: Theoretical distribution of protons in the transverse plane at z = 9.0 cm in the integration region for the initial number of particles $N = 1 \cdot 10^{10}$, corresponding to $I = 1.6$ nA.

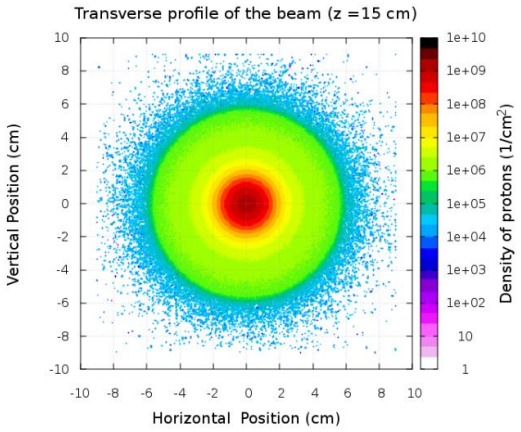

Figure 62: Theoretical distribution of protons in the transverse plane at z = 15.0 cm in the integration region for the initial number of particles $N = 1 \cdot 10^{10}$, corresponding to $I = 1.6$ nA.

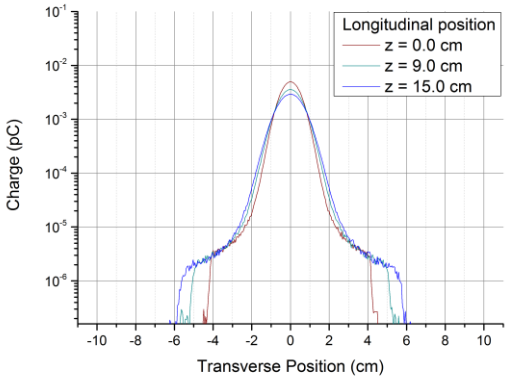

Figure 63: Transverse beam charge distribution in the proton beam for three LHCb VELO detector locations in the beam propagation direction for the beam current

The evolution of the halo shape shows the mentioned broadening of the Gaussian part of the beam with the distance traversed in the z axis. The divergence of the beam calculated at the FWHM of the distribution is $\alpha = 1.34° \ (0.023 \text{ radians})$. As a result, profile becomes flatter and less intense in the centre when travelling between $z_1 = 0.0$ cm and $z_3 = 15.0$ cm with simultaneous increase of the proton intensities towards the edges. These dependencies can be examined in figure 63, where a transverse charge distribution in the beam around the horizontal axis was plotted for the initial number of particles corresponding to the beam current $I = 1.6$ nA.

Studies into the performance of the non-invasive monitor to estimate the expected amplitude values per strip recorded in the VELO detector, as an answer to the interactions with

the described proton distribution at CCC, are presented in the following chapter. It shall be noted, that the low intensity of protons around the region of the circular rim of the halo is below sensitivity of the monitors used in quality assurance of the accelerator due to their capacitance and noise levels, unlike for the VELO detector.

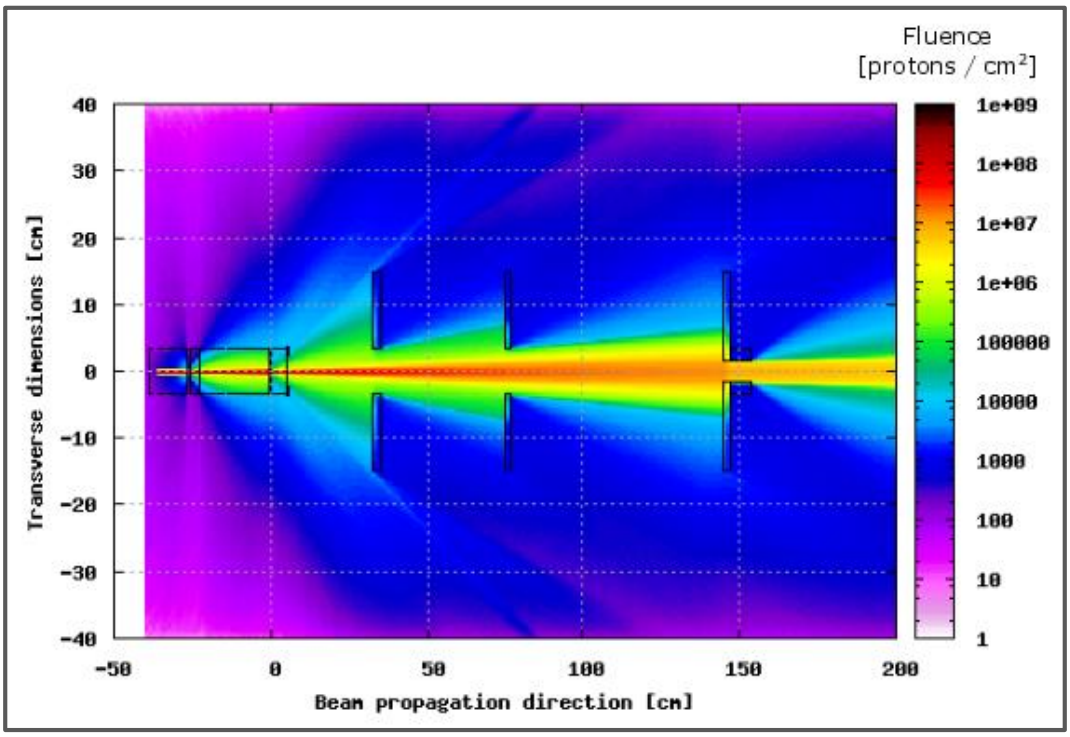

Figure 64: Treatment beam transport at CCC modelled in FLUKA integrated in the horizontal plane x.

Chapter Summary

This chapter gave of a review of the beam transport model at CCC, where the emittance and divergence of the beam were found at the position of the scattering foils using the quadrupole variation scans. Results of the latter were presented and discussed. The beam Twiss parameters calculated for the position of the scattering foils were employed as an input for the beam transport studies through the treatment beam line to the iso-centre using Monte Carlo methods. Proton halo maps were plotted and the overall behaviour of the beam was assessed. These, in the following chapter, will be used to find the expected amplitude values in the VELO detector.

6. NON-INVASIVE BEAM CURRENT MONITOR

The previous chapters presented the design paths and tests of the elements, which together compose the proposed non-invasive beam current monitor. The following section will conclude with the arrangement of the experimental set-up tested at Clatterbridge Cancer Centre. Monte Carlo investigations to estimate the expected amplitude of signal in the silicon sensors depending on their position in the halo region will be shown and will be followed by a summary of the performance of the conceptual monitor using measurements with the treatment proton beam.

6.1 Materials, data collection and analysis

The proposed non-interceptive beam current monitor set-up was installed at CCC to perform tests using the therapeutic proton beam. In preparation of the VELO detector for the first run, essential dry run tests were performed to determine the optimal set of working condition parameters which allowed safe operation of the detector at low temperatures in ambient atmosphere. These involved both mechanical design and performance tests:

- Matching of the cooling fluid with the design of the cooling system, powered by an ATC K3 chiller: to alleviate excessive heat absorption from ambient air by the coolant in the pipework as a result of slow flow caused by the viscosity of the fluid at the temperature $\mathrm{T} = \text{-}28$ ℃.
- Adjusting the dry air flow rate to guarantee condensation free operation of the detector hybrids: the desired flow was set to $\mathrm{V} > 60\ \mathrm{l/s}$ at a pressure $\mathrm{p} = 4.5$ bars for the dew point for the compressor being specified at $\mathrm{T_{dew\ point}} = -20$ ℃.
- Performance tests of the on-board trigger adapters for sending the readout signal to the Beetle chips in absence of an optical triggering system. They were manufactured for the project and assembled in accordance with the technical drawings exploiting a list of electronic elements available on CERN technical documentation servers**.**
- Adjustment of the timing parameters of the customised 10 m long signal cables to compensate for their cross talk.
- Noise tests to determine the dark count and pedestals per read out channel.

- Mock tests at CCC of the prototyped detector stand and devised alignment procedure.
- Investigation of the response of the FC coupled to a Keithely 486 Picoammeter to the irradiation with the proton beam versus potential applied to the guarding ring.

Figure 65: Overview of the non-invasive beam monitor test assembly at CCC: the stand hosting the VELO modules is visible behind the treatment box, a rack hosting the electronics on the right integrating TELL1 cards and their dedicated cooling, high and low voltage power supplies, DAQ computer and communication network. The FC vessel can be seen at the end of the treatment line in the top left quarter of the image.

The proton beam halo was monitored at three longitudinal locations in the beam propagation direction, as depicted in figure 66, with the origin at a distance of 6.9 cm from the beam modulator box wall. The origin of measurements, marked as $z = 0.0\ \mathrm{cm}$ in the monitor stand coordinate system, was equal to the minimum space required to accommodate the structures of the detector stand. Furthermore, two additional locations were used for the measurement series at $z = 9.0\ \mathrm{cm}$ and $z = 15.0\ \mathrm{cm}$. The transverse distributions of protons in the halo region were determined for the detector hybrids positioned symmetrically with respect to the beam axis at three transverse locations, that is $x = 0.0\ \mathrm{cm}$, $x = 1.0\ \mathrm{cm}$ and $x = 2.0\ \mathrm{cm}$.

Clinical operation of the accelerator requires precise knowledge of the dose delivered to the patient within a specified accuracy. The radiotherapy standards tackle this subject by using a unit of beam delivery called Monitor Unit (MU). [100] The definition of that value states that in a dose monitoring system, MU is an arbitrary unit in which a quantity is displayed and from which the absorbed dose can be calculated. In the course of the data collection three values of

the dose rate, expressed as MU/min, were investigated and linked with the proton beam intensity measured at the treatment isocentre by the FC. Their representation covered the range for the lowest, middle and highest dose rate values used clinically at CCC within the beam stability limitations of the accelerator. They also comprised of the minimum statistically relevant representation of the measurements possible to acquire within the limits of the available beam time.

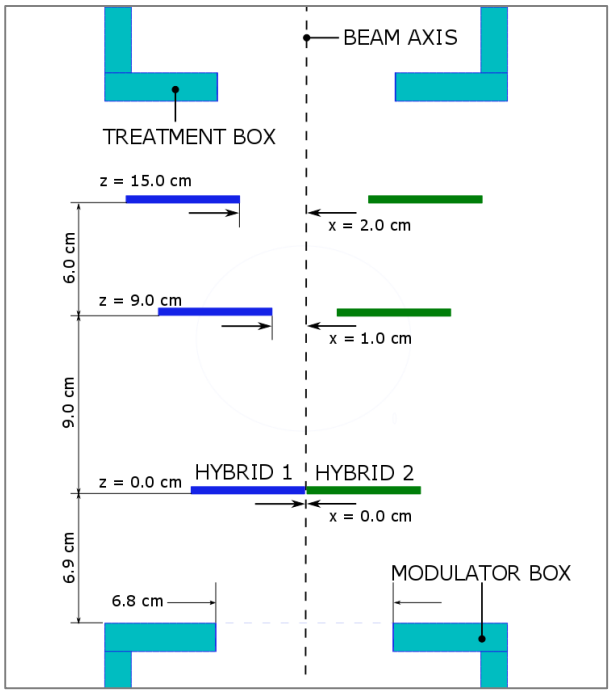

Figure 66: Locations of the VELO detector in the integration space on the CCC treatment line for assessing the performance of the non-invasive beam current monitor. The longitudinal positions in the beam propagation direction are noted with z and the transverse positions are noted with x.

The mode of operation of the VELO at the stage of experiment, where the timing of the of the detector readout was not correlated with the bunch crossing frequency, constrained the data analysis to investigating correlation between the measured proton halo intensity, expressed as the average amplitude of the ADC counts integrated across a region of interest of a given sensor per a readout event, and the average beam current value measured by the FC. The bias potential to establish the depletion region in the silicon sensors was set to $100\ \mathrm{V}$.

The triggering of both detectors was performed manually. The first readout signal from the mezzanine trigger adapter was sent to the Beetle chips after $t \sim 19.0\ \mathrm{s}$ from calling the detector readout function on the control/DAQ computer. In the given interval necessary on-

board diagnostics were performed after the TELL1 firmware had been loaded onto the cards from the control computer.

An example of data collection flow is depicted in figure 67. The data readout from the sensors was sequential, saving information from only one sensor during the readout event. Signals gathered from the hybrids by TELL1 cards were sent via a G-bit Ethernet series connection to the DAQ computer for storage and post processing. The detector was running in a non-zero-suppressed mode, saving full raw data information per strip to a binary '.mdf' file by the bespoke CERN readout software. Further off – line analysis was completed using VETRA script tailored to the obtained datasets format to rearrange them for further processing. The common mode correction algorithm was disabled in the analysis to avoid truncating of the ADC information. The processed data containing ADC information per strip per readout event was next analysed with a developed MATLAB script. At each of the locations, the VELO detector was programmed to collect 16000 readout events before the data collection was terminated.

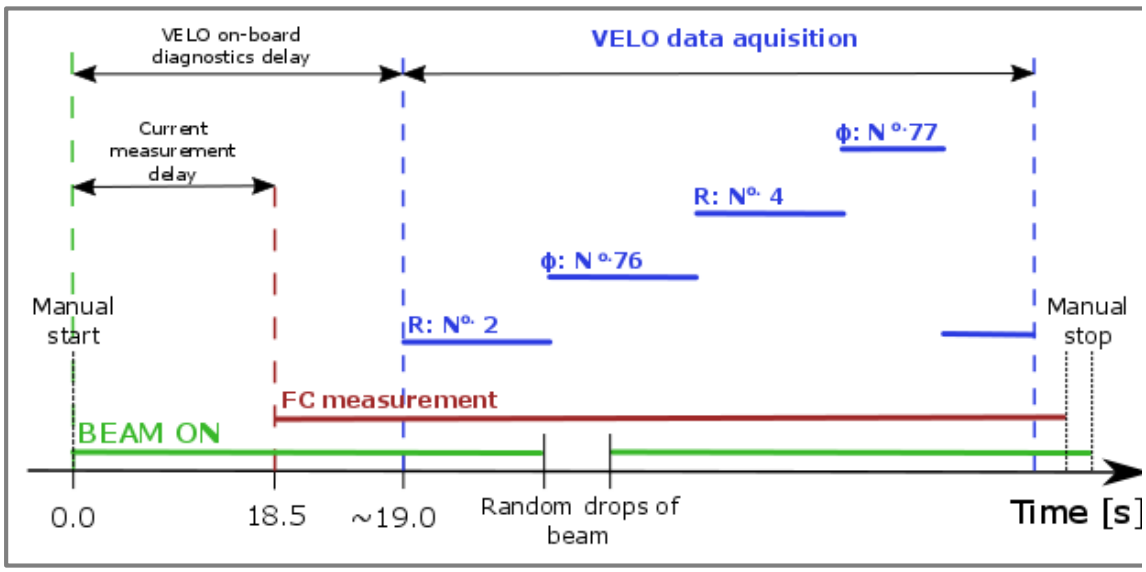

Figure 67: Data acquisition flow chart of the performance tests of the non-invasive beam current monitor. The VELO detector acquisition was sequential.

The investigated proton beam halo region can be defined as protons found at positions larger than $d = 1.7\ \mathrm{cm}$ in the radial frame from the beam axis. They do not take part in the treatment of the patient and are terminated in the metal elements of the treatment line. This is related to the radius of the treatment nozzle mounted directly before the treatment iso-centre at the end of the main diagnostic box. With regard to the divergence of the beam, any protons leaving the second scattering foil at an angle larger than $0.012\ \mathrm{radians}$ ($\sim 0.7°$) are beyond the

acceptance of the nozzle. Therefore, the beam halo extent can be redefined in the integration region of the VELO and varies with the position along the z axis in the beam propagation direction. For the available VELO stroke between $\mathrm{z} = 0.0\,\mathrm{cm}$ and $\mathrm{z} = 15.0\,\mathrm{cm}$ in the coordinate system of the stand, the halo can be understood as particles in the transverse plane to the beam propagation direction found at the radius larger than $\mathrm{r_{halo}} = 0.35\,\mathrm{cm}$ from the beam axis. Consequently, the VELO detector positioned in the transverse plane $\mathrm{x} = 0.0\,\mathrm{cm}$ falls already into the defined halo region as the radius of the central part of the detector is larger than $\mathrm{r_{halo}}$.

6.2 Faraday Cup measurement results

The Faraday Cup coupled with a Keithley 486 picoammeter provided absolute beam intensity values for the data analysis. The vacuum vessel hosting the aluminium beam stopper was positioned at the treatment isocentre with a dedicated coupler mounted onto the treatment nozzle.

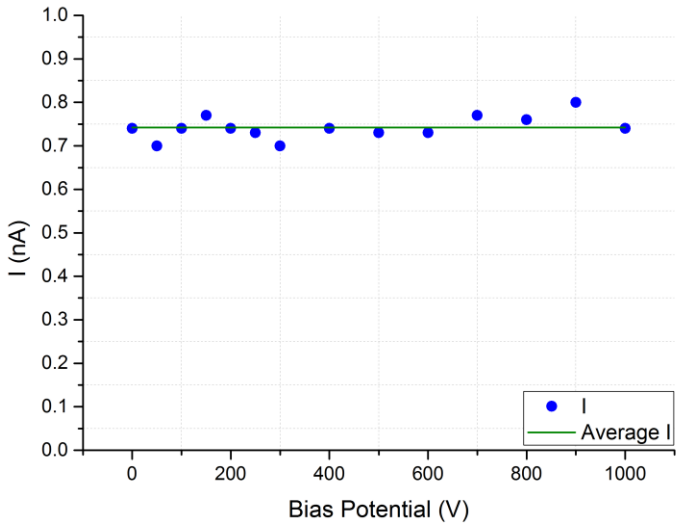

Figure 68: Response of FC to the proton beam at the dose rate of 30 MU/min versus the bias potential on the guarding ring.

The measured proton beam intensities were integrated in approximately $50\,\mathrm{ms}$ intervals and logged into a '.txt' file. The trigger signal for the beam current measurement software was introduced manually, simultaneously with the start-up of the LHCb VELO detector. The actual start of data acquisition had a software introduced delay aligned with the TELL1 cards diagnostics.

The performance of the FC was assessed by checking the behaviour of the measured beam intensity as a function of the bias potential on the guarding ring at a dose rate of $\mathrm{MU}_3 = 60\ \mathrm{MU/min}$. No fluctuations of the measured beam value were observed, other than those originating from the stability of the delivery by the accelerator, figure 68.

The average beam intensity values were calculated using a script implemented in MATLAB, which produced an arithmetical average of the bins logged in the .txt file for those values exceeding the noise threshold of the picoammeter. The uncertainty of the estimated beam current was calculated following the formula:

$$u(I) = \sqrt{\frac{\sum_{i=1}^{n}(I_i - \bar{I})^2}{n \cdot (n-1)}} \tag{74}$$

Where:

i - Bin number;

n - Overall number of bins containing the beam current values larger than the set noise cut-off threshold;

I_i - Value of the beam current for bin i, nA;

$\bar{I}$ - Average value of the current calculated for n bins, nA.

A series of beam intensity measurements performed with the FC were used to determine their relation to the treatment dose rate, expressed in MU, and summarized in table 17. The reproducibility of accelerator delivery was estimated as the ratio between the uncertainty of the calculated average current value to that average value for a given dose rate.

Table 17. Dose rate / beam current values tested with the monitor.

Dose rate [MU/min]	10	30	60
Average current $\bar{\mathrm{I}}\ (\mathrm{nA})$	0.126	0.374	0.751
Uncertainty $\mathrm{u}_{95\%}(\bar{\mathrm{I}})\ (\mathrm{nA})$	0.014	0.046	0.052
Reproducibility of the dose rate	12.54 %	12.52 %	9.72 %

It should be noted that the reproducibility of the delivery at the confidence level of 95 % is around 10% for the tested nominal dose rates. Nevertheless, the linearity of the beam

current versus the dose is preserved and the linear fit to the experimental data points was found as $\mathrm{R}^2 = 0.99998$, figure 69.

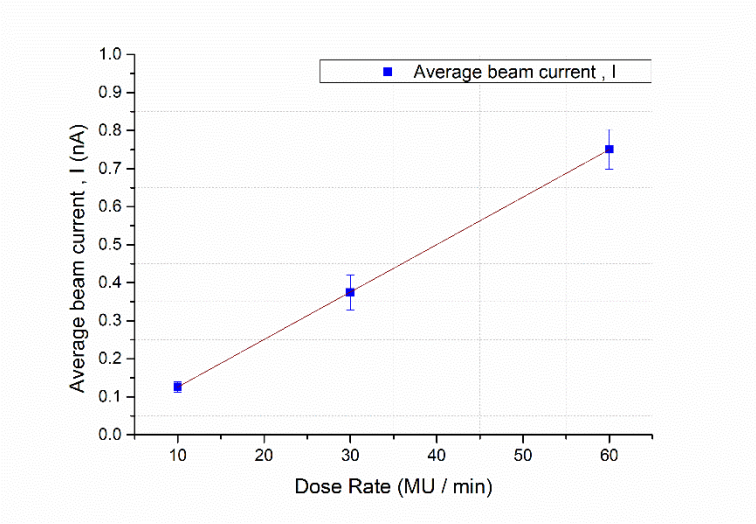

Figure 69: Beam current versus dose rate dependence.

In the course of analysis, the actual average beam current values were used as measured by the FC for each VELO experimental location and given dose rate.

6.3 LHCb VELO Response Amplitude Predictions

The performance of the proposed non-invasive beam monitor, based on the VELO detector, strongly depends on the response of the detector to interactions with non-minimum ionizing particles as the 60 MeV protons at CCC. Therefore Monte Carlo studies were carried out to estimate the ADC amplitude per strip in the R-sensor at the consecutive experimental positions in order to investigate any possible saturation of the detector. Studies were carried out in FLUKA for the detector locations following the experimental layout described in section 6.1. The surface of the R-sensor was divided into four azimuthal bins, following the strip architecture, figure 34. Every sector was divided into 41 equal radial bins with bin width $\mathrm{x}_{\mathrm{bin}} = 0.82\ \mathrm{mm}$, small enough to reproduce Gaussian shape fall off at the beam edge. Mapping the strips positions within the bin, the highest strip density was in the inner bins, with the maximum of 20 strips / bin, and decreasing by more than a half, to 8 strips / bin, for the outer bins.

The USRBIN FLUKA estimator was used to find the expected energy deposited in the volume of each bin. Figure 72 presents an example of the calculated energy deposition for the R-sensor at the location z, $\mathrm{x} = (0.0,\ 0.0)$. The number of produced electrons per bin was calculated by dividing the energy deposited by the electron – hole pair production threshold for

silicon $\mathrm{E}_{\mathrm{electron-hole}} = 3.6$ eV. Approximately 450 detected electrons are translated to 1 ADC count by the data acquisition software. Ultimately, the magnitude of the amplitude per strip per bunch was found as a function of the beam current and for the first inner bin the results were the following, see also figure 70 for reference:

- 6.67 ADC/strip/bunch for the beam current $\mathrm{I} = 0.112$ nA, (10 MU/min);
- 17.86 ADC/strip/bunch for the beam current $\mathrm{I} = 0.320$ nA, (30 MU/min);
- 43.54 ADC/strip/bunch for the beam current $\mathrm{I} = 0.870$ nA, (60 MU/min).

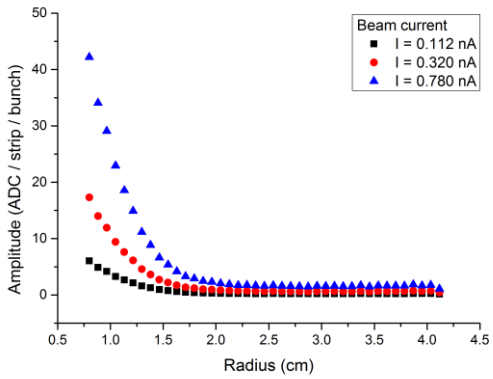

Figure 70: Estimated average amplitude of signal per diode strip in the R – sensor as a function of the proton beam current I. The beam current values correspond to the approximated beam dose rate values of $10, 30$ and $60\ MU/min$. The location of the detector: longitudinal z = 0.0 cm, transverse x = 0.0 cm.

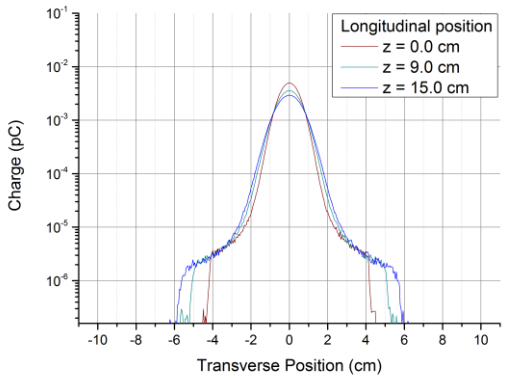

Figure 71: Beam transverse charge distribution at the experimental locations in the beam propagation direction for the beam intensity $I = 1.0\ nA$.

The ADC distribution as a function of radius follows the charge distribution of the Gaussian shaped beam in the fall off region, figures 71 and 72. The beam profile widening with the increasing distance along z-axis is observed in an increase of the ADC amplitude between the detector location z, $\mathrm{x} = (0.0, 0.0)$ at the two other longitudinal points of measurement (figures 72 to 74). The initial growth in the signal between $\mathrm{z} = 0.0$ cm and $\mathrm{z} = 9.0$ cm levels down at $\mathrm{z} = 15.0$ cm due to flattening of the proton density in the beam centre with the travelled distance, see figures 71 and 75. The estimated average amplitude per strip for the maximum dose rate doesn't reach the saturation values. For the full range of the ADC counts, the saturation region can be calculated as a difference between the available ADC range, namely 1024 ADCs, decreased by the pedestal values, which are normally in the range of 480 to 520 ADCs. Therefore the estimated average values of 60 ADCs in the inner strips for the dose

rate of $60\ \mathrm{MU/min}$ are in the predicted detector range of operation for the highest proton intensity at $\mathrm{x} = 0.0\ \mathrm{cm}$. The transverse distribution of hits is sector dependent, meaning that that the two azimuthal sectors, adjacent to $0°$ axis, for $\mathrm{x} = 1.0\ \mathrm{cm}$ and $\mathrm{x} = 2.0\ \mathrm{cm}$, will experience less energy deposition as opposed to the two vertical sectors at $90°$ and $-270°$ axes, refer to figures 12 to 14 and the following energy deposition plots. The estimated value of ADCs per strip increases with the longitudinal position and the increasing lateral spread of the beam.

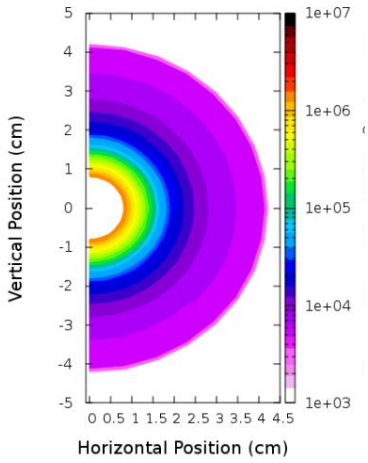

Figure 72. Average energy deposition in R–sensor per bunch for the location: longitudinal z = 0.0 cm, transverse x = 0.0 cm.

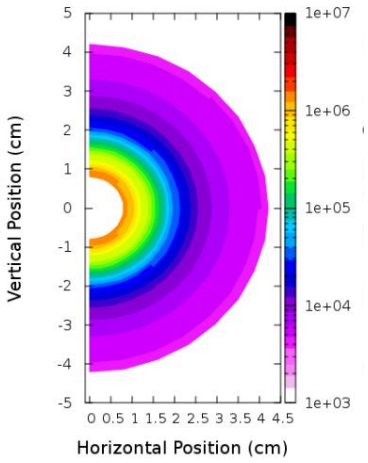

Figure 73. Average energy deposition in R – sensor pre bunch for the location: longitudinal z = 9.0 cm, transverse x = 0.0 cm.

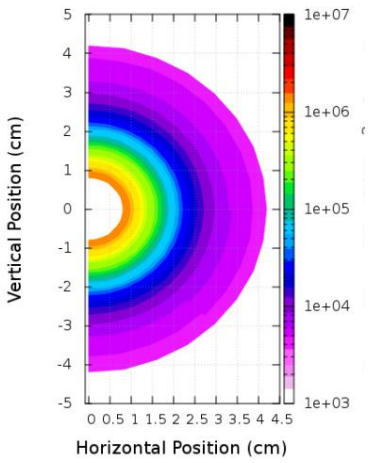

Figure 74. Average energy deposition in R- sensor per bunch for the location: longitudinal z = 15.0 cm, transverse x = 0.0 cm.

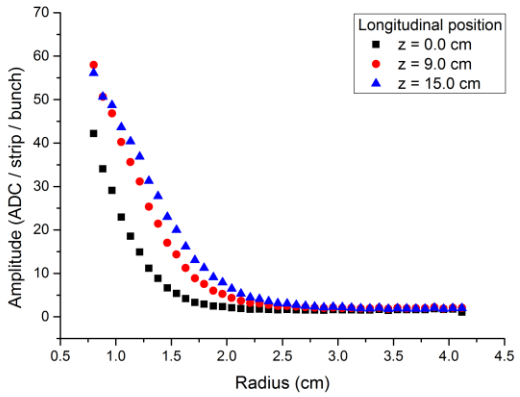

Figure 75: Estimated average amplitude of signal per diode strip in the R – sensor per bunch as a function longitudinal position for the dose rate of $60\ \mathrm{MU/min}$ and the transverse location x = 0.0 cm.

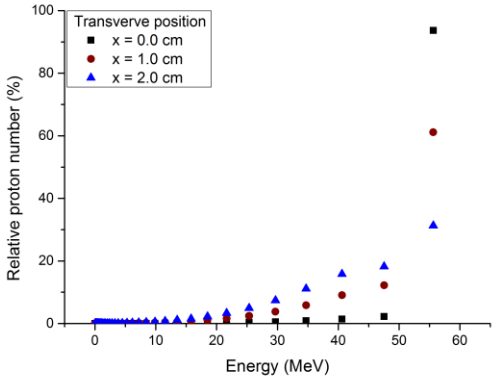

Figure 76: Normalized energy distribution of proton beam halo traversing though LHCb VELO sensors at the longitudinal position z = 0.0 cm and for the three locations in the plane transverse to the beam propagation direction.

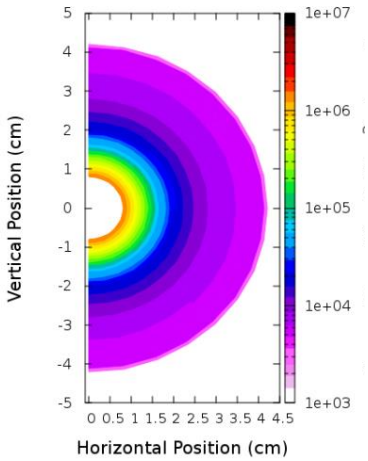

Figure 77: Average energy deposition in R – sensor per bunch for the location: longitudinal z = 0.0 cm, transverse x = 0.0 cm.

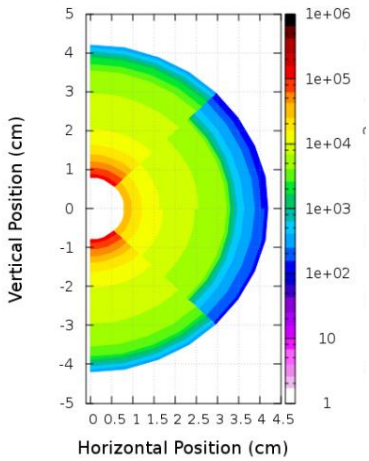

Figure 78: Average energy deposition in R – sensor per bunch for the location: longitudinal z = 0.0 cm, transverse x = 1.0 cm.

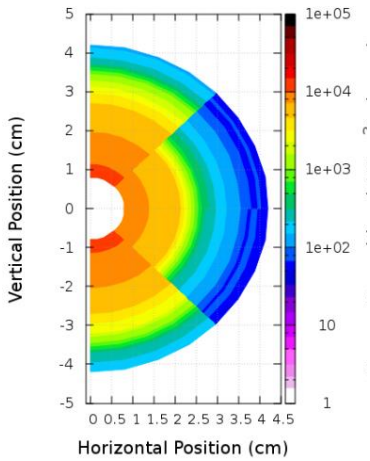

Figure 79: Average energy deposition in R – sensor per bunch for the location: longitudinal z = 0.0 cm, transverse x = 2.0 cm.

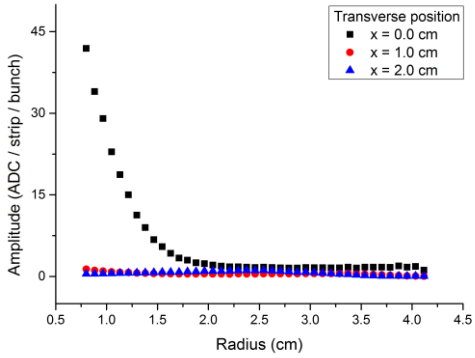

Figure 80: Estimated average amplitude of signal per diode strip in the R – sensor per bunch as a function of position in the plane perpendicular to the beam propagation direction at the longitudinal position $z = 0.0\ cm$.

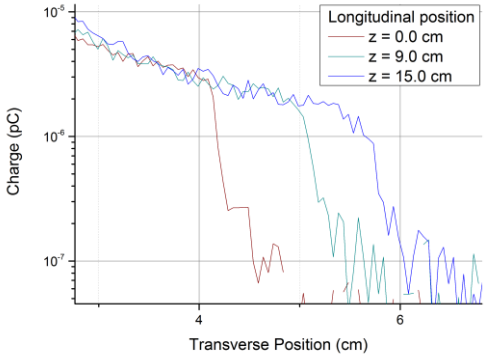

Figure 81: Estimated proton beam edge versus longitudinal position for the beam intensity $\mathrm{I} = 1\ \mathrm{nA}$.

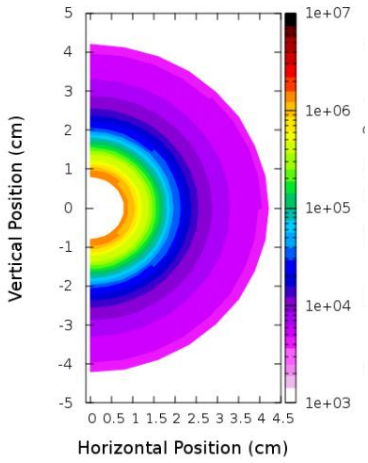

Figure 82: Average energy deposition in the R – sensor per bunch for the location: longitudinal z = 9.0 cm, transverse x = 0.0 cm.

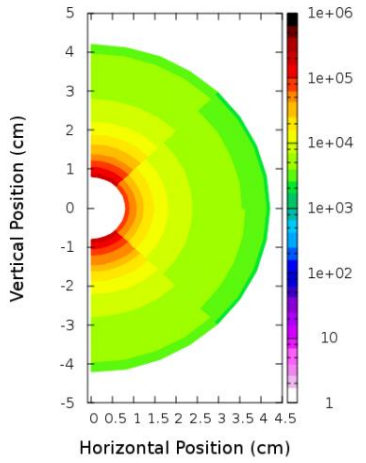

Figure 83: Average energy deposition in the R – sensor per bunch for the location: longitudinal z = 9.0 cm, transverse x= 1.0 cm.

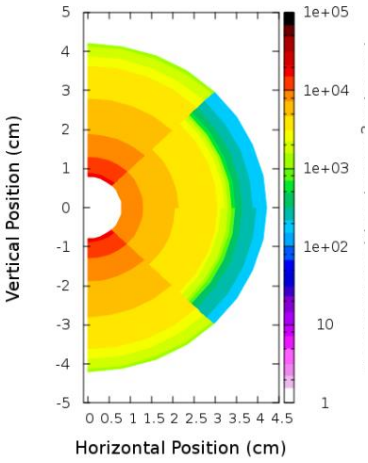

Figure 84: Average energy deposition in the R – sensor per bunch for the location: longitudinal z = 9.0 cm, transverse x = 2.0 cm.

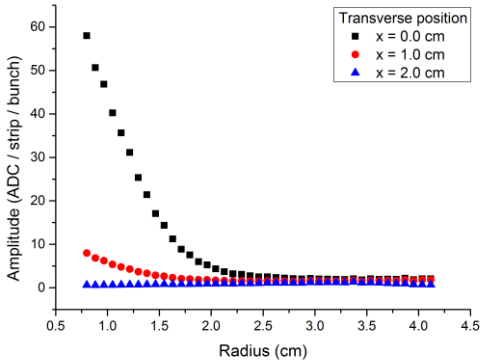

Figure 85: Estimated average amplitude of the signal per diode strip in the R – sensor per bunch as a function of position in the plane perpendicular to the beam propagation direction at the longitudinal position $z = 9.0$ cm.

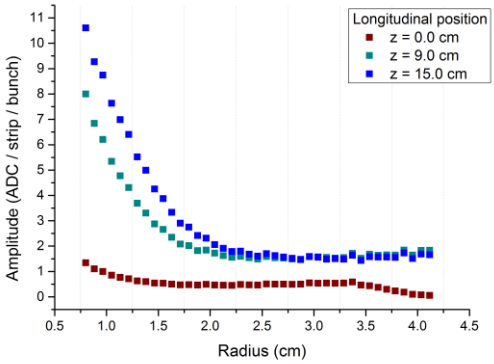

Figure 86: Estimated average amplitude of signal per diode strip in the R – sensor per bunch as a function position in longitudinal direction for the transverse position$x = 1.0$ cm.

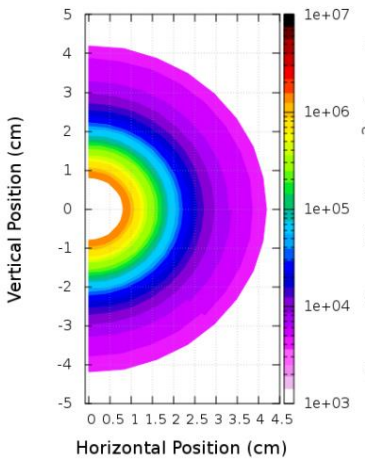

Figure 87: Average energy deposition in the R – sensor per bunch for the location: longitudinal z = 15.0 cm, transverse x = 0.0 cm.

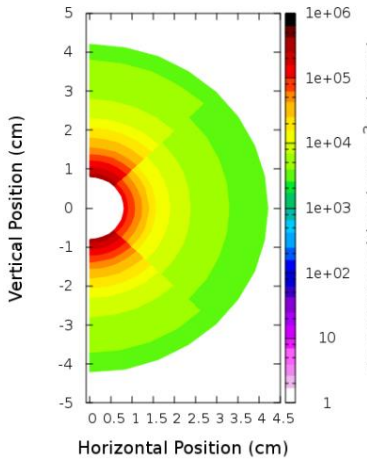

Figure 88: Average energy deposition in the R – sensor per bunch for the location: longitudinal z = 15.0 cm, transverse x = 0.0 cm.

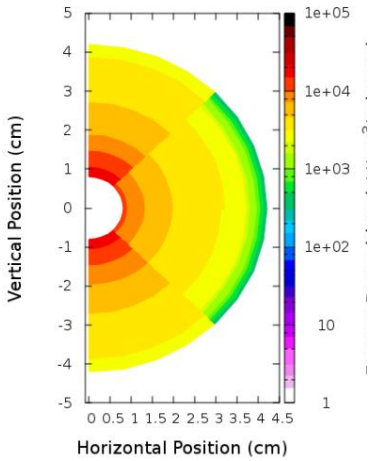

Figure 89: Average energy deposition in the R – sensor per bunch for the location: longitudinal z = 15.0 cm, transverse x = 0.0 cm.

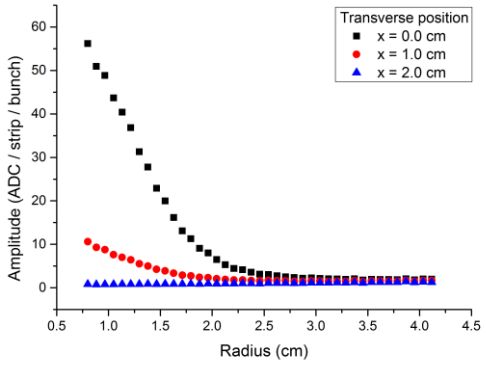

Figure 90: Estimated average amplitude of signal per diode strip in the R – sensor per bunch as a function of position in the plane perpendicular to the beam propagation direction at the longitudinal position z = 15.0 cm.

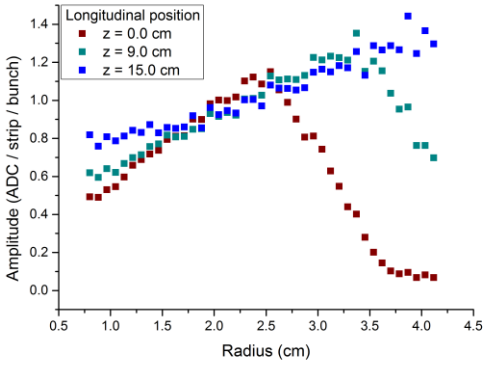

Figure 91: Estimated average amplitude of signal per diode strip in the R – sensor per bunch as a function of position in longitudinal direction for the transverse position x = 2.0 cm.

It can been seen that the sharp proton halo fall-off, determined by the beam line structures, is to be detected by the detector in the radial distributions of the ADC counts at two first detector positions in the longitudinal direction $z_1, x_1 = (0, 0)$, $z_2, x_2 = (9, 0)$, figures 81 and 91.

The presented theoretical predictions of the ADC amplitude per strip per bunch were obtained using the Monte Carlo method, where the estimators are based on the statistical distributions of a large number of particles crossing a given volume. Therefore, the energy

deposition maps reflect only on uniform distributions of ionisation in a bin. In practice, ionisation in silicon along the path of a traversing proton is much more localized. Additionally, the bias potential applied to the sensor minimizes the lateral drift of electrons and charge sharing between the strips enhancing the value of the collected charge per strip. Therefore, the estimated amplitudes per strip and readout event gave an approximation of the average detector radial performance, however, they do not reflect on the peak values of the ADCs per strip.

6.4 Experimental results analysis and discussion

6.4.1 Pedestals, noise and readout threshold determination

The pedestals and noise evaluation was estimated using 16000 events collected for the detector installed at the experimental location with the beam-off. An RMS amplitude of the dark count in each sensor was calculated as a function of the strip, figures 92 to 97. It must be emphasised that the Mean Common Mode Suppression (MCMS) algorithm was disabled during the course of analysis to avoid truncating the amplitude values, when strip-to-strips variation of amplitude is significant and not negligible. The differences in the RMS values of noise for the two variants of the MCMS algorithm enabling are presented in figure 92.

Table 18: Parameters of the statistical distribution of noise in the R - and ϕ- sensors.

Detector No.	**2**	**4**	**76**		**77**	
			Region		Region	
			Middle	Right	Middle	Right
Median (ADC)	2.90	2.38	3.25	3.31	1.94	1.90
Standard deviation (ADC)	0.56	0.65	0.57	0.44	0.24	0.34

The spectra of noise in the radial and azimuthal sensors are different, what has source in the layout of the readout lines. Whilst in the R- sensor the lines run radially and cross with the horizontally oriented diode strips at normal angles, their noise spectra are uniform and for the hybrids used in the experiment can be well approximated by a normal distributions, figures 94 and 95. The median values of noise for sensors No. 2 and No. 4 can be found in table 18. The noise spectrum in the ϕ -sensor can be characterised by three separate distributions corresponding one to the inner strips, and the other two to the outer strips. The latter

demonstrate two different spectra representing the even and odd strips. Noise in the odd strips is enhanced by the readout lines of the inner strips running radially above them to the readout pads at the circumference and is represented by the far right two peaks in figures 98 and 99. As a result of the architecture impacting that noise distribution, the quantitative description presented in table 18 is split in two in the outer region, termed 'Middle' and 'Outer'.

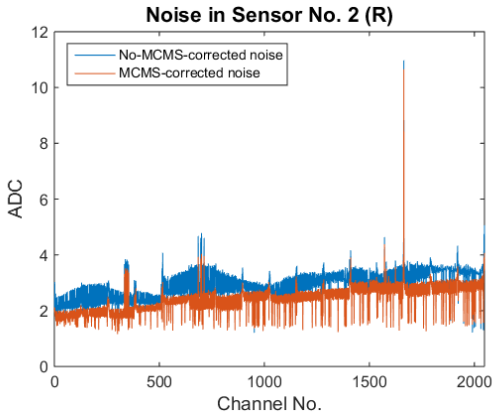

Figure 92: Noise per channel in R - sensor No. 2.

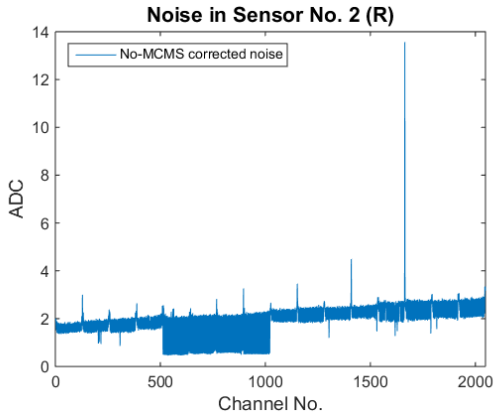

Figure 93. Noise per channel in R - sensor No. 4.

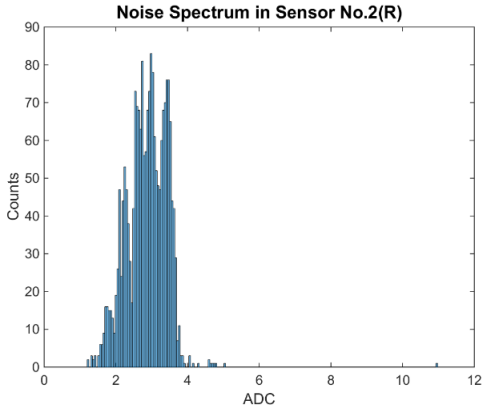

Figure 94: Spectrum of noise in R - sensor No. 2.

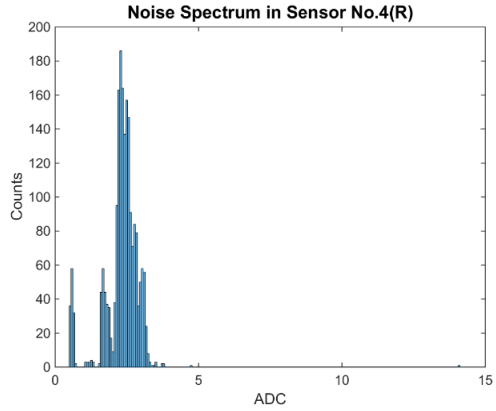

Figure 95: Spectrum of noise in R sensor No. 4.

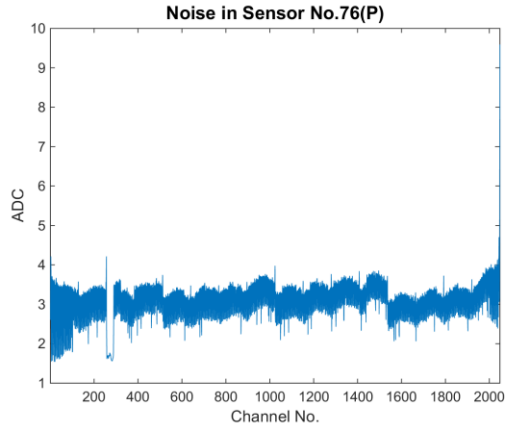

Figure 96: Figure 18: Noise per channel in ϕ - sensor No. 76.

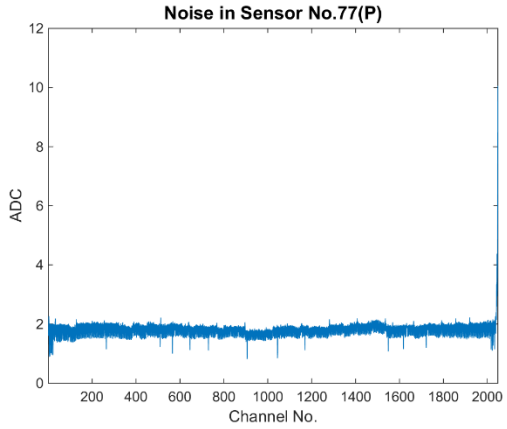

Figure 97: Figure 18: Noise per channel in ϕ - sensor No. 77.

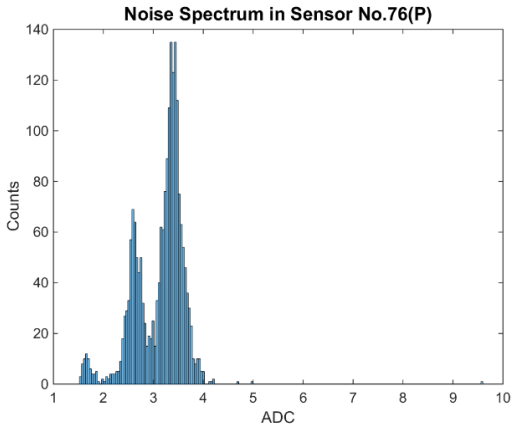

Figure 98: Spectrum of noise in ϕ - sensor No. 76.

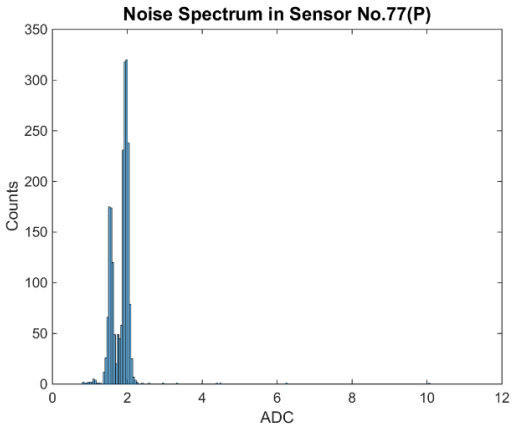

Figure 99: Spectrum of noise in ϕ - sensor No. 77.

Furthermore, the analysis of the noise spectrum in the sensors allowed the required noise cut-off threshold to be determined, introduced to suppress the events contributing to the analysis including also low event amplitude quality. Figures 100 to 103 illustrate the spectrum of hits for the series of readout events for the VELO detector positioned at $z, x = (0.0, 1.0)$ and exposed to the proton beam at the dose rate of $10\ \mathrm{MU/min}$, where the analysis was performed with the cut off level $T_{\text{cut-off}} = 0.0\ \mathrm{ADCs}$ above the noise level. The actual signal from the proton interactions proved to have amplitudes reaching up to 300 ADCs per strip, however, their number related to the total number of recorded hits was significantly reduced. To efficiently suppress the noise hits, a minimum cut-off level, equivalent of a quadrupled value of the median RMS amplitude $T_{\text{cut-off}} = 12\ \mathrm{ADC}$, was introduced to the analysis.

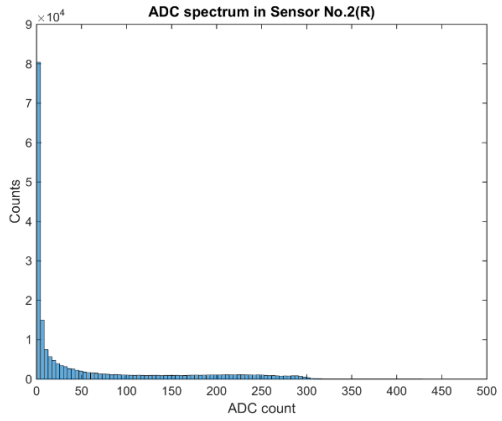

Figure 100. Spectrum of amplitude values for the R – sensor No. 2 for the dose rate 10 MU/min and the cut-off threshold $T_{cut\text{-}off}$ = 0.0 ADC. The position of the detector: longitudinal z = 0.0 cm, transverse x = 1.0 cm.

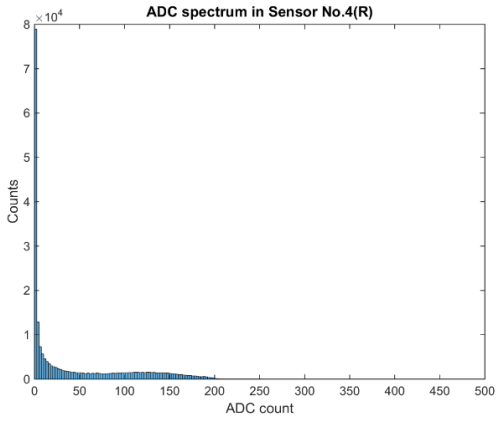

Figure 101. Spectrum of amplitude values for the R - sensor No. 4 for the dose rate 10 MU/min and the cut-off threshold $T_{cut\text{-}off}$ = 0.0 ADC. The position of the detector: longitudinal z = 0.0 cm, transverse x = 1.0 cm.

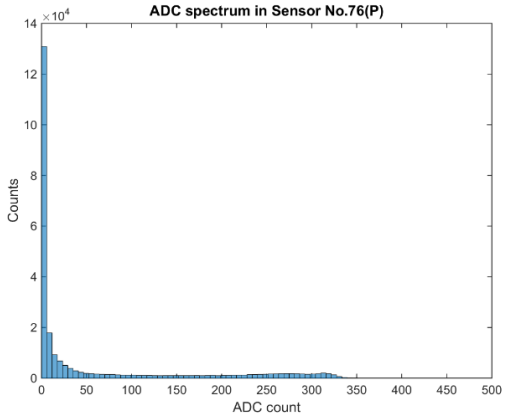

Figure 102: Spectrum of amplitude values for the ϕ - sensor No. 76 for the dose rate 10 MU/min and the cut-off threshold $T_{cut\text{-}off}$ = 0.0 ADC. The position of the detector: longitudinal z = 0.0 cm, transverse x = 1.0 cm.

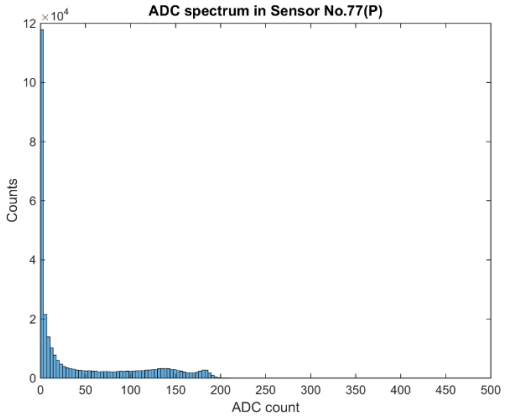

Figure 103: Spectrum of amplitude values for the ϕ - sensor No. 77 for the dose rate 10 MU/min and the cut-off threshold $T_{cut\text{-}off}$ = 0.0 ADC. The position of the detector: longitudinal z = 0.0 cm, transverse x = 1.0 cm.

6.4.2 Qualitative description of signal measured in the beam halo region

The applied noise cut-off threshold enhanced the ADC amplitudes measured by the diode strips in both types of the VELO sensors exposed to the proton beam halo. This enabled investigation of the deterministic part of the spectrum. The series of plots in figures 104 to 107 illustrate the hits histograms integrated across the strips in both types of sensors for the hybrids located at $\mathrm{z,x} = (0.0,\ 0.0)$ and the dose rate $10\ \mathrm{MU/min}$. It should be mentioned here that there is a mismatch between the maximum ADC value recorded by hybrid No. 1 (sensors No. 2 and No. 76) and hybrid No. 2 (sensors No. 4 and No. 77). The reported difference reached 100 ADCs. This could be related to the worse noise characteristics and observed

modulation, however, the exact nature of the phenomena, post measurements, could not be determined.

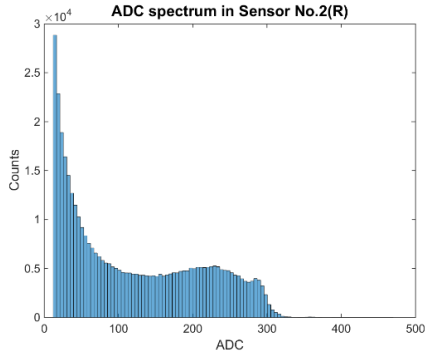

Figure 104: Spectrum of the amplitude values for the R-sensor No. 2 for the dose rate 10 MU/min, $T_{cut\text{-}off}$ = 12.0 ADCs and at the position: longitudinal z = 0.0, transverse x = 0.0 cm.

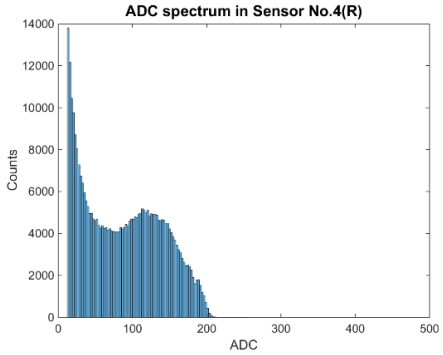

Figure 105: Spectrum of the amplitude values for the R-sensor No. 4 for the dose rate 10 MU/min, $T_{cut\text{-}off}$ = 12.0 ADCs and at the position: longitudinal z = 0.0, transverse x = 0.0 cm.

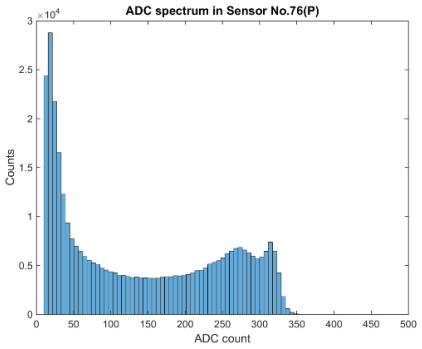

Figure 106: Spectrum of the amplitude values for the ϕ - sensor No. 76 for the dose rate 10 MU/min, $T_{cut\text{-}off}$ = 12.0 ADCs and at the position: longitudinal z = 0.0, transverse x = 0.0 cm.

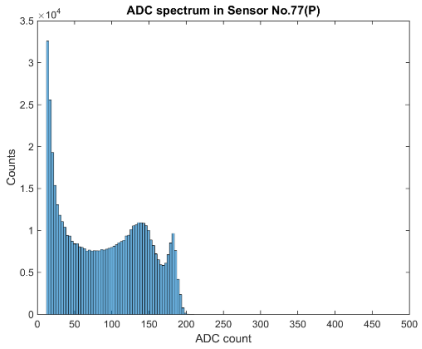

Figure 107: Spectrum of the amplitude values for the ϕ - sensor No. 77 for the dose rate 10 MU/min, $T_{cut\text{-}off}$ = 12.0 ADCs and at the position: longitudinal z = 0.0, transverse x = 0.0 cm.

Despite the observed maximum amplitude difference, studies into the relative response to changes in the beam intensity were not affected. The ADC integration per sensor versus event number can be followed in figures 108 to 111. In agreement with theory, this relationship demonstrates a linear increase. Fluctuations of the average amplitude increase are observed from event to event as a result of no-synchronisation between the bunch arrival time and VELO readout and proton beam stability.

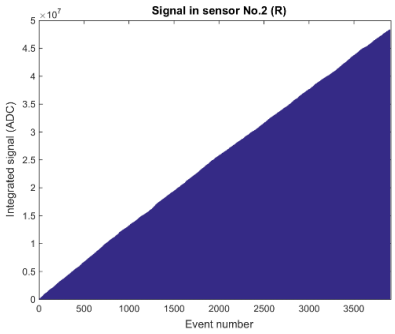

Figure 108: Signal integration by the R- sensor No. 2 for the dose rate 10 MU/min, $T_{cut\text{-}off}$ = 12.0 ADC and at the location: longitudinal z = 0.0 cm, transverse x = 0.0 cm.

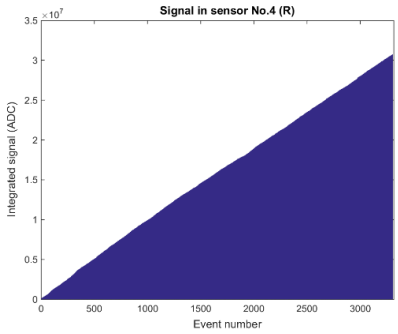

Figure 109: Signal integration by the R- sensor No. 4 for the dose rate 10 MU/min, $T_{cut\text{-}off}$ = 12.0 ADC at the location: longitudinal z = 0.0 cm, transverse x = 0.0 cm.

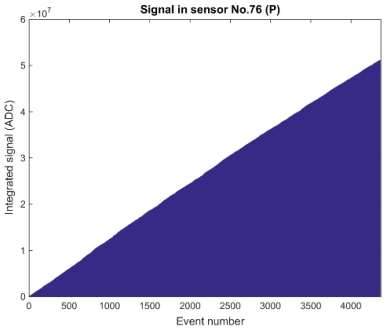

Figure 110: Signal integration by the ϕ- sensor No. 76 for the dose rate 10 MU/min, $T_{cut\text{-}off}$ = 12.0 ADC at the location: longitudinal z = 0.0 cm, transverse x = 0.0 cm.

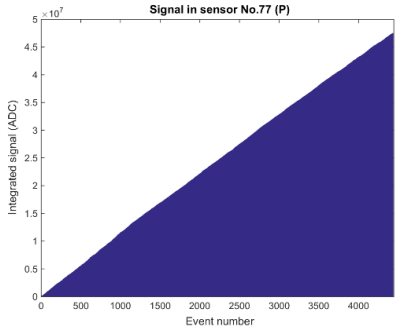

Figure 111: Signal integration by the ϕ- sensor No. 77 for the dose rate 10 MU/min, $T_{cut\text{-}off}$ = 12.0 ADC at the location: longitudinal z = 0.0 cm, transverse x = 0.0 cm.

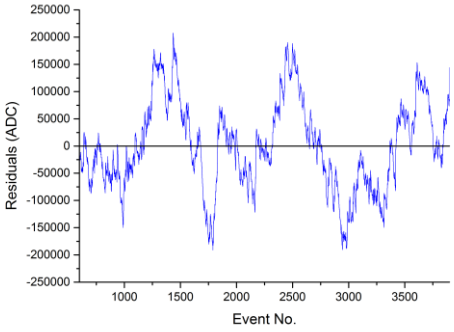

Figure 112: Residuals from a fit to the experimental points of average amplitude increase per event. The discreet structure of the amplitude variations originates from lack of exact bunch arrival time - VELO readout synchronisation and accelerator fluctuations.

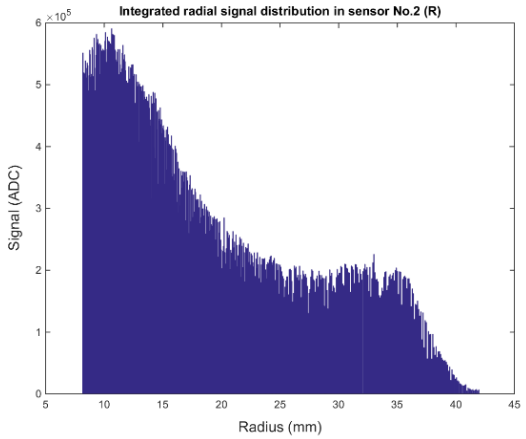

Figure 113: ADC signal integrated across recorded events versus radial position of a strip in the R- sensor No. 2 for the position: longitudinal z = 0.0 cm, transverse x = 0.0 cm.

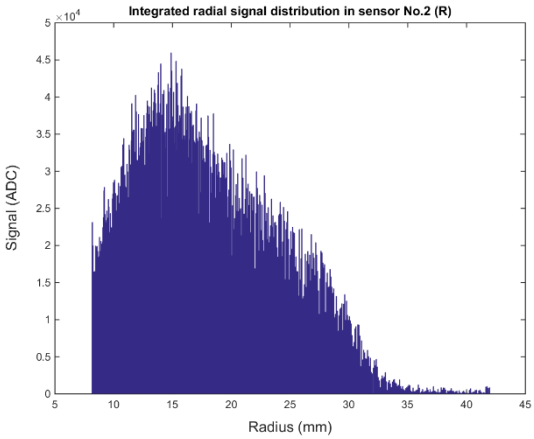

Figure 114: ADC signal integrated across recorded events versus radial position of a strip in the R- sensor No. 2 for the position: longitudinal z = 0.0 cm, transverse x = 2.0 cm.

Ultimately, the theoretical predictions of the signal shape in the R- sensors can be compared with the actual measured distributions. The simulated field edge, depicted in figure 81, is detected by the R-sensor for radii $\mathrm{r} > 36.0\,\mathrm{mm}$ for the hybrid located at $\mathrm{z,x} = (0.0, 0.0)$. Analogously, the field edge can be visualized for the detector positioned at $\mathrm{z,x} = (0.0, 2.0)$ in figure 114. Here, the shape of spectrum is determined by the interception of the quasi-flat part of the beam halo, before the abrupt fall off. Therefore, the signal amplitude rises with the radial strip location because of their increasing length. A point of inflection can be observed around $\mathrm{r} = 15\,\mathrm{mm}$ where the fall off of the beam takes place and change in the length has no significance. One must also be aware that the discrepancy between the location of the field edge found in the simulations and the experimental results has origins in both the accuracy of the created beam line model and the actual position of the detector in the stand being shifted outwards. The source of the shift is in the design of the shrouds and unavoidable clearance between them, to mitigate their collision at $\mathrm{x} = 0.0\,\mathrm{cm}$, and position of the detector itself inside each of the shrouds. Thus, the introduced systematic transverse shift was estimated to be approximately $\mathrm{x_{shift}} = 10\,\mathrm{mm}$.

6.4.3 Quantitative description of signal-to-dose rate relation per sensor in beam halo monitoring

A quantitative description of analysis performed for the non-invasive concept of proton beam current monitoring is subject to discussion in the two following sub-chapters. Signal integration across the detector was performed per event to find the average amplitude, also referred to as the average amplitude increase per one readout event per sensor. These were obtained for the three tested dose rate values and related to the measured beam intensity by the FC.

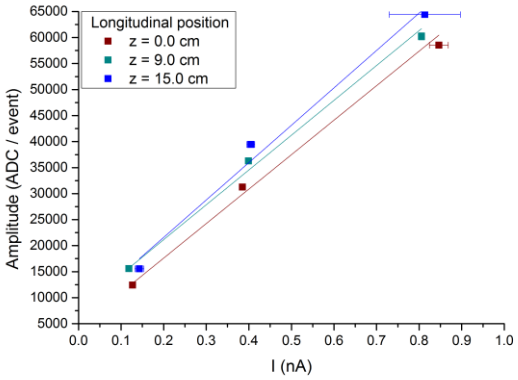

Figure 115: Average increase of the integrated ADC values in the R- sensor No. 2 per readout event versus the proton beam intensity; transverse position x = 0.0 cm.

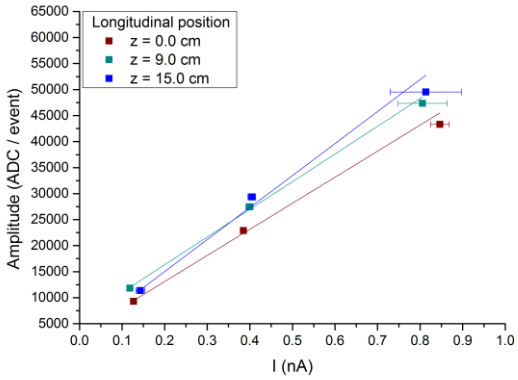

Figure 116: Average increase of the integrated ADC values in the R- sensor No. 4 per readout event versus the proton beam intensity; transverse position x = 0.0 cm.

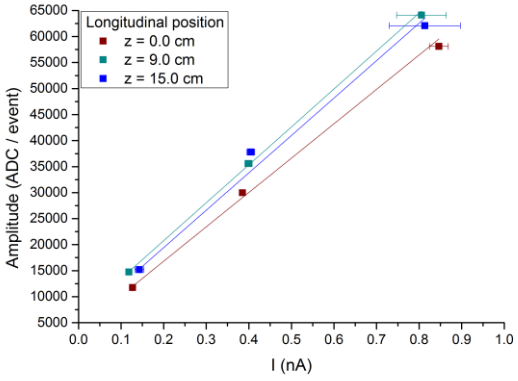

Figure 117: Average increase of the integrated ADC values in the ϕ- sensor No. 76 per readout event versus the proton beam intensity; transverse position x = 0.0 cm.

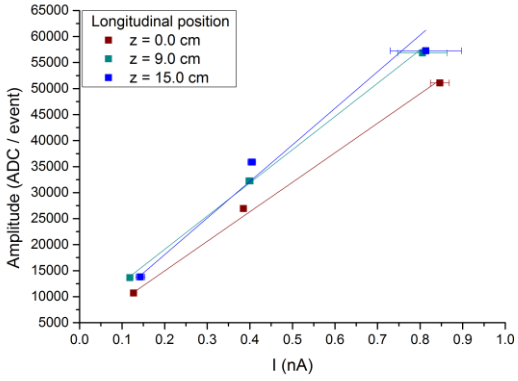

Figure 118: Figure 40: Average increase of the integrated ADC values in the ϕ- sensor No. 77 per readout event versus the proton beam intensity; transverse position x = 0.0 cm.

Table 19: Sensitivity of the LHCb VELO sensors to the dose rate changes at position $z, x = (0.0, 0.0)$ expressed as a slope of a linear data fit.

Sensor No.	z (cm)	x (cm)	Sensitivity (ADC / event)	Sensitivity Error (ADC/ev.) (%)
2	0.0	0.0	66295	4649 7.0 %)
4	0.0	0.0	50134	2973 5.9 %)
76	0.0	0.0	66076	3257 4.9 %)
77	0.0	0.0	56763	2299 (4.0 %)

Table 20: Sensitivity of the LHCb VELO sensors to the dose rate changes at position $z, x = (9.0, 0.0)$ expressed as a slope of a linear data fit.

Sensor No.	z (cm)	x (cm)	Sensitivity (ADC / event)	Sensitivity Error (ADC/ev.) (%)
2	9.0	0.0	66946	3961 (5.2 %
4	9.0	0.0	53215	2333 (4.4 %)
76	9.0	0.0	72906	1291 (1.8 %)
77	9.0	0.0	63857	2050 (1.3 %)

Table 21: Sensitivity of the LHCb VELO sensors to the dose rate changes at position $z, x = (15.0, 0.0)$ expressed a slope of a linear data fit.

Sensor No.	z (cm)	x (cm)	Sensitivity (ADC / event)	Sensitivity Error (ADC/ev.) (%)
2	15.0	0.0	71861	8165 (11.4 %)
4	15.0	0.0	50134	2973 (5.9 %)
76	15.0	0.0	71887	5814 (8.1 %)
77	15.0	0.0	70332	9523 (12.5 %)

The sensitivity of response, expressed as a slope of a linear fit to the experimental points, for both R- and ϕ- sensors demonstrates similar amplitude raise per the readout event. The exception is sensor No. 4, which suffered from signal transfer losses for channels in the radius range between $14\ \mathrm{mm}$ and $21\ \mathrm{mm}$. The estimated values of sensitivity for the consecutive longitudinal locations in the beam propagation direction and $x = 0.0\ \mathrm{cm}$ are summarized in tables 19, 20 and 21. The transverse broadening of the centre of the beam between the locations z = 9.0 cm and z =15.0 cm, discussed earlier, and visualized in figure 75, can be observed in the amplitude increment per event, where the two characteristic curves fitted to the measured points do not show distinctive differences compared to the curve for z = 0.0 cm.

The integrated amplitude values for the sensor per event at the transverse locations x = 1.0 cm and x = 2.0 cm, demonstrate larger differences in amplitude as a function of the longitudinal locations. Here, the detected beam halo regions cover the area of the Gaussian slope and, therefore, experience large charge distribution fluctuations with the travelled distance as opposed to the centre. The sensitivity for $x = 1.0\ \mathrm{cm}$ for either type of the sensors exhibits similar performance and, thus, both R- and ϕ- sensors are equivalent in terms of the

detection efficiency. Summary of the sensitivity values estimated using a linear fit to the experimental points for this region can be found in tables 22, 23 and 24. Accuracy of the slope values for either of the positions $z = 9.0$ cm and $z = 15.0$ cm for three sensors differ by no more that 6 % of the maximum slope value whilst for the sensor No. 4 the damaged sector results in the sensitivity lowered by 20% Here again, measurements demonstrated the largest uncertainty due to the faults in the sector, which was in the high gradient region of the beam. Following the beam divergence, the detectors positioned at $z = 15.0$ cm show the highest sensitivity of response. Similar analysis of performance can be done for the transverse location at $x = 2.0$ cm and in more detail is addressed in the following section. There, the results for the beam halo monitoring as a function of radius and detector type are presented for the transverse distances to $x = 61.95$ mm from the beam axis. Nevertheless, the sensitivity results for the signal integration per sensor area for $x = 2.0$ cm can be visually examined in figures 132 to 135 with a quantitative description is summarized in tables 25 to 27.

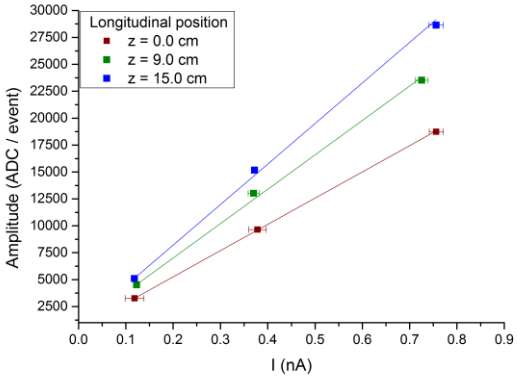

Figure 119: Average increase of the integrated ADC values in the R- sensor No. 2 per readout event versus the proton beam intensity; transverse position x = 1.0 cm

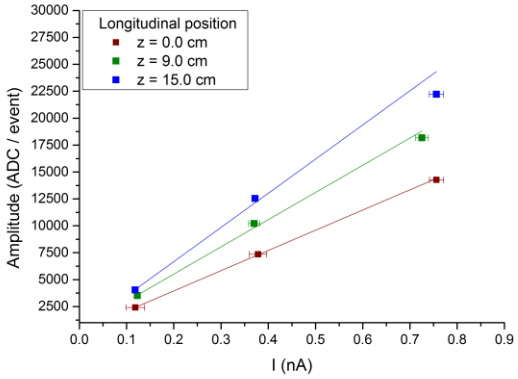

Figure 120: Average increase of the integrated ADC values in the R- sensor No. 4 per readout event versus the proton beam intensity, transverse position x = 1.0 cm.

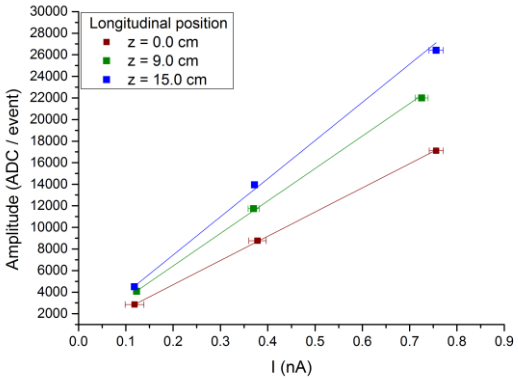

Figure 121: Average increase of the integrated ADC values in the ϕ- sensor No. 76 per readout event versus the proton beam intensity; transverse position x = 1.0 cm.

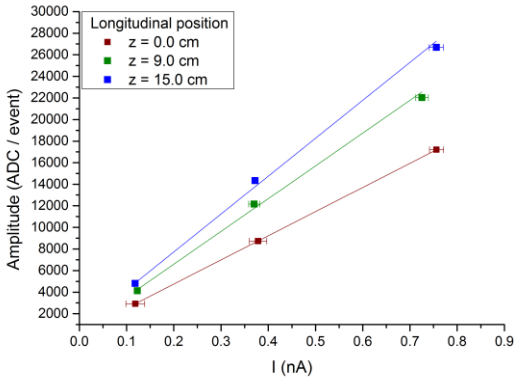

Figure 122: Average increase of the integrated ADC values in the ϕ- sensor No. 77 per readout event versus the proton beam absolute intensity; transverse position x = 1.0 cm.

Table 22: Sensitivity of the LHCb VELO sensors to the dose rate changes at position $z, x = (0.0, 1.0)$ expressed as a slope of a linear data fit.

Sensor No.	z (cm)	x (cm)	Sensitivity (ADC / event)	Sensitivity Error (ADC/ev.) (%)
2	0.0	1.0	24392	162 (0.7 %)
4	0.0	1.0	18778	232 (1.2 %)
76	0.0	1.0	22450	188 (0.84 %)
77	0.0	1.0	22388	26 (0.1 %)

Table 23: Sensitivity of the LHCb VELO sensors to the dose rate changes at position $z, x = (9.0, 1.0)$ expressed as a slope of a linear data fit.

Sensor No.	z (cm)	x (cm)	Sensitivity (ADC / event)	Sensitivity Error (ADC/ev.) (%)
2	9.0	1.0	31962	1085 (3.4 %)
4	9.0	1.0	25287	1415 (5.6 %)
76	9.0	1.0	30112	599 (2.0 %)
77	9.0	1.0	30387	1525 (5.0 %)

Table 24: Sensitivity of the LHCb VELO sensors to the dose rate changes at position $z, x = (15.0, 1.0)$ expressed as a slope of a linear data fit.

Sensor No.	z (cm)	x (cm)	Sensitivity (ADC / event)	Sensitivity Error (ADC/ev.) (%)
2	15.0	0.0	37676	1312 (3.5 %)
4	15.0	0.0	31749	2477 (7.8 %)
76	15.0	0.0	35385	1480 (4.2 %)
77	15.0	0.0	35144	1518 (4.3 %)

The overall accuracy of the method cannot be unambiguously determined due to the lack of synchronisation between the beam bunch arrival time and the readout trigger. For the collected dataset the span of errors is in a range of $0.1\ \%$, for the position $z, x = (15.0, 0.0)$, to $12.5\ \%$ for, $x = (0.0, 1.0)$. To explain the differences we need to refer to figures 126 to 128, which illustrate the distribution of residuals per readout event for a linear and quadratic polynomial fit to the signal integration in sensor No. 77, for which the uncertainty of the slope of the linear fit per event was determined with an error of 0.1 %. It must be emphasised that the distribution of residuals for both types of fits here is convergent. The symmetric distribution of residuals around the x axis, despite visible patterns caused by a superposition of the beam stability fluctuations and the non-synchronised readout of the detector, mean that the assumed linear behaviour and the calculated slope for the integrated average ADC value per event are valid for the model. The symmetrical behaviour reproduces stable beam delivery for this location, where the beam current value can be represented as a constant with either symmetrically scattered measured points or a confined asymmetrical spread, refer to figure 129 for $10\ \mathrm{MU/min}$ and figure 131 for $60\ \mathrm{MU/min}$. Despite the fact that for the dose rate

30 MU/min the current versus time dependence was not stable, the distribution is symmetrical around an average value.

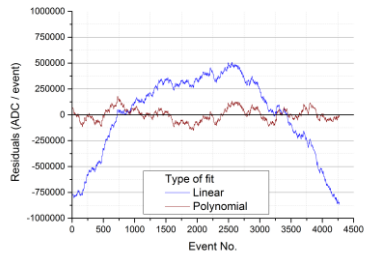

Figure 123: Residuals for the dose rate 10 MU/min and position z, x = (15.0 , 0.0).

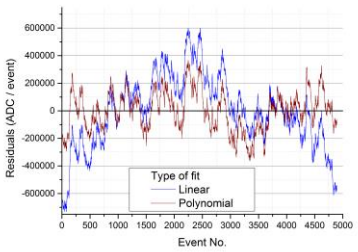

Figure 124: Residuals for the dose rate 30 MU/min and position z, x = (15.0, 0.0).

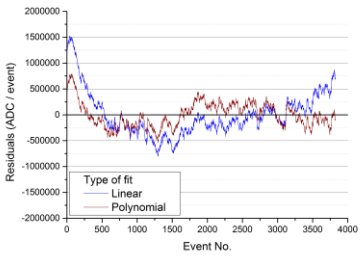

Figure 125: Residuals for the dose rate 60 MU/min and position z, x = (15.0, 0.0).

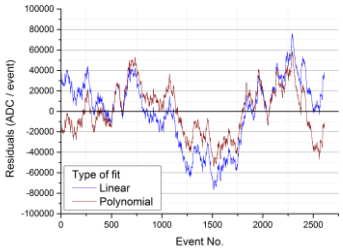

Figure 126: Residuals for the dose rate 10 MU/min and position z, x = (0.0, 1.0).

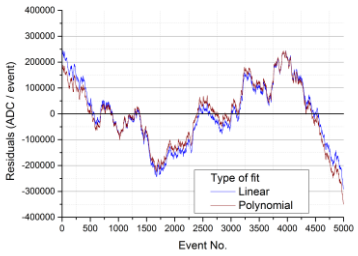

Figure 127: Residuals for the dose rate 30 MU/min and position z, x = (0.0, 1.0).

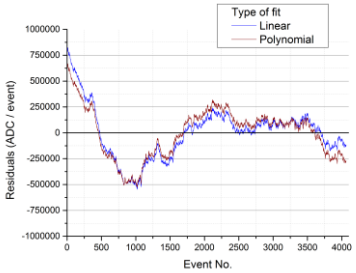

Figure 128: Residuals for the dose rate 60 MU/min and position z, x = (0.0, 1.0).

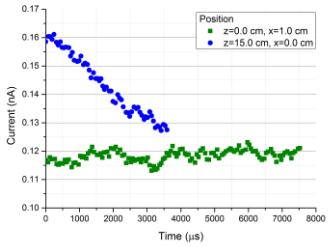

Figure 129: Beam current versus time for the dose rate 10 MU/min corresponding to the above measuremetns.

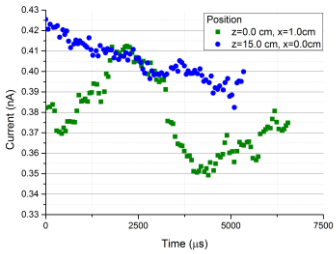

Figure 130: Beam current versus time for the dose rate 30 MU/min corresponding to the above measuremetns.

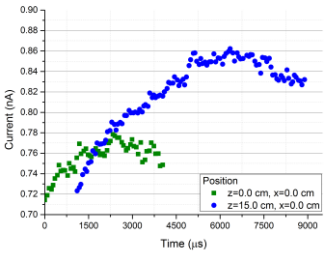

Figure 131: Beam current versus time for the dose rate 60 MU/min corresponding to the above measurements.

The measurement conditions for the location z, x = (15.0, 0.0) demonstrate distinct trend, that is descending for both 10 MU/min and 30 MU/min and ascending for 60 MU/min. This is reflected in the residuals distribution around x axis, where for the linear fit values the magnitude of integrated ADC counts per event can be as much as 70000 ADC different from the trend line. This is cancelled for a quadratic polynomial function fitted to the data. The distribution of residuals becomes symmetric with regards to x axis and reflects only on

variations due to the mismatch in the readout timing. Therefore, further experimental work with the detector should incorporate a high level trigger coupled with the RF of the accelerator during normal run or the FC when calibrating the monitor.

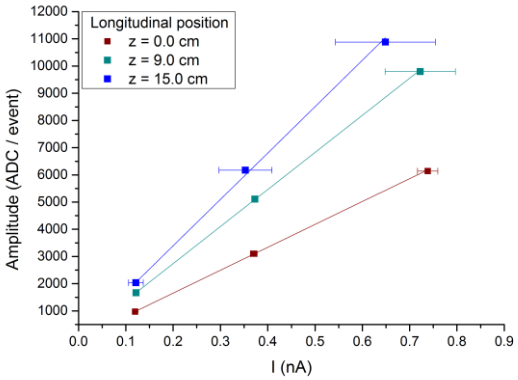

Figure 132: Average increase of the integrated ADC values in the R- sensor No. 2 per readout event versus the proton beam intensity; transverse position x = 2.0 cm.

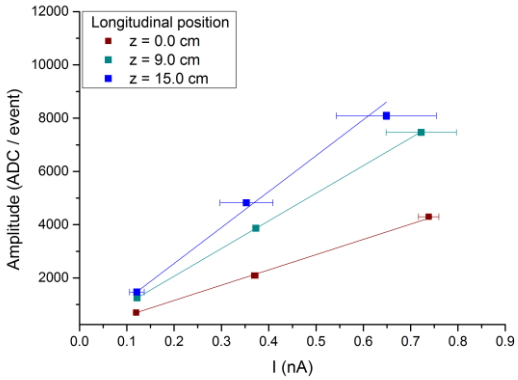

Figure 133: Average increase of the integrated ADC values in the R- sensor No. 4 per readout event versus the proton beam intensity; transverse position x = 2.0 cm.

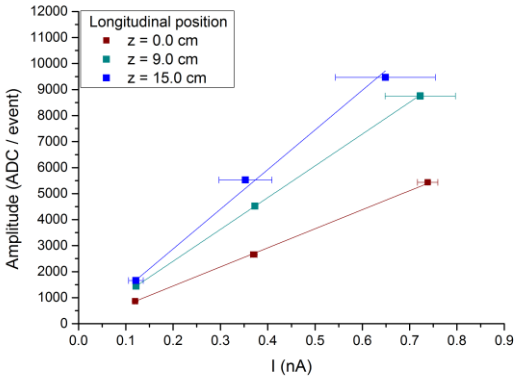

Figure 134: Average increase of the integrated ADC values in the ϕ- sensor No. 76 per readout event versus the proton beam intensity; transverse position x = 2.0 cm.

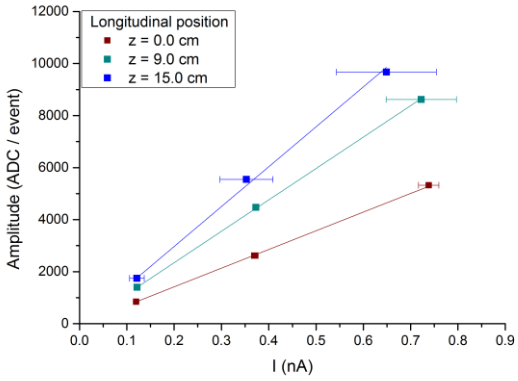

Figure 135: Average increase of the integrated ADC values in the ϕ- sensor No. 77 per readout event versus the proton beam absolute intensity; transverse position x = 2.0 cm.

Table 25: Sensitivity of the LHCb VELO sensors to the dose rate changes at position $z, x = (0.0, 2.0)$ expressed as a slope of a linear data fit.

Sensor No.	z (cm)	x (cm)	Sensitivity (ADC / event)	Sensitivity Error (ADC/ev.) (%)
2	0.0	2.0	8419	75 (3.0 %)
4	0.0	2.0	5731	135 (7.2 %)
76	0.0	2.0	7329	110 (5.5 %)
77	0.0	2.0	7182	92 (4.0 %)

Table 26: Sensitivity of the LHCb VELO sensors to the dose rate changes at position $z, x = (9.0, 2.0)$ expressed as a slope of a linear data fit.

Sensor No.	z (cm)	x (cm)	Sensitivity (ADC / event)	Sensitivity Error (ADC/ev.) (%)
2	9.0	2.0	13630	97 (0.7 %)
4	9.0	2.0	10388	27 (0.3 %)
76	9.0	2.0	12228	34 (0.3 %)
77	9.0	2.0	12080	96 (0.8 %)

Table 27: Sensitivity of the LHCb VELO sensors to the dose rate changes at position $z, x = (15.0, 2.0)$ expressed as a slope of a linear data fit.

Sensor No.	z (cm)	x (cm)	Sensitivity (ADC / event)	Sensitivity Error (ADC/ev.) (%)
2	15.0	2.0	17053	514 (3.0 %)
4	15.0	2.0	13503	976 (7.2 %)
76	15.0	2.0	15252	843 (5.5 %)
77	15.0	2.0	15344	619 (4.0 %)

6.4.4 Signal-to-dose rate relation versus radius in beam halo monitoring

The R- and ϕ-sensors of the LHCb VELO detector were divided into radial bins to investigate the maps of efficiency of the beam intensity monitoring using beam halo versus radius. Sector No. 3 on sensor No. 4 was divided into four equivalent radius length bins, figure 136. Likewise, the surface of the azimuthal sensor No. 77 was divided into two radial bins following to the strips layout as depicted in figure 137.

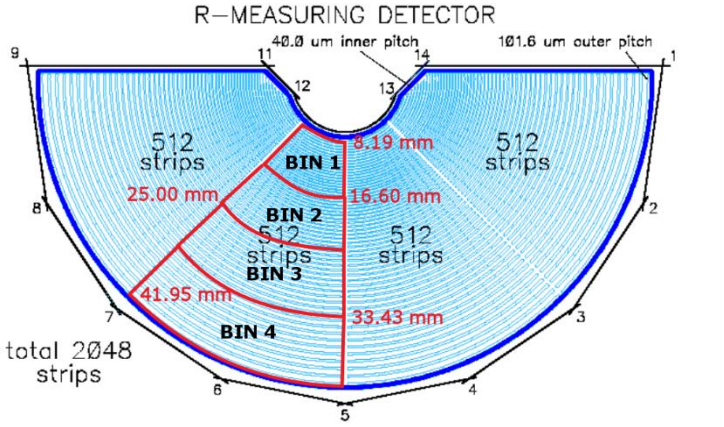

Figure 136: Radial binning in sector 3 of the R-sensor of LHCb VELO detector.

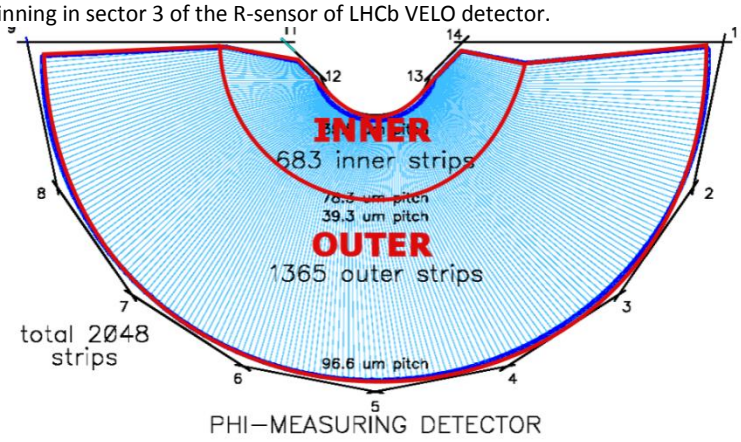

Figure 137: Radial binning in Phi sensor of the LHCb VELO detector.

A slope for a linear fit to the points of average integrated ADC value per radial bin per event was calculated as a function of the dose rate and the experimental location. The signal strength per bin as a function of the transverse and longitudinal locations reflects much stronger on the beam shape than for integration across the whole area of the sensor. At all locations the trend analysis of the amplitude per event demonstrates linear behaviour with varying slope value, decreasing with the radial position of the bin from the beam central axis. This can be followed on the series of images presented below. It should be noted that the linearity of

response is also preserved for the region detecting the lowest proton intensities, at the transverse position $x = 2.0\ cm$, where the 4th bin extended between $53.33\ mm$ and $61.95\ mm$ from the beam axis at $z = 0.0\ cm$. Amplitudes of hits of 200 ADCs were observed and their intensity increased proportionally with the dose rate, figures 155 to 158.

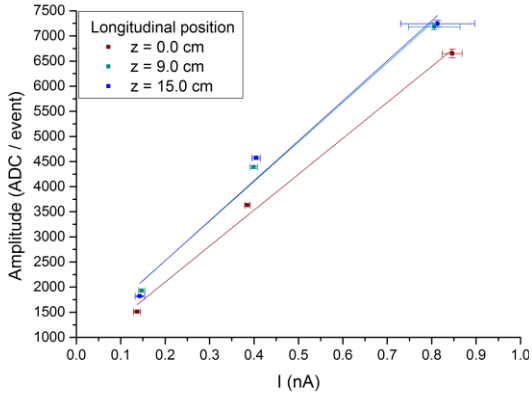

Figure 138: Average increase of the integrated ADC values in the R- sensor No. 4 per readout event versus proton beam intensity in the first 179 radial strips between 8.19 mm and 16.60 mm from the beam axis; transverse position x = 0.0 cm.

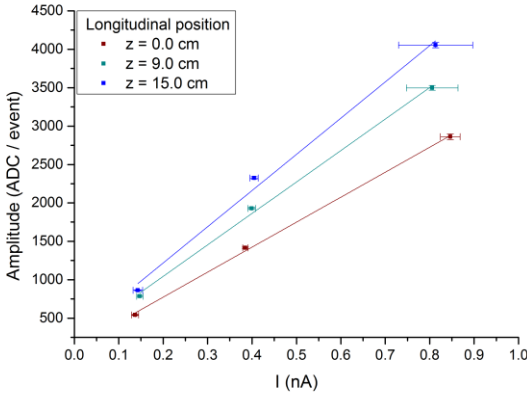

Figure 139: Average increase of the integrated ADC values in the R- sensor No. 4 per readout event versus proton beam intensity in 134 radial strips between 16.60 mm and 25.00 mm from the beam axis; transverse position x = 0.0 cm.

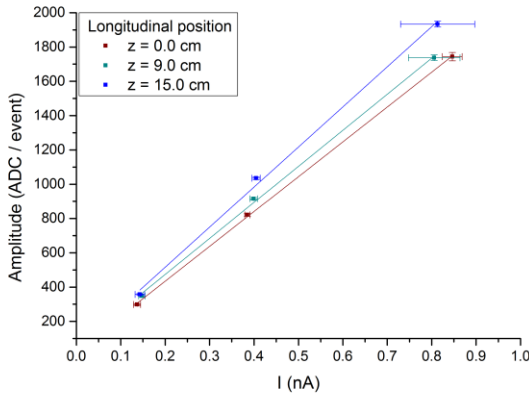

Figure 140: Average increase of the integrated ADC values in the R- sensor No. 4 per readout event versus proton beam intensity in 108 radial strips between 25.00 mm and 33.43 mm from the beam axis; transverse position x = 0.0 cm.

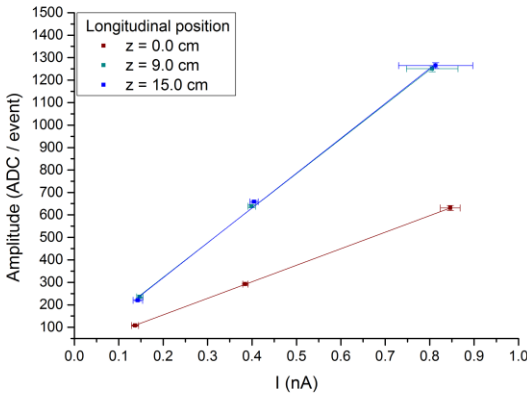

Figure 141: Average increase of the integrated ADC values in the R- sensor No. 4 per readout event versus proton beam intensity in 91 radial strips between 33.43 mm and 41.95 mm from the beam axis; transverse position x = 0.0 cm.

Ultimately, collective maps of sensitivity versus radius, expressed as the geometrical centre of the radial bin location, for both R- and ϕ- sensors were examined and are presented in figures 159 to 162. With reference to the theoretical predictions, the lateral beam spread provides higher sensitivity of measurement with increasing z and for the R-sensor can be approximated with a linear function of up to 53 mm from the beam axis in the transverse location.

The performance of the radial bins in the ϕ-sensor has better sensitivity than in the R-sensor, which is attributable to the length of the strips in the outer sector, where they compensate for the decrease in the beam intensity by integration of hits along a strip.

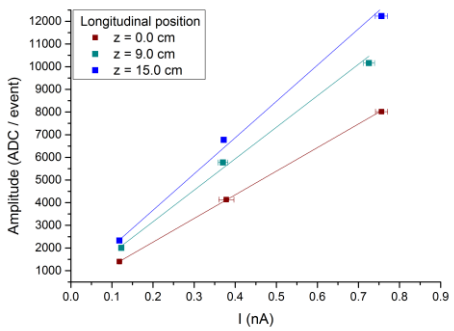

Figure 142: Average increase of the integrated ADC values in the inner strips of the ϕ- sensor No. 77 per readout event versus proton beam intensity; transverse position x = 0.0 cm.

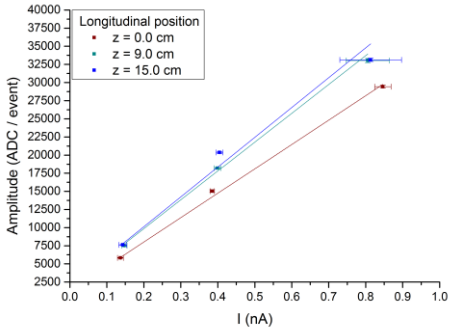

Figure 143: Average increase of the integrated ADC values in the inner strips of the ϕ- sensor No. 77 per readout event versus proton beam intensity; transverse position x = 0.0. cm.

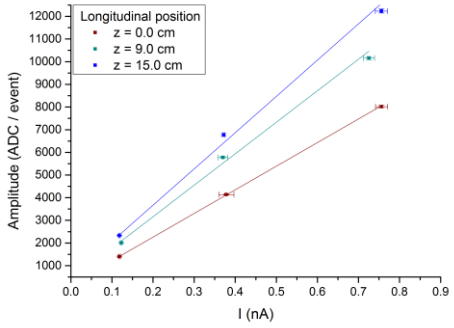

Figure 144: Average increase of the integrated ADC values in the inner strips of the ϕ- sensor No. 77 per readout event versus proton beam intensity; transverse position x = 1.0 cm.

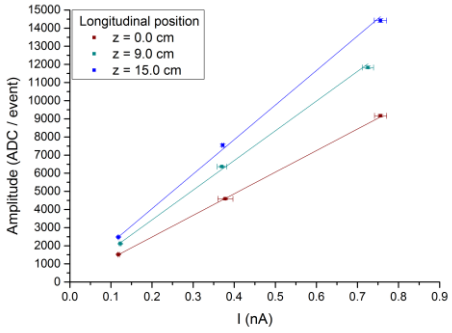

Figure 145: Average increase of the integrated ADC values in the inner strips of the ϕ- sensor No. 77 per readout event versus proton beam intensity; transverse position x = 1.0. cm.

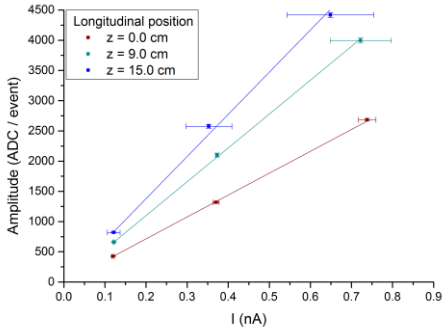

Figure 146: Average increase of the integrated ADC values in the inner strips of the Phi- sensor No. 77 per readout event versus proton beam intensity; transverse position x = 2.0 cm.

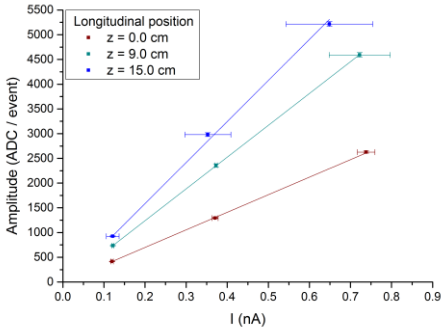

Figure 147: Average increase of the integrated ADC values in the inner strips of the Phi- sensor No. 77 per readout event versus proton beam intensity; transverse position x = 2.0. cm.

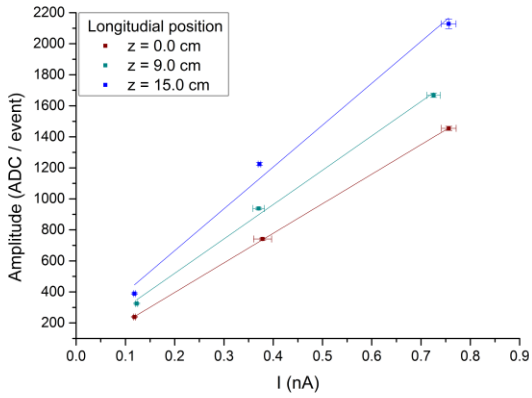

Figure 148: Average increase of the integrated ADC values in the R- sensor No. 4 per readout event versus proton beam intensity in the first 179 radial strips between 18.19 mm and 26.60mm from the beam axis; transverse position x = 1.0 cm.

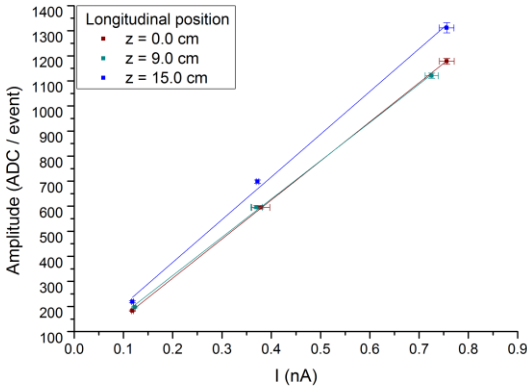

Figure 149: Average increase of the integrated ADC values in the R- sensor No. 4 per readout event versus proton beam intensity in 134 radial strips between 26.06 mm and 35.00 mm from the beam axis; transverse position x = 1.0 cm.

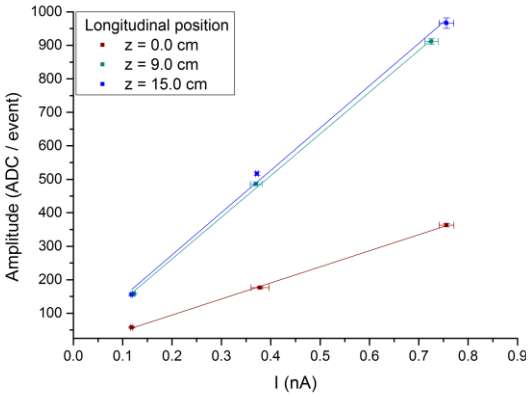

Figure 150: Average increase of the integrated ADC values in the R- sensor No. 4 per readout event versus proton beam intensity in 108 radial strips between 35.00 mm and 43.43 mm from the beam axis; transverse position x = 1.0 cm.

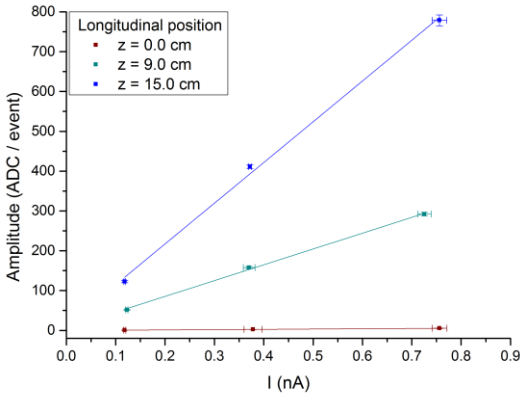

Figure 151: Average increase of the integrated ADC values in the R- sensor No. 4 per readout event versus proton beam intensity in 91 radial strips between 43.43 mm and 51.95 mm from the beam axis; transverse position x = 1.0 cm.

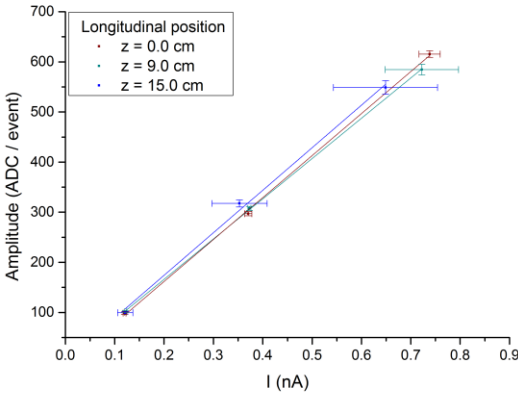

Figure 152: Average increase of the integrated ADC values in the R- sensor No. 4 per readout event versus proton beam intensity in the first 179 radial strips between 28.19 mm and 36.60mm from the beam axis. The transverse position x = 2.0 cm.

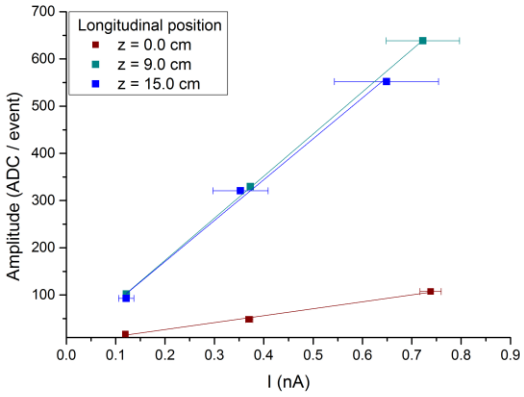

Figure 153: Average increase of the integrated ADC values in the R- sensor No. 4 per readout event versus proton beam intensity in 134 radial strips between 36.06 mm and 45.00 mm from the beam axis; transverse position x = 1.0 cm.

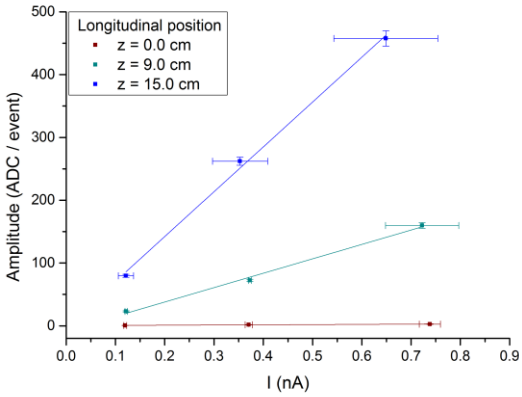

Figure 154: Average increase of the integrated ADC values in the R- sensor No. 4 per readout event versus proton beam intensity in 108 radial strips between 45.00 mm and 53.43 mm from the beam axis; transverse position x = 2.0 cm.

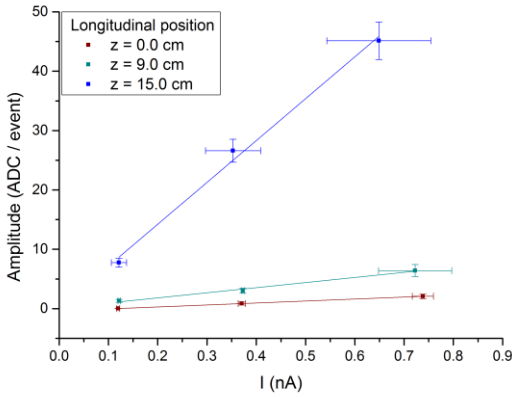

Figure 155: Average increase of the integrated ADC values in the R- sensor No. 4 per readout event versus proton beam intensity in 91 radial strips between 53.43 mm and 61.95 mm from the beam axis; transverse position x = 2.0 cm.

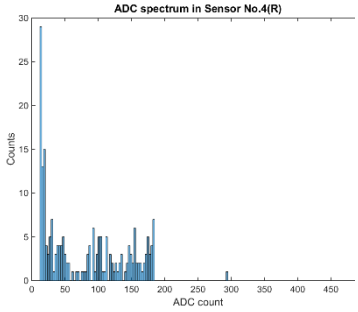

Figure 156: ADC spectrum integrated across the readout events in the R- sensor No. 4 for in the 91 radial strips between for the dose rate 10 MU recorded in the fourth radial bin between 53.43 mm and 61.95 mm from the beam axis; longitudinal position $z = 0.0\,\mathrm{cm}$, transverse position x = 2.0 cm.

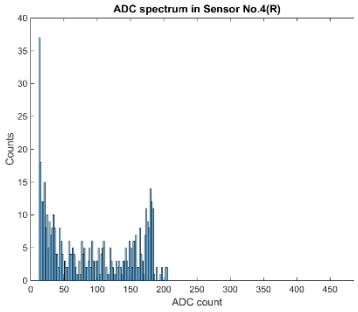

Figure 157: ADC spectrum integrated across the readout events in the R- sensor No. 4 for in the 91 radial strips between for the dose rate 30 MU recorded in the fourth radial bin between 53.43 mm and 61.95 mm from the beam axis; longitudinal position $z = 0.0\,\mathrm{cm}$, transverse position x = 2.0 cm.

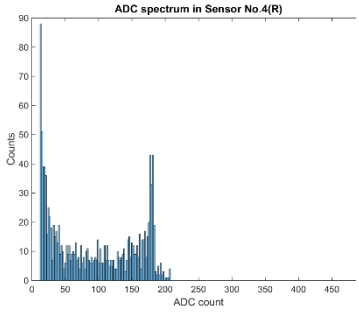

Figure 158: ADC spectrum integrated across the readout events in the R- sensor No. 4 for in the 91 radial strips between for the dose rate 60 MU recorded in the fourth radial bin between 53.43 mm and 61.95 mm from the beam axis; longitudinal position $z = 0.0\,\mathrm{cm}$, transverse position x = 2.0 cm.

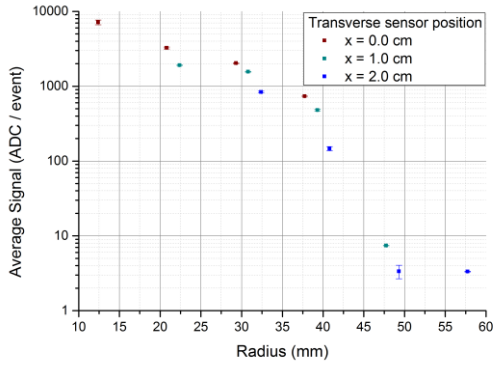

Figure 159: Average signal per event in the R-sensor of the LHCb VELO detector in consecutive radial bins versus transverse location; the longitudinal position $z = 0.0$ cm.

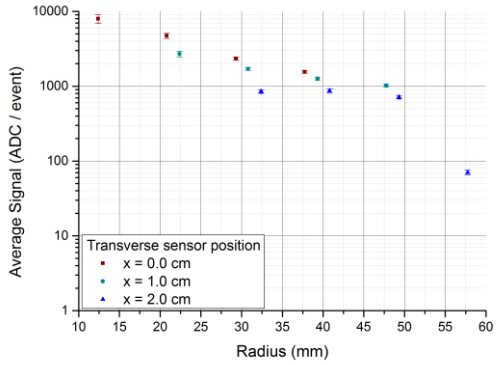

Figure 160: Average signal per event in the R-sensor of the LHCb VELO detector in consecutive radial bins versus transverse location; the longitudinal position $z = 15.0$ cm.

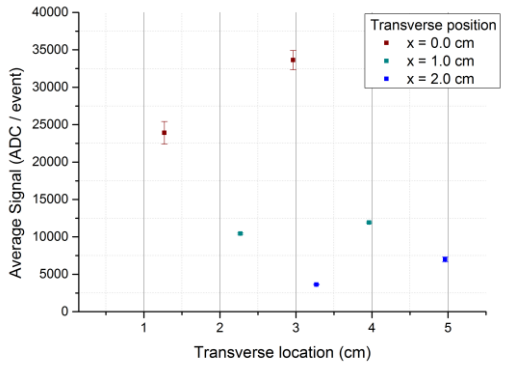

Figure 161: Average signal per event in the ϕ-sensor of the LHCb VELO detector in the inner and outer bins versus their transverse location. The radial position for each pair of points belongs respectively to the inner region on the left and the outer region on the right. The longitudinal position $z = 0.0$ cm.

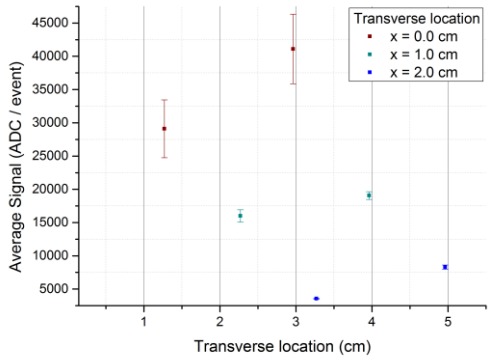

Figure 162: Average signal per event in the ϕ-sensor of the LHCb VELO detector in the inner and outer bins versus their transverse location. The radial position for each pair of points belongs respectively to the inner region on the left and the outer region on the right. The longitudinal position $z = 15$ cm.

Chapter Summary

In this chapter a non-invasive beam current monitor for a medical proton beam at CCC was developed and tested. The detector uses silicon multi-strip technology in the form of the LHCb VELO detector, which has a beneficial semi-circular sensor design with a half-iris in the middle that allows the core of the beam to pass though without any distortions to its profile or energy. The architecture of the detector also means that it provides radial distributions of the beam halo. In the measurements presented in this chapter, silicon sensors measured the beam

halo at different locations in the plane perpendicular to the beam propagation direction for several distances along the z axis. The non-invasive beam measurement method is based on establishing the correlation between the measured signals from the VELO detector, integrated across the detector strips in a sensor per a readout event, with an average value of the absolute beam intensity measured at the treatment isocentre by a dedicated Faraday Cup.

Essential detector modifications were refined to operate the VELO detector in an environment it was not designed for, i.e. outside of the LHC. A set of optimal working conditions was found and verified to permit stand-alone operation of the detector in water vapour condensation-free conditions at a low temperature during measurements with the proton beam in ambient air.

The chapter also covered aspects of the Faraday Cup commissioning with a proton beam. The performance of the detector was assessed and proved to remain constant in a range between 0.0 V and -1000 V used to suppress electrons emitted from the surface of the beam stopper with kinetic energies below $1\ \mathrm{keV}$ when measuring the proton beam intensity. The readout circuit consisted of a picoammeter, which was used to establish relation between the clinically used monitor units and the absolute average beam intensity values. For the largest beam intensities the uncertainty associated with the measurement was found to be of 10 %, which was later reflected in the accuracy of the obtained results from the VELO detector.

The signal rise in the R-sensor of the VELO detector was then studied using FLUKA to find an estimate of the amplitude per strip per a readout event as a function of beam halo intensity. The amplitudes were obtained for three different monitor unit values exercised in the test as well as for a combination of the detector locations in both the perpendicular and parallel axes to the beam propagation direction. It was shown that no saturation effects from the 60 MeV proton beam are expected in the detector. However, it must be highlighted that the calculated amplitudes per bunch do not accurately reflect the maximum measured signal per strip. This limitation is associated with the applicability of the Monte Carlo methods, which are designed for assessment of interactions for a large number of particles building their statistical representation. The actual energy deposition from a bunch consisting of 200 protons is scarce and much more localised around the path length in a vicinity of a single strip. As a result, the maximum values of signal per strip per bunch remained unknown. At the same time, the radial proton intensities, approximated by a Gaussian distribution, was detected in the R-sensor and

was found to be in agreement with the results of the modelling of the beam transport described in chapter 5.

The chapter also summarized results of the tests of the non-invasive beam current monitor with the proton beam at CCC. The response of the detector was studied in a function of the average intensity of the beam and detector position. Noise level studies in the detector were performed to obtain an amplitude cut-off threshold to suppress false hits associated with the above noise levels and along with low amplitudes of hits. This enhanced the relative visibility of the number of proton hits with high amplitudes in the spectrum in each of the sensor. Ultimately, the dependence between the average amplitude per sensor per bunch was found as a function of absolute beam intensity. Some expected distortions were observed, that affected the linear trend in the above relation. For this reason, non-linarites of the signal can be observed and are limited by using the average values. Any instabilities of the beam current during the data collection, as highlighted in the data analysis that cannot be expressed with a constant around which the beam intensity oscillations average out lead to loss of the ADC count proportionality with the changing monitor units value.

Additionally, radial sensitivity of the method was explored to look into efficiency of the non-invasive beam monitoring for different regions of the beam halo as a function of distance from the beam axis. For these positions, the sensitivity demonstrated linear behaviour even for the farthest locations from the beam axis, which were beyond the edge of the beam halo produced by the scattering foils and the aperture of the modulator box. With regard to chapter 5, only a few particles per readout event can be found in this frame. Therefore, the radial efficiency of the R-sensor drops faster than for the Φ-sensor, where the length of radially oriented strips compensates for the decrease of the radial intensity of protons, unlike for the horizontally oriented strips in the R-sensor.

7. CONCLUSIONS

7.1 Summary

The primary objective of the project was to develop a non-invasive beam current monitor for a medical accelerator based on the LHCb VELO detector and test it with a proton beam at Clatterbridge Cancer Centre. In order to achieve the set goal, a number of sub-projects had to be completed, which involved a few other detectors and were described in chapters 3 to 5. The design paths optimising the performance of the mentioned monitors were presented. Additionally development of necessary hardware and software supporting their operation were outlined. A number of intermediate steps were followed to provide information about many physics processes, which allowed for decisions to be made on the final designs of the respective elements of the set-up. These included the design of a Faraday Cup, which geometrical arrangement and choice of material were supported by literature and numerical studies, integration of the LHCb VELO detector with the existing beam line, where the operation of the detector took place outside the environmental conditions it was designed for, and the design and test of monitor based on a scintillating screen to perform quadrupole variation scans for the beam dynamics studies. Despite the fact, that the set up was optimised for operation at the Clatterbridge Cancer Centre, it can be used at other proton therapy centres with possibly minute adjustments required.

In Chapter 2, the principles of charged particle interactions with matter were described with a focus on the benefits they have in cancer treatment compared to conventional radiotherapy with photon radiation. The theory describing of energy deposition from protons in matter was explained and linked with their clinical applications. A brief introduction into the beam delivery techniques in proton therapy was given, including types of used accelerators, and the parameters characterising the clinical beam at CCC were presented.

In Chapter 3, various beam current monitoring methods for accelerators were introduced and a justification for the choice of a Faraday Cup was given. The design of the detector was brought forward as a coaxial transfer line to support large bandwidth of signal transfer, where the transport of a transverse electro-magnetic mode (TEM) does not have any upper or lower limit. The choice of geometry and materials were also outlined. Impedance matching for the detector was proposed to equalise the impedance of the FC with the readout

transfer line of $Z = 50\ \Omega$, which reduction of the detector dimensions in size and weight. At the same time, the diameter of the beam collector cavity had to preserve its dimensions due to the size of the treatment beam at the isocentre, $\Phi_{\mathrm{beam}} = 3.6\ \mathrm{cm}$, where the beam current was measured. Theory of the reflections at the impedance mismatch was introduced to explain the results of the FC tests with nanosecond-long pulses delivered by a pulse generator during the bandwidth tests. A remedy was proposed to correct for the impedance mismatch by introducing compensating resistances. The matching was incorporated for possible future developments of the proposed method, when bunch-to-bunch correlation of signals will be introduced. For the time being, the tests of signal transfer properties of the FC were done without impedance matching and the results have shown that the bandwidth of the designed monitor allows for investigation of single bunches down to a width of 3.1 ns, which constituted the shortest available electric pulses from the applied pulse generator. In the operation of the FC as a part of the proposed non-invasive monitor, the charge collected by the beam stopper was integrated by a coupled picoammeter in $50\ \mu\mathrm{s}$ intervals and impedance matching was not necessary. The detector geometry was also optimised in terms of charge measurement losses associated with proton-induced particle emission from the surface of metals when measuring with a beam. Literature studies on the theory of particle emission were presented first and were followed by results of numerical studies using FLUKA, which showed that the extent of charge escaping from the FC is of $0.16\ \%$ for the beam current value of $1.6\ \mathrm{nA}$ for the suggested geometry.

In Chapter 4, the technology of the LHCb VELO detector was presented and the beneficial architecture of the sensors was linked with the requirements of the proposed detector application as a stand-alone non-invasive beam current monitor. A number of necessary adjustments were described in terms of the hardware and software adaptations to permit its intended use. These comprised of an assembly of new signalling and powering cable sets, PCB boards and a design of a new infrastructure for incorporating the detector readout. Software adjustments comprised of modifications to TELL1 boards firmware to tailor the timing properties of the detector to the modified electronics layout. Adaptations of the existing VETRA data analysis code, created at CERN, were necessary to enable data analysis in the experiment. A dedicated motorised stand was devised and customised software written to provide a precise alignment of the detector with respect to the beam in its three cardinal axes. Ultimately, for the first time use, the VELO detector was used outside a vacuum with the sensors still kept at a low temperature for a prolonged period of time. Therefore, a dedicated cooling system was applied

together with dry air shrouds, which supported its operation in air without any damage from the electronics because of water condensation.

In Chapter 5, a summary of determination of beams transverse dimensions for accelerators was presented with a focus on quadrupole variation scans (QVS), which were performed at CCC. The QVS scans and the beam dynamics studies were a joint venture between the author of the thesis and the collaborators at the TERA Foundation at CERN and the Cockcroft Institute in the UK. The aim of the studies was to determine the beam Twiss parameters, which were used for further continuation of numerical investigations in FLUKA on the beam transport in the treatment beam line at CCC. The formation of the beam halo, its transverse dimensions and the intensities of the beam halo were calculated for the integration space of the LHCb VELO detector. The beam halo extent was found and had a Gaussian-like core with a sharp fall-off at a radius of 6.8 mm from the beam axis, formed by the aperture of the modulator box in the beam line structures. The obtained beam intensity maps were used to estimate expected amplitude values measured in the VELO detector and were presented in the next chapter.

In Chapter 6, the experimental results generated during the first run of the prototyped non-invasive beam current monitor were presented and preceded by a description of a set of parameters determined to provide for a safe operation of the VELO detector in air at low temperatures. Results of the expected amplitudes from the VELO detector were given for as a function of proton beam currents and positions in the chosen integration area. The sensitivity of measurements showed comparable values for both the R- and ϕ- sensors when integration of signals for all the strips in a sensor was performed per a readout event. The values of sensitivity were a function of the distance from the beam axis in a plane perpendicular to the beam direction and increased with increasing beam divergence in the beam propagation direction. Sensitivity was also assessed in smaller 1 cm-steps from the beam axis and showed linearity of response for the whole range of radii of up to the last position at 62 mm. Non-linearities in the average value of signal in the VELO detector per sensor per a readout event as a function of the average value of the measured current were explained. They limit application of the detector for a medical accelerator, unless synchronisation of the accelerator and the VELO detector readout is implemented.

The proposed method permits measurements to be taken of the intensities of protons on a medical accelerator without introducing disruptions to the energy or transverse dimensions

of the beam. The outlined design of the set up may be used for the calibration of the detector at any other similar treatment centre once refinements of the method have been applied.

7.2 Future Developments

The subject of the non-invasive beam current monitoring for a medical accelerator, described in this thesis, has not been exhausted and more work can be undertaken. The presented results constitute a proof of principle of the method and are based on the first ever run of the monitor. At the current state of the art, the monitor cannot be implemented as an independent monitor until a number constraints are removed and further modifications and refinements to the detector have been implemented. The potential additional applications include daily Quality Assurance of the accelerator in terms of beam position, stability of the treatment delivery and online beam dose monitoring.

The datasets from the preliminary run of the monitor were analysed off-line and no online software tools were available to the time of the experiment, what restricts the application of the detector as an on-line monitor. Therefore, software improvements can be implemented to enable data analysis in real-time.

The accuracy of the integrated average amplitude per sensor per a readout event, referred to as sensitivity, corresponded to a specific average beam current value and was described by a range of uncertainties reaching as much as 15 % of the calculated sensitivity value, which disqualifies the current design from implementation as a part of a medical device. For comparison, accuracy of ionisation chambers used in radiotherapy, expressed as uncertainty of measurement, is in a range between 0.7 % and 1.5 %. The lowest uncertainty found during measurements with the non-invasive monitor was 0.01 %. This happened for the exposure conditions, when the average value of the beam current could be represented by a constant, around which the beam intensity oscillations took place. Thus the measured ADC values preserved their proportionality to the average beam current. This provides an indication for achievable uncertainty levels of the method and must be verified experimentally in any provisioned future tests. Therefore, the detector triggering must be enabled and coupled with either the FC readout, during commissioning of the detector, or with the RF generators of the accelerator to provide for the VELO detector with time information and synchronise the data readout with a bunch arrival.

The bunch-to-bunch operation of the monitor allows space for improvements of the Faraday Cup. Firstly, the impedance matching should be applied to minimize any distortions of the signal originating reflections. A dedicated wide bandwidth trans-impedance amplifier should be implemented to examine shapes and measure charge values in single bunches. A dedicated software could also be developed to pass a trigger signal to the VELO detector for commencing the readout.

Ultimately, studies should be made to simplify the electronics and architecture of the VELO detector, which is very advanced for the proposed application. Additionally, the current system architecture is space consuming and, alternatively, other less complicated detectors should be also envisaged for implementation.

8. GLOSSARY

AC Alternating Current

ADC Analogue-to-Digital Count

BNC Bayonet-Neill-Concelman connector

BW Bandwidth

CAT 6 Category 6 Cable

CCC Clatterbridge Cancer Centre NHS Trust based in Bebington on Wirral, United Kingdom

CCD Charge Coupled Device

CERN European Organisation for Nuclear Research

CSDA Continuous Slowing Down Approximation

CsI(Tl) Caesium Iodine doped with Thallium

CST Computer Simulation Technology

DAQ Data Acquisition

DC Direct Current

DN100CF ConFlat Flange with a diameter D=100 mm

ECS Experiment Control System

FC Faraday Cup

FEA Finite Element Analysis

FPGA Field Programmable Gateway Array

FWHM Full Width at Half Maximum

HEP High Energy Physics Group

HIT Heidelberg Ion Therapy Centre

HLT High Level Trigger

HV High Voltage

I^2C A multi-master, multi-slave, single-ended, serial computer bus protocol invented by Philips Semiconductor

LHC Large Hadron Collider

LHCb VELO (VELO) LHCb Vertex Locator

LINAC Linear Accelerator

LV Low Voltage

MCS Multiple Coulomb Scattering

MIP Minimum Ionising Particle

QUASAR Group Quantum Systems and advanced Accelerator Research Group

PEEK Polyether Ether Ketone

PPIC Parallel Plate Ionisation Chamber

PTFE Polytetrafluoroethylene

RF Radio Frequency

SCL Serial Communication Language

SMU Source-Measurement Unit

STFC Science and Technology Facilities Council

TCS Time Control System

TERA TERA Foundation

TPG Thermal Pyrolytic Graphite

UHV Ultra High Vacuum

VCTS VELO Thermal Control System

VITON Synthetic Rubber by DuPont

9. ACKNOWLEDGMENTS

I would like to express my gratitude and say sincerely “Thank you!” to my supervisor, Prof. Dr. Carsten P. Welsch, who throughout many years supported my scientific and personal development, indicating the directions which allowed for creation of this thesis.

The generous support of my work, leading to this thesis completion, were made possible by a DITANET Marie Curie fellowship, funded by the European Commission under a contract PITN-GA-2008-215080 and the Cockcroft Institute Core Grant No. ST/G008248/1.

Hereby, I would like to say how grateful I am to Team at the Douglas Cyclotron Department at the Clatterbridge Cancer Centre, especially to Andy Wray, Brian Marsland and Ian Taylor, for their invaluable kindness and effort in helping to run the experimental work, and to Andrzej Kacperek for his support in organizing the measurements and his keen interest in the subject. Quite a few sleepless nights spent measuring on the accelerator will never be forgotten. Most of all, I will keep in my memories the good time spent together at endless tea time gathering accompanied by all sorts of sweets and cakes. I believe that is also a highlight of Alberto Degiovanni’s visit when performing the QVS measurements.

Thank you to the High Energy Group at the University of Liverpool, in particular, to Tony Smith, Karol Hennessy and Gianluigi Casse, who supported my work and helped me in making the LHCb VELO detector run at CCC, outside both the testing laboratory at the University and experimental sites at CERN.

I am grateful to Glenda Wall whose motherly heart was priceless in managing the DITANET project, joining the fellows together. Her never ending smile and fabulous Northern sense of humor could always brighten the day.

I would also like to express how grateful I am to Lee Devlin, who was always ready to give me a hand with shifting, repairing, setting up and dismantling of the experimental bits and pieces. With the numerous failures that the set-up suffered from, Lee he was kept really busy and stopped being afraid of experimental work. All in all, things were sometimes broken down so badly, that it was hard to imagine anything more could happen.

It is impossible to say how wonderful support I was given by many employees of Daresbury Laboratory (STFC) and the Cockcroft Institute. It would take a long list to mention everyone, therefore, I am saying thank you all but addressed to each one personally.

Thank you to all the members of the QUASAR Group based both at the Cockcroft Institute and outside it, fellows of DITANET, LA3NET and OPAC Marie Curie networks and my wonderful friends at the Cockcroft Institute, Alexandra Alexandrova, Lee Devlin and Chris Edmonds for fabulous moments spent together and joy we shared.

Finally, I would like to thank my beloved mother, Bożenna, members of my family and my friends, here in the UK and back in Poland, for their support, concerns and presence every single day along the path of this PhD. To you and myself I dedicate this work.

10. REFERENCES

[1] *On a new kind of rays,* W. Roentgen,Nature53: 274 – 276 (1896)

[2] *Radiation Oncology Physics: A handbook for teachers and students*, E. Podgorsak, International Atomic Energy Agency, Austria Vienna 2005

[3] *Techniques for Nuclear and Particle Physics Experiments*, W.R. Leo, Springer-Verlag, Germany Berlin 1994

[4] *New Technologies in Radiation Oncology*, W. Schlegel, T. Bortfeld, A.L. Grosu, Medical Radiology – Radiation Oncology, Springer, Germany Munich 2006

[5] *Protontherapy of eye tumours in the UK: A review of Treatment at Clatterbridge*, A. Kacperek, Applied Radiation and Isotopes 67 (2009) 378-386, Elsevier 2008

[6] World Cancer Research Fund International: http://www.wcrf.org/

[7] *Proton Beam Therapy*, Santosh Yajnik, Springer, USA New York 2013

[8] *A LHCb VELO module as beam quality monitor for proton therapy beam at the Clatterbridge Centre for Oncology*, G. Casse et al. , Materials obtained from G. Casse at HEP University of Liverpool

[9] *LHCb Technical Design Report*, CERN/LHCC 2001-0011, CERN Geneva 2001

[10]*Proton Therapy Physics*, H. Paganetti et al., CRC Press Taylor & Francis Group, USA Boca Raton 2012

[11] *Proton Range-Energy Tables, 1keV-10GeV: Energy Loss, Range, Path Length, Time-of-flight, Straggling, Multiple Scattering and Nuclear Interaction Probability*, J. Janni, Atomic Data and Nuclear Data Tables 27, 147-339, American Press, USA 1982

[12] *A comprehensive study of the most likely path formalism for proton-computer tomography*, B. Erydelyi, Physics in Medicine and Biology 54 (2009) 6095-6122, IOP Publishing 2009

[13]Particle Data Group: http://pdg.lbl.gov/

[14] *Stopping Powers and Ranges for Protons and Alpha Particles*, International Commission on Radiation Units and Measurements Report No. 49, USA Maryland 1993

[15]Scanditronix Medical AB documentation.

[16]*Proton and Carbon Ion Therapy*, T. Lomax et al., CRC Press Taylor and Francis Group, USA Boca Raton 2012

[17]*Beam dynamics for* cyclotrons, F. Chautard, CERN Accelerator School Proceedings: cas.web.cern.ch

[18]*Injection and extraction from cyclotrons*, W. Kleeven, CERN Accelerator School Proceedings: cas.web.cern.ch

[19]*Assessing the suitability of a medical cyclotron as an injector for an energy upgrade*, J. A. Clarke et al., European Particle Accelerators Conference Proceedings (1998) 2374-2376, CERN website: accelconf.web.cern.ch

[20]*Monte Carlo modelling of a clinical proton beam-line for the treatment of ocular tumours*, C. Baker, Nuclear Instruments & Methods in Physics Research A 562 (2006) 1005-1008, Elsevier 2006

[21] *Proton therapy of eye tumours in the UK: A review of treatment at Clatterbridge*, A. Kacperek, Applied Radiation and Isotopes No. 67 (2009): 378-386, Elsevier 2009

[22] *Cyclotron MC60PF Technical Specification*, Scanditronix Medical, Ver. 1, document obtained from IBA Europe, Netherlands

[23] *Beam Instrumentation and diagnostics*, P. Strehl, Springer-Velrag Berlin Heidelberg, The Netherlands 2006

[24]*Lecture notes on beam instrumentation and diagnostics*, P. Forck, Joint University Accelerator School, CERN 2008

[25] *Statistical Physics*, F. Mandl, John Wiley & Sons. , England London 1988

[26]*Microwave Engineering*, D. Pozar, John Wiley & Sons, USA New York 1998

[27] *A high power Faraday Cup to measure extracted beam current from the BATES South Hall Ring*, J. Shaw, IEEE (1998) 2274-2275

[28]*Stopping Powers and Ranges for Protons and Alpha Particles*, ICRU Report No. 49, USA Maryland 1993

[29]*A Faraday Cup with High Frequency Response for a 200 MeV LINAC proton Beam*, M. Zucker, IEEE Particle Accelerator Conference Proceedings PAGE 1270, US San Francisco 1991

[30]*Faraday Cup with nanosecond response and adjustable impedance for fast electron beam characterisation*, Jing Hu, Review of Scientific Instruments 82, 0703504 (2011), US American Institute of Physics 2011

[31]*A very wide bandwidth Faraday Cup for measuring Gigahertz structure on ion beams with velocities down to β < 0.01*, Proceedings of the Linear Accelerators Conference 1990, US Albuquerque 1990

[32]*Particle induced electron emission II*, D. Hasselkamp, Springer Verlag , Germany 1992

[33]*Influence of charge changing process on proton induced electron emission from polycrystalline aluminium*, Elsevier Nuclear Instruments and Methods in Physics Research B 203 (2003) 36-40, 2003

[34]*Particle-impact Induced Electron Ejection from Surfaces*, E. Thomas, IAEA Nuclear Data Section INDC(NDS)-322, Austria Vienna 1995

[35]*Proton Range – Energy Tables, 1keV – 10GeV: Energy Loss, Range, Path Length, Time-of-Flight, Straggling, Multiple Scattering, and Nuclear Interaction Probability*, J.F. Janni et al., Atomic Data and Nuclear Data Tables No. 27, 147-339, UK 1982

[36] *FLUKA – a multi-particle transport code*, A. Ferrari, CERN-2005-010, Switzerland Geneva 2011

[37]*The Determination of Absorbed Dose in a Proton Beam for Purposes of Charged – Particle Radiation Therapy*, L. Verhey, Radiation Research No. 79 34-54, UK 1979

[38]*Faraday cup dosimetry in a proton therapy beam without collimation*, E. Grussel, Physics in Medicine and Biology vol. 40 1831-1840, UK 1995

[39]*Proton beam dosimetry: A comparison between the Faraday cup and an ionization chamber*, R. Cambria, Physics in Medicine and Biology vol. 42 1185–1196, UK 1997

[40]*Beam diagnostics for low energy beams*, J.Harasimowicz, Physical Review Special Topics – Accelerators and Beams 15, 122801, APS 2012

[41]*Computer Simulation Technology*: https://www.cst.com/

[42] LEWVAC components: http://www.lewvac.co.uk/

[43]*Bertan 205B high voltage power supply*, Spellman High Voltage Electronics Corporation: http://www.spellmanhv.com/

[44]*Solid Edge*, Siemens: http://www.plm.automation.siemens.com/

[45]*HiPace80 Turbo pump manual*, Pfeiffer Vacuum: http://www.pfeiffer-vacuum.com/

[46]*Low Level Measurements Handbook*, Keithely Instruments 6th Edition, website: www.keithley.com

[47]*Highly Sensitive Optical Receivers*, K. Schneider, Springer, Germany Berlin 2006

[48]*Introduction to Scanning Tunnelling Microscopy: Second Edition*, C. Chen, Oxroft University Press, UK 2007

[49]*Variable Gain High Speed Amplifier DHPCA-100*, FEMTO JM/08DEZ2014, Germany Berlin 2014

[50]*Keithely Model 486 and 487 Picoammeter / Voltage Source*, Instruction Manual, USA Cleveland 2000

[51]*Progress of the diagnostics at the PROSCAN beam* lines, R. Doelling, WEPC23Proceedings of DIPAC 2007, Italy Venice 2007

[52]*Keysight 81150A and 81160A Pulse Function Arbitrary Noise Generator*, Edition 2.0 Keysight Technologies, Germany Boeblingen 2014

[53]*MATLAB*: http://uk.mathworks.com/help/matlab/

[54]TERA Foundation: http://www.tera.it/

[55]*Beam* Instrumentation, J. Bosser, CERN-PE-ED 001-92, Switzerland Geneva 1994

[56]*A longitudinal density monitor for the LHC*, A. Jeff, PhD Thesis at the University of Liverpool, UK Liverpool 2012

[57] *Particle Accelerator Physics*, H. Wiedemann, Springer Verlag, Heidelberg 2007

[58]*An introduction to particle accelerators*, E. Wilson, Oxford University Press, UK Oxford 2001

[59]*Projected and slice emittance measurements using multi-quadrupole scan and streak readout at PITZ*, R. Spesyvtsev, DESY Zeuthen TESLA-FEL Report 2009-09, Germany Zeuthen 2009

[60]*A transverse slice emittance measurement system using quadrupole scan technique and streak readout at PITZ*, R. Spesyvtsev, Proceedings of FEL08 Conference TUPPH037 (326-329), Korea 2008

[61]*OptiM* FermiLab: http://www-ap.fnal.gov/~ostiguy/OptiM/

[62]*LHCb Technical Design Report*, CERN/LHCC 2001-0011, CERN Geneva 2001

[63]*LHCb Technical Design Report Re-optimized Detector Design and Performance* , CERN/LHCC 2003-030 LHCb TDR 9, Geneva 2003

[64]*Characterisation and commissioning of the LHCb VELO detector*, A. Papadelis, Vrije Universiteit, Enschede 2009

[65]*Introduction to Radiological Physics and Radiation Dosimetry*, F. H. Attix, Wiley-VCH, Weinheim 2004

[66]*Radiation Detection and Measurement 4th Edition*, G. F. Knoll, John Wiley & Sons, Hoboken 2010

[67]*R-measuring sensor*, The LHCb Collaboration, version 1.17. 8 September 2004, Switzerland Geneva 2004

[68]*Phi-measuring sensor*, The LHCb Collaboration, version 1.14 26 August 2004, Switzerland Geneva 2004

[69]*The LHCb Detector at LHC*, The LHCb Collaboration, Journal of Instrumentation, Institute of Physics 2008

[70]*Contribution to the development of the acquisition electronics for the LHCb experiment*, G. Heafeli, EPFL, Lausanne 2004

[71]*The Beetle Reference Manual – chip version 1.3, 1.4 and 1.5*, S. Loechner, CERN LHCb-2005-105, CERN Geneva 2006

[72]*Further optimisation of the VELO material*, The LHCb Collaboration, CERN LHCb 2001-099, CERN Geneva 2001

[73]*The LHCb VELO: Status and Upgrade Developments*, A.G. Bates, CERN LHCb 2004-098 VELO, CERN, Geneva 2004

[74]*CO_2 cooling for the LHCb-VELO experiment at CERN*, B. Verlaat et al., GL2008 8th IIF/IIR Gustav Lorentzen Conference on Natural Working Fluids, Copenhagen 2998

[75]*Application of the pedestal following algorithm to the VELO detector*, T. Szumlak, CERN LHCb-2009-036, Cern Geneva 2009

[76]*Position reconstruction and Charge Distribution in LHCb VELO Silicon Sensors*, T.W. Versloot, CERN/LHCb 2007-119, CERN Geneva 2007

[77]*Specification and common readout board board for LHCb*, G. Haefeli, CERN/LHCb2003-007, CERN Geneva 2003

[78]*Application of the Beetle Cross Talk Correction algorithm for the VELO Detector*, T. Szumlak et al., CERN/LHCb-PUB-2009-006, CERN Geneva 2009

[79]*LHCb VELO and ST clusterization on TELL1*, G. Haefeli, CERN/EDMS 690585, CERN Geneva 2006

[80]Reconstruction of Cluster Positions in the LHCb VELO, T. Szumlak et al.. CERN/LHCB-2007-151, CERN Geneva 2007

[81]*VELO raw data format and strip numbering*, CERN/EDMS 637676, CERN Geneva 2005

[82]*VELO and ST non-zero-supressed bank data format*, G. Haefeli, CERN/EDMS 692431, CERN Geneva 2008

[83]*SM9859 Three Axis Micro-step Motor Drive and Control System*, Mclennan Servo Supplies Ltd. Issue A, UK Ash Vale 2012

[84]*LM Guide Actuators*, THK CO. Ltd.: http://tech.thk.com

[85]*17&23 frame size hybrid stepper motors – HS series*, McLennan Servo Supplies Ltd.

[86]Baumer Precision Mechanical Switches: www.baumer.com

[87]LabVIEW: http://www.ni.com/labview/

[88]*Host Command Reference*, Applied Motion Products 920-0002 Rev. D, USA Watsonville 2007

[89]*A heat transfer Textbook*, J. Linehard IV, Philogiston Press, USA Cambridge Massachustes 2011

[90]*Fundamentals of the Finite Element Method for Heat and Fluid Flow*, R. Lweis, John Wiley & Sons, UK Chicester 2004

[91]*A finite element algorithm for computational fluid dynamics*, A. Baker, AIAA Journal, Vol. 21, No. 6 (1983), pp. 816-827.

[92]*KTC Series Chillers K1, K3 – Installation and Operation Manual*, Applied Thermal Control Ltd. Issue 10.21, UK Withwick

[93]HYCOOL Product Specification, SRS Frigadon Group: http://www.srs-frigadon.com

[94]*EkomDK50 V2 Installation, Operation and Maintenance Manual*, Ekom spol. S r.o. NP-DK50 2V-3_09-2014-MD, Slovenia Piestany 2014

[95]Alpha Gel: http://www.taica.co.jp/gel-english/alpha/

[96]Shenzhen Ezoneda Technology Co.

[97]EHS High Precision HV modules, ISEG Spezialelektornik GmbH, Germany Radeberg 2012

[98] *CERN Document Server*: https://cds.cern.ch/

[99]*Beam Instrumentation and diagnostics*, P. Strehl, Srpinger-Velrag Berlin Heidelberg, The Netherlands 2006

[100] IEC TR 60788: 2004 Medical electrical equipment - Glossary of defined terms, International Electro-technical Commission, Switzerland Geneva 2004